5-2018

A Flexible, Highly Integrated, Low Power pH Readout

Song Yuan
University of Tennessee, syuan1@vols.utk.edu

To the Graduate Council:

I am submitting herewith a dissertation written by Song Yuan entitled "A Flexible, Highly Integrated, Low Power pH Readout." I have examined the final electronic copy of this dissertation for form and content and recommend that it be accepted in partial fulfillment of the requirements for the degree of Doctor of Philosophy, with a major in Electrical Engineering.

Syed K. Islam, Major Professor

We have read this dissertation and recommend its acceptance:

Benjamin J. Blalock, Joshua S. Fu, Nicole McFarlane

Accepted for the Council:
Dixie L. Thompson

Vice Provost and Dean of the Graduate School

(Original signatures are on file with official student records.)

A Flexible, Highly Integrated, Low Power pH Readout System with Wide Range

A Dissertation Presented for the
Doctor of Philosophy
Degree
The University of Tennessee, Knoxville

Song Yuan
May 2018

Dedication

This dissertation is dedicated to my mother, Suzhen Li, who is suffering Spinocerebellar Atrophy during this research, my father, Zhongxue Yuan, my wife, Pei Yu and my sons, Shaojie Yuan and Shaoxian Yuan. Mother's enthusiasm and love of life is my strongest motivation of this dissertation. Father’s philosophical thought shaped my thinking in many profound ways. Wife’s and sons’ love is the continuous support to finish this dissertation.

Acknowledgements

This research was only possible with the encouragement and support of many people, for whom I am very grateful.

Dr. Syed Islam offered solid continuing support for this research and I consider it a great opportunity to study under him. Dr. Benjamin Blalock was a knowledgeable, creative, and thorough researcher and my analog integrated circuit design introducer. Dr. McFarlane and Dr. Joshua Fu also provide great help serving as my committee members and improving my dissertation.

It is a great opportunity to be employed at Siemens Molecular Imagining Inc., which has the mission of making PET a widely-available, clinical, medical-imaging modality. The potential of improving the quality of human life and, indeed, saving human life through medical research and clinical practice is enormous using PET biochemical imaging.

Hanson Cannon, my manager in Siemens, Arnott Chris, David Binkely, my colleagues, it is my pleasure to work with you all.

Kai Zhu served as a great supporter for this research, and his extensive knowledge and feel for IC design was invaluable.

Hanfeng Wang assisted with IC prototype design submission and publication reviews based on this research was very helpful.

Abstract

Medical devices are widely employed in everyday life as wearable and implantable technologies make more and more technological breakthroughs. Implantable biosensors can be implanted into the human body for monitoring of relevant physiological parameters, such as pH value, glucose, lactate, CO_2 [carbon dioxide], etc. For these applications the implantable unit needs a whole functional set of blocks such as micro- or nano-sensors, sensor signal processing and data generation units, wireless data transmitters etc., which require a well-designed implantable unit.

Microelectronics technology with biosensors has caused more and more interest from both academic and industrial areas. With the advancement of microelectronics and microfabrication, it makes possible to fabricate a complete solution on an integrated chip with miniaturized size and low power consumption.

This work presents a monolithic pH measurement system with power conditioning system for supply power derived from harvested energy. The proposed system includes a low-power, high linearity pH readout circuits with wide pH values (0-14) and a power conditioning unit based on low drop-out (LDO) voltage regulator. The readout circuit provides square-wave output with frequency being highly linear corresponding to the input pH values. To overcome the process variations, a simple calibration method is employed in the design which makes the output frequency stay constant over process, supply voltage and temperature variations. The prototype circuit is designed and fabricated in a standard 0.13-μm [micro-meter] CMOS process and shows good linearity to cover the entire pH value range from 0-14 while the voltage regulator provides a stable supply voltage for the system.

The goal of this work is to initially solve the linearity issue for the readout circuit, and explore the complete solution for a pH measurement system with low-cost, low-power and miniaturized silicon solution in a standard CMOS technology. Besides, mathematical derivation is developed to verify the linearity and other non-idealities such as temperature and noise effect. Finally, the chip is designed, fabricated in a commercialized process and in-vitro test is also performed to verify the entire system feasibility and performance.

Table of Contents

List of Tables

List of Figures

Chapter 1 Introduction and Motivation

1.1 Introduction

Integrated Circuits (IC) technology has been proven to be the one of the most significant inventions of human civilization. According to Moore's Law, the number of the transistors in an integrated circuit with certain size doubles in every two years. The semiconductor industry has followed Moore's Law for about half century and is still valid for the modern IC technologies. The rapid development of semiconductor technologies has made a huge contribution to the world economy, and strived a series of technology innovations, social reformation, production efficiency improvement and economy development. [1].

On the other hand, more parallel technologies have also gone through rapid evolutions. For example, with the evolution of the complementary metal-oxide semiconductor (CMOS) technology, application-specific integrated circuits (ASIC) have been realized to solve specific problems associated with particular applications. For example, radio-frequency IC (RFIC) has been implemented in CMOS technology for wireless/wireline communications involving up to tens of GHz [2].

As physics, chemistry, material science and package technology gain more and more breakthroughs, high-performance, miniaturized, low-power consumption devices or even system-on-chips (SoCs) [3] are continuously being implemented for a wide-range of applications including the emergence of another major technology called micro-electro-mechanical system (MEMS) [4]. Other application involving micro- or nano-sensors have been developed using the sensing elements to transfer signals to electronic interfaces.

A sensor is usually composed of a sensing element, an analog interface and a processing circuitry, possibly in a miniaturized microelectronic environment. The sensing element needs to meet more and more strict requirements in speed, accuracy, temperature, etc. For example, wearable electronic devices are now widely used to detect heart beats, blood pressure, dissipated calories by simply using a wrist ring. However, the collected data usually does not reflect the real value but only provide a moving tendency. Other sensing devices such as pH sensor only can work under a short temperature range which severely limits its applications. The analog interface is also facing difficulties in interacting with the sensing element, which usually provides uncertainties in loading or sourcing. To cover a wide-range of valid sensing functionalities, the analog interface and the processing circuitry are required to operate under a wide range of conditions with acceptable performance in accuracy, speed, low power consumption, etc. [5, 6].

Standard intellectual properties (IPs) such as analog-to-digital converters (ADC), microcontroller unit (MCU), and RF transceivers are also used in the sensors to provide good performance and enhanced computing capability. Using these standard IPs with good accessibility, the users can design sensor system more easily. However, these IPs also bring complexity to the system, and consumes a lot of resources such as size, power, and cost. For example, in biomedical sensors the signal usually changes very slowly and does not require fast computing. Some implantable sensors can be powered by wireless electromagnetic signals or simply a button battery, which require very low power to operate for long life-time.

On the other hand, more and more functionalities are required to be achieved for implementation of a sensor system. Following the signal processing circuitry, typically post-processing is required to realize display, signal transmission, communication etc. Discrete devices mentioned above are well qualified to complete these jobs. However, with so many devices, the sensor system will grow more bulky, complex, and power-hungry. Hence, there is a great need to integrate all functionalities in a single chip realizing a dedicated ASIC.

Another trend of modern technologies has been their ability to integrate sensing elements on a standard microfabrication process [7] since the same materials (silicon, polysilicon, aluminum, dielectrics, metal-oxides, etc.) are used to fabricate the majority of the sensor system. For example, resistive chemical gas sensors are based on metal-oxide (MOX) and silicon-based capacitive pressure sensors and their front-ends. Ion-sensitive field-effect transistor (ISFET) can be used to sense pH level by generating a sensed current to measure the concentrations in a solution. As the most popular process developed until now, CMOS technology can be used to implement these sensors because of its low-cost, high integration density, and more importantly good compatibility, so the sensors on the same process can gain these advantages automatically.

There are several important specifications required to be met in the design iof a sensor system. For example, a dynamic range is defined for the sensor so that the signal range of interest can be detected effectively. Usually the larger the dynamic range the better is the sensor. Sensitivity is defined as the minimum signal strength the sensor can detect effectively. It is always good to have high sensitivity for a high-performance sensor. Meanwhile, sensing accuracy, reliability under low and high temperatures, and noise injection are also of vital importance for a sensor performance. For a sensor measurement system, the circuitry following the sensing element must not degrade these performances, which means that the analog interface and the processing circuitry are all required to achieve these specifications as well, or even better, to ensure that the high performance of the complete sensor system is achieved [8, 9].

1.2 Research Motivation

Biomedical sensors are gaining more and more importance due to the rapid emergence of wearable and implantable sensors for healthcare. With the aging population of the world, more strict requirements are set for the development and research of biomedical sensors. The development of medical sensing technology leads to better prevention, detection and treatment of various diseases. It is an important component of the health care system and plays a crucial role in addressing the challenges associated with the modern healthcare system. A key element in the development of the healthcare systems is the use of advanced functional biomaterials and the development of new technologies to realize intelligent, miniature, reliable, low-cost, versatile, and efficient biomedical sensors that continuously monitor and detect the health conditions and functions of the human body in a real-time fashion, to ensure timely detection of disease and make timely treatment under continuous observation.

As discussed before, a monolithic sensor system is more desirable than the one with multiple discrete devices. Meanwhile, the analog front-end needs to operate under a wide range of conditions such as ambient temperature, high sensitivity, good response linearity etc. An appropriate CMOS process needs to be carefully selected to implement the complicated circuitry with affordable cost, low power consumption and miniaturized size. Innovative architectures, and novel circuit topologies are greatly needed to meet challenges from both CMOS technology limitation and strict requirements from biomedical applications [10].

Due to the progressive breakthroughs in microelectronics and microfabrication technologies, it has become more and more feasible to implement various implantable biosensors on CMOS platform thereby miniaturizing traditional measurement systems capable of analyzing physiological variables, such as blood glucose level [11, 12], lactate in bloodstream or tissue [13, 14], pressure in blood vessels or intracranial compartments [15], and pH value in the blood [16, 17]. In most of these systems, electrochemical or electro-catalytic sensors generate an analog signal in response to the presence or concentration of a particular substance or certain condition in the biological system. Usually the sensed signal is a very small in amplitude which is greatly affected by the ambient noise and the sensor itself and cannot be directly used in the detection of the analyte of interest. Hence, a signal processing unit is essential to process the signal with minimum distortion and transmit it out of the human body. To achieve that, a monolithic circuit is required to minimize the size and integrate all the functionalities together in one chip. On the other hand, the chip should consume a power small enough to maintain long battery lifetime. In [14], an integrated biosensor capable of sensing multiple molecular targets using both cyclic voltammetry (CV) and chronoamperometry (CA) was reported. The reported system can do both voltage and current signal detection as well as signal processing, and convert the sensor current to a pulse-width signal to send out the data for chronoamperometry analysis. The system was implemented in a 0.18-µm process, which was a common CMOS technology. With a 1.8V supply the total power it consumed was about 220 µW, which was good for low-power application. In [16], a wireless, highly miniaturized, low-power electrochemical integrated pH sensing system employing CMOS electronics was reported. Fabricated in a standard 0.35-µm CMOS technology, an integrated CMOS voltage controlled oscillator which consumed 120µW of power and occupied an area of 0.045 mm^2, together with a miniature electrochemical pH sensor which detected real-time changes in pH levels. The reported system could provide continuous and real-time monitoring of carbon dioxide in totally implantable device applications.

These reported works use more discrete devices and IPs to implement the sensor system, which become more and more unacceptable in low-power and miniaturized applications. The monolithic works are also reported but still need more improvement in terms of complexity, power consumption and sensor size.

In this work, a monolithic pH measurement system with power conditioning system by optical source is presented. A novel topology for a low-power, highly miniaturized electrochemical pH sensor readout circuit with wide measurement range of pH values is proposed, and the power conditioning circuit is also included to make it a complete monitoring system. The readout circuit converts the output voltage of a pH sensor, which corresponds to the pH value of a solution under measurement, to a square-wave signal with its frequency being proportional to the pH sensor output voltage. A simple calibration method is employed in the design which makes the output frequency stay constant over process, supply voltage and temperature variations. The prototype system is designed and fabricated using a standard 0.13-μm CMOS process and the measurement results show that the sensor has good linearity to cover the entire pH value range from 0-14. The proposed sensor consumes 12.8 μW of power with 1.25 V supply voltage for a typical pH value of 7 while occupying a die area of 0.017 mm^2.

1.3 Research Goal

The pH sensor measurement system will be designed and implemented in this work. The research goals for this work are summarized as below:

- Study the popular topologies of pH sensors and their features;

- Study the sensing principles and readout circuit for pH sensor and implement it under standard 0.13-μm technology;
- Study and realize low-power technologies for signal processing circuits;
- Study and implement a wide-range, high-linearity, low-power pH sensor measurement system for a wide range of applications;
- Propose a simple and feasible method to calibrate the output frequency to overcome the variations from process, voltage supply and temperature (PVT);
- Developed the basic mathematical model to validate the high-linearity and frequency calibration.
- Developed the power management unit for the pH sensor and readout circuit, to make the pH measurement system a complete one suitable for a low-power application.

1.4 Dissertation Overview

The remaining chapters of the dissertation cover the design, implementation, test, and measurement of the proposed pH sensor readout circuit, including comparison between the proposed and the conventional ones. Chapter 2 discusses the background of the physiological parameter real-time monitoring and some recent progress of realizations. Chapter 3 introduces the principles of pH sensing and readout, and compares the state-of-art published works. It also describes the bigger picture of the application background of this sensor, and how the whole sensor system works. Chapter 4 provides literature review of the pH sensor readout circuit, and describes the circuit implementation including the mathematical derivations and transistor level analysis for each building block, provided with some important simulation results. Chapter 5 summarizes the test results of the prototype of pH sensor readout system and the voltage regulator performance, including the in-vitro test results. The future work is included in Chapter 6.

Chapter 2 Biomedical Sensor Systems

Recent developments in biomedical, chemical, microelectronics and microfabrication process technologies have made biomedical sensors more and more feasible and available for widespread applications. For example, in some applications, the biosensors now can be implanted into the human body for monitoring of relevant physiological parameters, such as glucose, lactate, CO_2, etc, as was discussed in previous chapter. For these applications the implantable unit must include a complete set of functional blocks such as micro- or nano- sensors, sensor signal processing and data generation units, wireless data transmitters etc., which place strict requirements on the design of the implantable unit. The most important ones may include low-power and small-size of the implantable system.

K. Zhu et. Al [18] reported another biomedical sensor platform shown in Fig. 2.1. For the implanted system, continuous and long-term powering is usually a critical issue. Previously, tethering power cables (percutaneous plugs) were used in some clinical implantable applications, but they suffer from some serious drawbacks such as potential path for infection due to breaking of the skin thus creating potential risks of safety of the individual as well as the implant. Another alternative will be the use of batteries [19]. Unfortunately, there are also some limitations associated with that. For example, batteries can be considerably large compared to the monolithic implanted circuits, and can potentially leak and cause hazard to the body tissues. In addition, batteries are associated with limited life times. Therefore, inductive link is used as the solution to the continuous powering system since it is free of external cables and batteries [20]. Besides, the inductive link is also durable and suitable for long-term use while making the miniaturization possible. In addition, with an inductive link, the power and the data signals can be transferred simultaneously or by time division multiplexing depending on the architecture used.

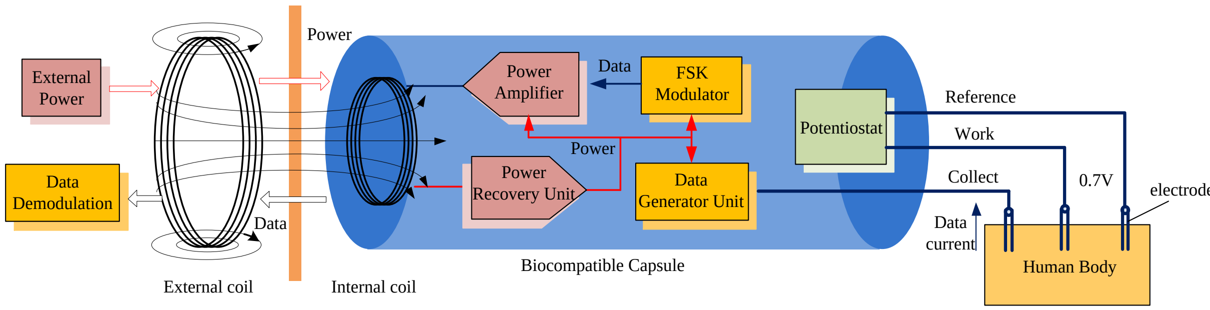

Fig. 2.1. Block diagram of the inductively-powered implant system [21].

In [21], it reported an implantable bio-sensing platform architecture that enables calibration and reading of multiple sensors including glucose, lactate, oxygen, and CO_2. It also enables checking power levels of the electrical source powering various electronic, optoelectronic and micro-electromechanical (MEM) components and circuits included in the implantable unit by receiving instructions from an external unit (not implanted). In addition, the architecture permits checking the operation of the potentiostats interfacing with the analyte sensors, as well as transmitting sensor readings and other data wirelessly back to the external unit.

This implantable bio-sensing platform architecture that enables the wireless selection, calibration and reading of multiple sensors, as well as checking the power levels of the electrical powering source energizing various devices and circuits embedded in the platform. It also permits checking the operation of the potentiostats interfacing with each amperometric analyte sensor. In one embodiment, mode selection (such as sensor calibration, sensor reading, power level check, potentiostat check) is carried out by finite state machine-based architecture. Operations such as receiving instructions from an external unit, performing desired tasks, and transmitting output data are carried out using optical communication link(s). In this embodiment, the powering of the implantable unit is carried out by utilizing optical sources located in the external unit which are incident on solar cells in the implantable unit. In other embodiments, each sensor communicates its output data at a distinct optical wavelength which is received by the photodetector located in the external unit or proximity communicator. In yet another embodiment, each sensor is selected by activating a sensor using pulse coding architecture.

Nowadays, medical devices are widely employed in everyday life as wearable technologies make more and more technological breakthroughs. The internet can be employed to transfer any medical data from a patient to a caregiver to provide interactive communication for improved healthcare. For example, diabetic patients can monitor glucose level at home using the home care assistance system [22] and the data can be transferred to and monitored by doctor located in a remote medical facility. Battista et al reported investigation of a wireless remote monitoring system that can help patients monitor their conditions and get advice from doctor at home [23]. This monitoring scheme covers most of the important physiological parameters and the data can be sent via internet in real-time. Physiological parameters such as glucose, oxygen, lactate values can all be measured with a miniaturized sensor system which can be implanted in the human body as shown in Fig. 2.2 [21]. This scheme resolves the problem of finger pricking to collect the physiological data for diabetic patients. The data can also be transferred via smartphones. However, these applications still meet many challenges such as measurement accuracy, device cost, power consumption etc.

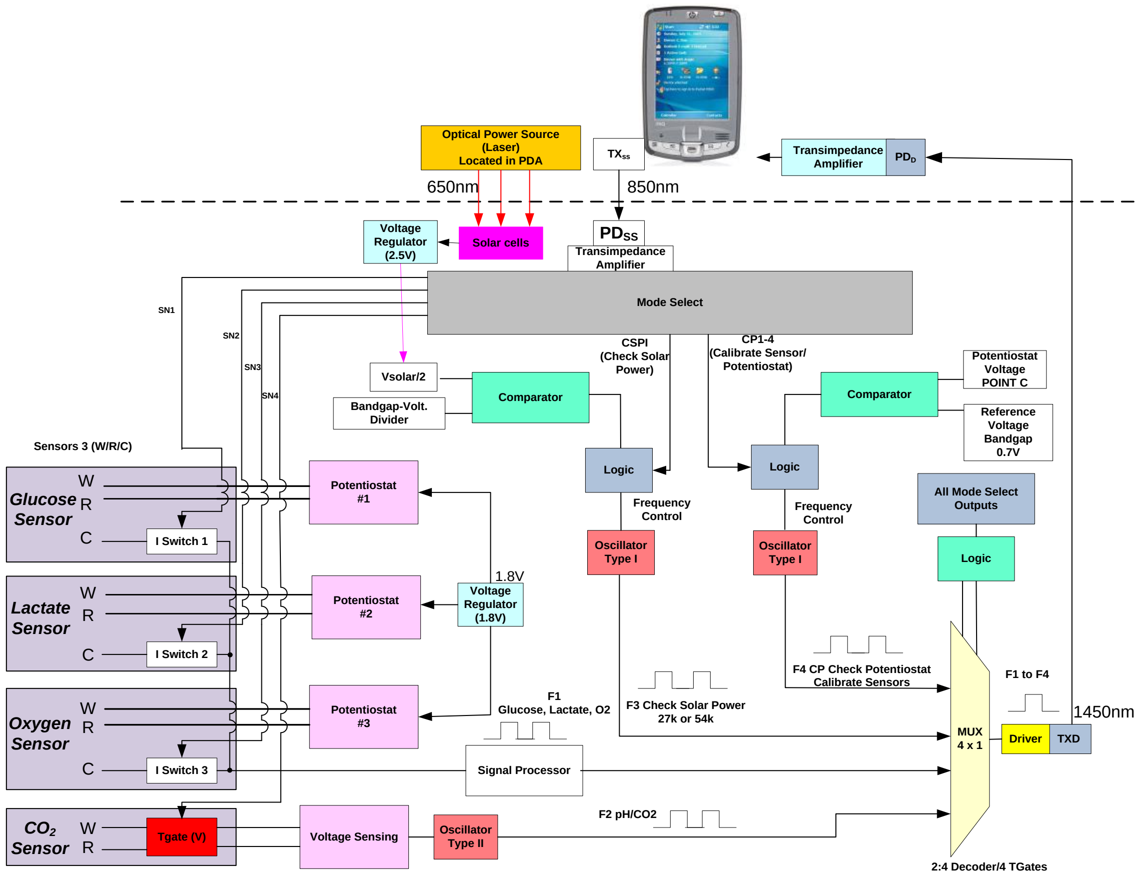

Fig. 2.2. Multi-analyte sensor architecture where instructions are received from a transmitter located in the PDA unit.

Chapter 3 pH Sensors and Readout Circuits

3.1 pH Sensors

PH level is a crucial parameter in a wide range of applications, such as human body health [24], water pollution control [25], environmental inspection [26]. These are all related with pH levels. For example, drinking water is usually considered healthy and less polluted if the pH level is slightly alkalescent or neutral. Clothes materials have different ranges of safety and environment friendliness. There are a lot of parameters to evaluate how environment and human friendly for a certain material, but pH level is one of most fundamental ones. Monitoring pH levels during the whole fabrication, has caused more and more attention from clothes manufacturers. If the pH level from the textile exceeds the proper range, it can cause scytitis, pruritus, and other skin problems to customers.

E. coli organism is used in a lot of places to reflect hygiene condition to check for food safety. Therefore, the Health Protection Agency even settles the standard that for food that is good to eat must have the E. coli density less than 20 cells/ml. Jiang et. al reported a solution to detect the food safety using a pH sensor in [27]. The detection principle is to firstly culture the original E. coli DH5α sample, and then dilute it to different concentrations, and then incubate it for a direct pH measurement. Different samples will result in different pH levels along with culture time, and eventually the pH difference can indicate the E. coli levels. In this way the E. coli levels are measured, and food safety is detected.

Different applications will require different ranges and accuracies [24-28]. In some applications such as environmental monitoring, a wide pH range is preferred to detect an object of interest to explore the environmental conditions. The pollution from exhaust emission and industrial wastewater discharge usually makes water become more acid. These can be detected by a pH sensor easily as well.

For human body, various parts have quite different pH levels. For example, many enzymatic processes are highly sensitive to pH variations and operate most efficiently with plasma pH levels in the physiological range of 7.38 – 7.42 [29]. Table 3-1 shows a typical pH levels in different organs and fluids, etc., in human body [30].

TABLE 3-1 PH OF SELECTED FLUIDS, ORGANS, AND MEMBRANES.

Organ, Fluid or Membrane	**pH**	**Function of pH**
skin	4-6.5	Barrier protection from microbes
Urine	4.6-8.0	Limit overgrowth of microbes
Gastric	1.35 – 3.5	Break down protein
bile	7.6-8.8	Neutralize stomach acid, aid in digestion
Pancreatic fluid	8.8	Neutralize stomach acid, aid in digestion
Vaginal fluid	<4.7	Limit overgrowth of opportunistic microbes
Cerebrospinal fluid	7.3	Bathes the exterior of the brain
Intracellular fluid	6.0-7.2	Due to acid production in cells
Serum venous	7.35	Tightly regulated
Serum arterial	7.4	Tightly regulated

It is concluded in a certain component or organ, the pH variation is very small (Urine has a wider range covering from acid to alkaline), however, to detect the all of them, the pH sensor must be able to work between less than 1.35 to 8.8 or higher.

It becomes more and more important to monitor the pH level, along with some other parametric index such as glucose, lactate, oxygen to diagnose the healthy condition in human body in a real-time manner. For example, in medical applications, a slight change in the pH value may provide good evidence of other reactions and possibly discover previously unknown trends, given the total range of pH values in human body is very limited. In some cases, knowledge of these trends can result in more efficient treatment option and reductions in the intake of medicine. It is also possible to react more quickly to changes in human body due to real-time monitoring with online sensors, which can identify problems more quickly.

It is of significant importance to maintain balance of vital metabolic analytes for human body. This is to help body immune system to counter acute and chronic diseases. However, imbalance always emerges easily due to various reasons. For example, CO_2 concentration or the metabolism of various fats and proteins can generate acidic compounds. The hydration of CO_2 in the plasma creates carbonic acid where it dissociates into bicarbonate and H+, so the pH level is changed, as described in the chemical reaction equations (3-1) and (3-2).

$$CO_2 + H_2O \rightarrow H_2CO_3 \tag{3-1}$$

$$H_2CO_3 \rightarrow HCO_3^- + H^+ \tag{3-2}$$

Usually an invasive arterial blood gas (ABG) method is employed to detect plasma pH levels, in which blood needs to be sampled and analyzed in medical environment. This method is usually performed every couple of hours and not comfortable for patients. Therefore, continuous monitoring of local H+ concentration in the plasma becomes more and more imperative for diagnose and observation of abnormal metabolic ailments.

An additional potential benefit of continuous monitoring is the ability to acquire more data for a similar or slightly lower number of man hours and cost. These put a lot of requirements on the design of sensor and measurement system. For example, real-time measurement needs very low-power solution and miniaturized size for both the sensor and the readout circuit. In [21], a four-sensor health monitoring system was reported which included pH sensor based on voltaic sensor processing unit. In [32], a V-I converter is employed to measure pH value from the ISFET sensor. It converts the voltage from the sensor to a current for signal conditioning. However, this V-I converter adds additional electronic blocks such as amplifiers to the sensor system and consumes a lot of current which is not suitable for low-power applications.

Various structures of pH sensors have been reported in recently published works, such as plastic optical fibers [33], ISFET [34], FinFET [35, 36], EGGFET [37], and capacitance measurement [38], impedance measurement [39], and electrochemical [16, 40] pH sensors.

3.1.1 Optical pH sensor

Fig. 3.1 shows a typical optical pH sensor and block diagram of detection on neuromorphic CMOS sensor IC (SIC). In the experiment setup in Fig. 3.1(a), the halogen bulk is used as the light source, go through the visible bandpass filter (VBF) which helps the light intensity across the visible wavelengths. The solution is used in the cuvette, the sensor IC will sense the light and process it to decode the pH level. The SIC has an integrated CMOS photodetector and processing circuitry, and outputs a voltage proportional to the light detected (also proportional to pH level).

HWLS Optical pH sensors can be compatible with commercial CMOS technology without post-processing deposition (unlike many ISFET systems [41 - 46]). In addition, the fabrication process is relatively easy and inexpensive without the need for frequent calibration. Another advantage of this type of pH sensor is that its size is not as large as other standard pH sensors such as glass pH electrodes and is not fragile.

The drawback with this type of PH sensor and its readout circuit is pretty apparent: it requires extra optical sources and detection circuit for the system (Fig. 3.1(b)). Meanwhile, the result in [32] shows obvious non-linearity over the PH value, which reveals its weak immunity over noise and variations.

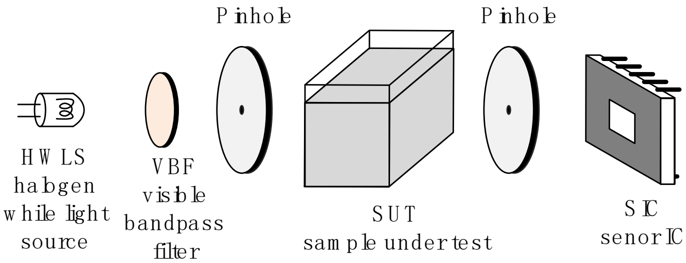

(a)

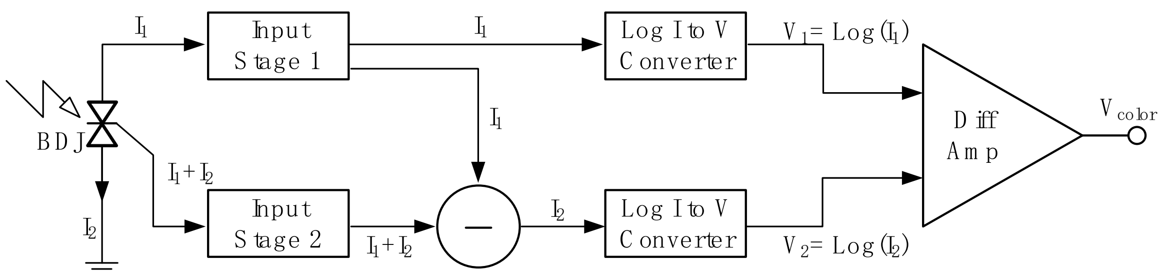

(b)

Fig. 3.1. (a) pH measurement setup diagram with optical sensor (b) and the block diagram of the CMOS SIC in [32].

3.1.2 pH Sensor Based on ISFET

One of the most conventional pH sensors is fabricated based on ion sensitive field-effect transistor (ISFET). It was originally introduced in [41] as an application for measuring chemical quantities. Later it has been extensively studied and reported and is continues to be a viable option to date [42-46]. Fig 3.2 shows a typical ISFET pH sensor. The cross-sectional view reveals that the device is very similar to a standard MOSFET device, which has gate terminal as an electrolytic solution where the reference electrode is generated. In particular, the interface between the metal gate and insulator is to be replaced by the reference electrode. Fig. 3.2 shows a n-type ISFET which is similar with a n-type MOSFET in a standard CMOS process.

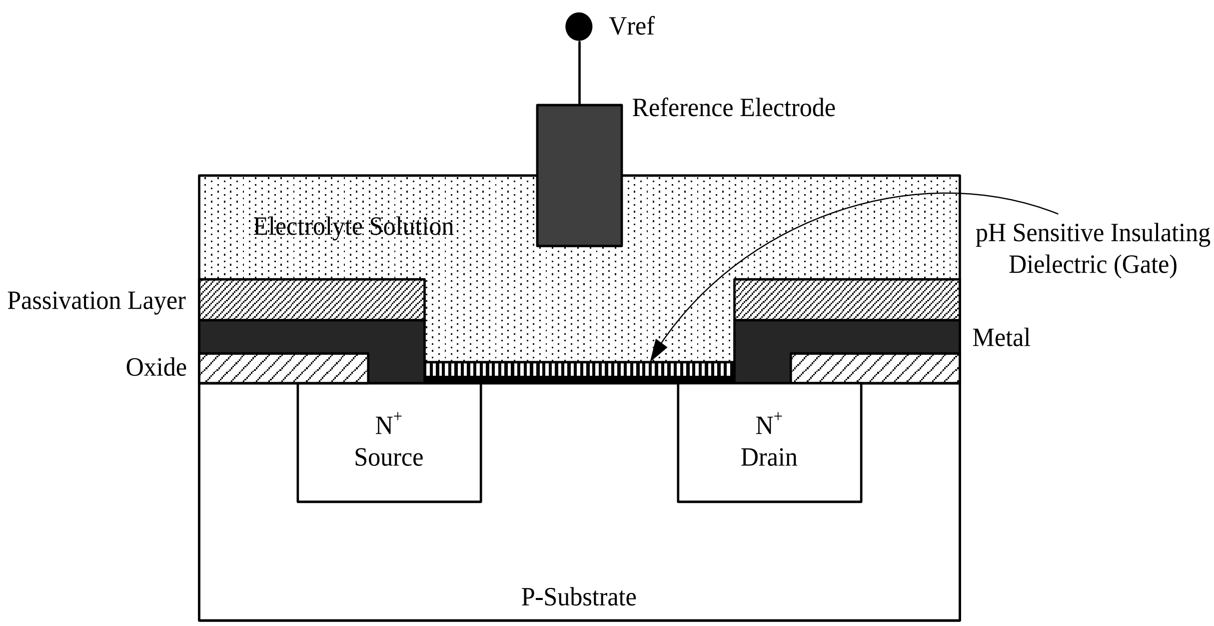

Fig. 3.2. A cross-sectional view of the n-ISFET.

From [41], the threshold voltage (V_T) of the ISFET can be written as:

$$V_T = K_1 + \psi_O(pH) \tag{3-3}$$

where K_1 summarize all the pH independent quantities, and $\psi_o(pH)$ represents the potential difference between the insulator surface exposed to the electrolyte and the bulk of the electrolyte itself. The ISFET device is commonly biased to operate in the linear mode where $V_{DS} << V_{GS}-V_T$. The drain current in this case is given:

$$I_{DS} = K[(V_{GS} - V_T) - V_{DS}/2]V_{DS} \tag{3-4}$$

Thus,

$$V_{GS} = I_{DS}/KV_{DS} + V_T \tag{3-5}$$

Using equation (3-4):

$$V_{GS} = I_{DS}/KV_{DS} + K_1 + \psi_O(pH) \tag{3-6}$$

It is evident from Eq. (3-6) that any change in the electrolyte pH will result in a corresponding change in the gate voltage, V_{GS}.

In [42], a high-sensitivity CMOS-based pH sensor was published, which exceeded the Nernst limit of 59mV/pH. The sensor circuit consisted of two sensors each with a charge sensing field effect transistor (FET) and an extended sensing gate (SG). The two ISFETs, one n-type and one p-type form a differential structure to perform differential measurement. Similar to many other differential circuit structures such as differential input pair, it can cancel common-mode noise which is a main source of sensing error from both the reference electrode and the solution. On the other hand, there is no need of a real reference electrode anymore, which is usually achieved by by Ag/AgCl electrodes. Hence it becomes implantable and suitable to be used in autonomous applications. But the complementary pair of ISFETs were used which hurt the sensor size and fabrication complexity.

From the previous discussion, the ISFET looks very similar with a standard MOSFET device in a CMOS technology, and seems to be compatible with CMOS devices. However, to be a reliable device in a CMOS process, the ISFET still has a couple of issues to be resolved, such as time dependence of the threshold voltage, temperature effect on the measurement, and the difficulties associated with packaging to implement the reference electrodes. These problems can prevent the ISFET from being commercialized for extensive applications, especially for reliable, long-term real-time pH monitoring systems. To deal with these issues, a real differential ISFET sensor is proposed in [45]. Combining a conventional ISFET and a reference FET (REFET), the proposed differential ISFET sensor can provide the same ISFET characteristics but insensitive to the pH variation, both are integrated in the same device structure.

The differential ISFET reported in [45] can demonstrated in Fig. 3.3. It includes two FETs in one ISFET, one is regular ISFET and the other is reference FET (REFET). The REFET has same ISFET characteristics but insensitive to the pH variation. It has very obvious advantage due to its differential configuration which provides good rejection of common-mode noise. For example, the disturbance caused by temperature coefficient and environmental noise can be cancelled by this differential configuration of the ISFET. Another advantage of this topology, is the elimination of ghe reference electrode issue. The liquid junction potential can react quite fast to the change in ionic composition which can occur at the same time when the ISFET responds to the sample. However, with this differential topology, the potential change be can rejected as a common-mode signal similar to the noise.

This sensor and readout system requires differential ISFET, which can provide good immunity over the environmental noise and disturbance, and the output current is proportional to pH value as well. However, the at least double ISFET and six operational floating current conveyors OFCC of readout circuit make this system too bulky and power hungry to be used in some biomedical systems, in particularly the implant system. Also, ISFET usually needs post-processing deposition using commercial CMOS standard processes.

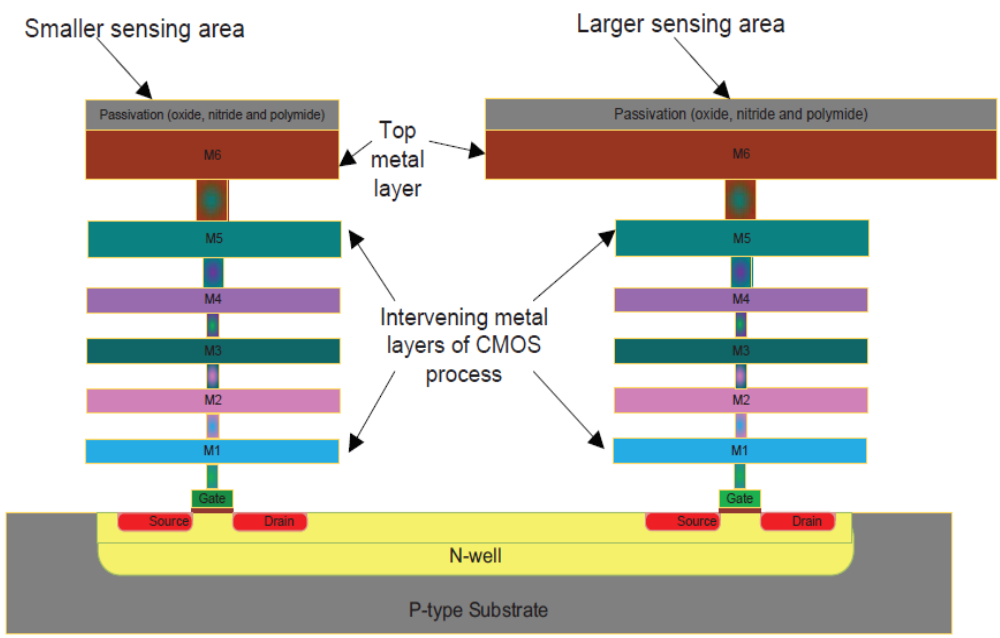

Fig. 3.3. Cross section views the differential ISFET in [45].

As mentioned before, the threshold voltage of an ISFET can be too high to be used in a standard CMOS technology (3.3V supply voltage or lower), which is due to existence of trapped charge, either embedded within the native passivation or on the floating gate of device. To counter large referred threshold voltages and mismatch, a programmable gate ISFET was proposed and fabricated in a standard CMOS process in [47]. The proposed device used a capacitively coupled floating gate to allow tunability of its operating point to counteract the presence of trapped charged, thus allowing operation within a tolerable gate voltage range.

In [46], a hexagonal honeycomb structure-based CMOS ISFET sensor which exhibits a more compact arrangement as part of large arrays and provides benefits in terms of capacitive attenuation.

It is classified as enclosed gate transistors (EGTs), can be used in standard CMOS technology and effectively reduce the gate capacitance by 20% - 40%.

3.1.3 pH Sensor based on other FETs

Although ISFET has been widely studied and demonstrated, there are still some challenges to obtain high sensitivity. Therefore, other field-effect transistors (FETs) can also be employed to implement pH sensor, such as FinFET [35, 36] and FinFET can be also fully compatible with the standard CMOS process. The previous section introduced some advanced methods to achieve high sensitivity, however, high-k dielectric materials, such as HfO_2 have been investigated and demonstrated to be the most pH sensitive materials.

In [35], a pH sensing microfluidic chip based on the heterogeneous integration is reported. The integration includes a small Ag/AgCl quasi-reference electrode, a high-k FinFET sensor with liquid gate and passive microfluidic. These three components are integrated as a complete and compact sensor to monitor ionic change in biofluids which can be applied in several applications such as healthcare service. A sensitivity of 8mV/pH is achieved with a DC current operation scheme.

Another FinFET-based sensing voltage-readout work is reported in [36]. In this work, the pH readout system is implemented in a silicon bulk and shows a very high sensitivity up to $\Delta Vout$ = 185 mV/pH and $\Delta Vout/ \Delta VpH$ = 6.6. The sensitivity is fluctuating depending on the pH level. The pH can be sensed in a range from 3 to 8. This reported pH sensor can have much faster response time than a single FinFET counterpart. Moreover, the power consumption is also small. It could be used consistently both as a sensing and a readout element, and preserved its electronic performance under scaling with low power consumption.

3.1.4 pH Sensor based on Capacitance Measurement

pH value changes can cause some other interesting electrical changes. In [38], it is reported that the pH changes in the electrolyte can cause shift in the capacitance-voltage characteristics in an Electrolyte insulator semiconductor capacitors (EISCAPs). This feature can be used to be as pH biosensors. Fig. 3.4 shows a typical structure of the EISCAPs pH sensor. It consists of a stack of nitride and oxide dielectric layers on silicon. The electrochemical relationship between the flat band shift and the hydrogen ion concentration is given by the Nernst response [33].

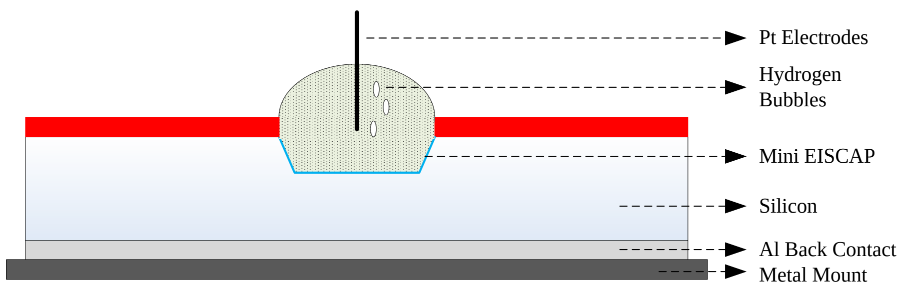

Fig. 3.4. The structure of the EISCAPs pH sensor in [38].

To convert the C-V characteristics into readable format for furthermore process, such as communication or computer, this pH sensor needs a readout circuit to sense the capacitance. Fig. 3.5 shows a typical relaxation used to sense the capacitance of the EISCAPs pH sensor. It can convert the sensed capacitance into different oscillation frequencies.

The relaxation oscillator in Fig. 3.5 can generate an output frequency depending on the input voltage which represents the pH level assuming that the output frequency is denoted as f_{ref} under pH_{ref} in the sensor electrolyte. Analogically, output frequency shifts to fx when pHx are applied.

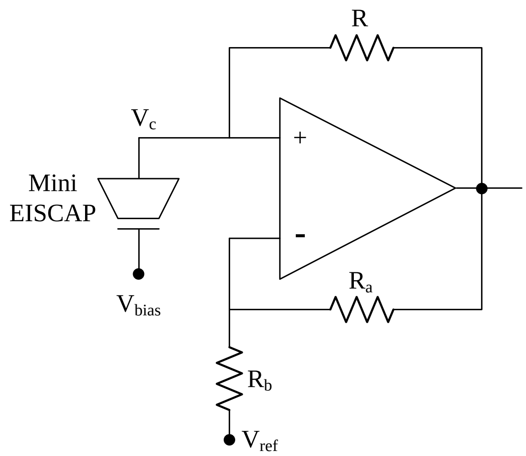

Fig. 3.5. Schematic of the EISCAP relaxation oscillator.

Assume that $pHx > pH_{ref}$ and voltages (V_H, V_L, V_{bias}) are initially set appropriately as shown in Fig. 3.6 as the function of C (V_{ref}) curve. Then we have:

$$V_H = \frac{V_{ref} R_a + V_{dd} R_b}{R_a + R_b} \tag{3-7}$$

$$V_L = \frac{V_{ref} R_a}{R_a + R_b} \tag{3-8}$$

$$f_{ref} = \frac{1}{2}[\int_{V_L}^{V_H} C(V_{ref} - V_{bias}) dvc]^{-1} \tag{3-9}$$

$$f_x = \frac{1}{2}[\int_{V_L}^{V_H} C(V_{ref} - V_{bias}) dvc]^{-1} \tag{3-10}$$

$$C(v_x) = C(V_{ref} - \Delta V) \tag{3-11}$$

At 25^{o}C,

$$\Delta V = 0.0592(pHx - pH_{ref}) \tag{3-12}$$

3.1.5 Impedance measurement based pH sensor

Impedance obtains good emphasis in sensors because people have found more and more biochemical parameters are directly related with it. Chuang et al. [39] reported a pH sensor consists of an interdigital electrode array on a flexible printed circuit and a thin-film polyaniline as the sensing layer. With different pH level in the solution, the impedance of the polyaniline also swings because the conductivity of the polyaniline changes on the redox state.

Fig. 3.6 shows the microfabrication process of the PANDB (Polyaniline dodecyl benzene sulfonic acid). The reported pH sensor can detect a pH value from 2 to 12 due to the change in impedance. The difference in the impedance change between the unreacted and the reacted sensors can be several orders of magnitude. The high resolution makes it feasible as a pH sensor by measuring the impedance with the circuit described above.

Therefore, it can be concluded that the problem with this sensor and its detection circuit is mainly on the sensitivity. The pH is changing very slowly so the detection circuit is designed with very high sensitivity, which in sequence introduces accuracy and linearity problem. The result shows a big non-linearity and sharp increment when pH value is higher than 10.

3.1.6 Electrochemical pH sensors

From the previous discussion, ISFET usually needs special fabrication process, even some CMOS process-compatible ISFET fabrication has been reported, however, the linearity of pH change is not very favorable. The plastic optical fibers usually employ expensive optical processes and require extra light sources. There are a lot of pH sensors using electrochemical electrodes to detect pH [40, 49]. Traditional glass membrane pH electrodes have the disadvantage to be delicate and expensive. The main alternative to these electrodes is a structure containing a metal oxide, which acts as the active component. pH response has been observed for certain types of electrically semiconducting oxides, in particular lead, cobalt, iridium or molybdenum oxides. These metallic oxide-based electrodes can be miniaturized but they have the disadvantage to be toxic. Therefore, polymer-based pH electrodes which are biocompatible and inexpensive, can be miniaturized to be used in clinical or biological applications, such as in-vivo analysis.

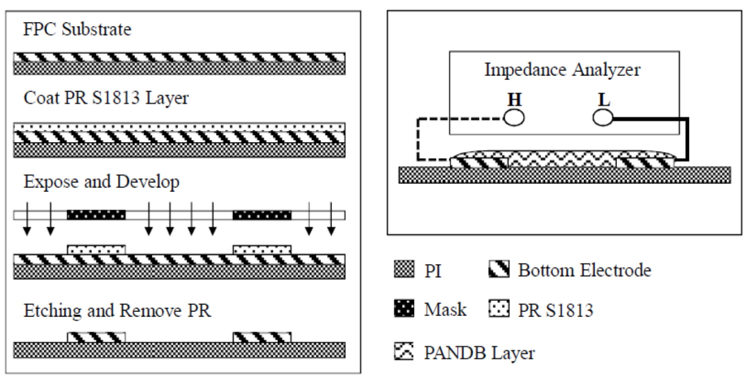

Fig. 3.6. Microfabrication process of PANDB sensor.

Heineman et. [50] al firstly reported the pH sensor resulting from electropolymerization of chemical compounds at electrode surfaces. The Nernstian potentiometric response to pH changes was found on a platinum electrode electrodeposited with a film of poly. Later, more works were reported on this type of sensor as the protonation of nitrogen or oxygen atoms in the polymers are expected to impart a pH response to the chemically modified electrodes. These works verified the electrosynthesized polymers suitable for pH sensors because they are strongly bonded to the electrode surfaces during the electropolymerization step. Moreover, it makes possible that chemically modified electrodes exhibit potentiometric responses depending on the pH changes due to the presence of amino groups, for example onto the modified surfaces. What makes it more favorable is the potentiometric responses to pH changes appeared linear, reversible and stable in time thanks to the amino groups present in the polymer backbone. This type of pH sensor also shows little dependence on the direction of pH changes, in other words, it also shows good response reversibility. Using electrochemical sensor usually has very good linearity and easy commercial availability. The size is also very small (<1mm length) which is very suitable for medical use.

The same type of pH sensor is employed in this work. Coil-type electrodes were created along with the electrochemical sensor for its high linearity and reversibility. The sensors were fabricated by first winding 125 µm platinum (Pt) and silver wire to form the working electrode and quasi-reference electrode (in contrast to aqueous reference electrodes such as the saturated calomel electrode (SCE)), respectively. Fig. 3.7 shows the fabricated electrodes briefly. The Ag/AgCl quasi-reference electrode was then fabricated by coiling silver (Ag) wire in close proximity to the working electrode, followed by converting the surface to AgCl via galvanometry (at 0.4 V vs. standard calomel electrode for 5 min) in a stirred 0.1 M HCl solution. The resulting sensor has a radius and length of ca. 0.5 mm and 7 mm, respectively, with a working electrode area of 3 mm^2. The working electrode was then electrochemically cleaned in a 0.5 M H_2SO_4 solution via potential cycling between -0.21 to 1.25 V, until a stable background current has been reached [51]. The electrode was then coated with a thin film of poly phenylene diamine (PPD), via electropolymerization from a 5-mM solution of o-phenylenediamine and by applying a voltage of +0.7 V to the working electrode [49].

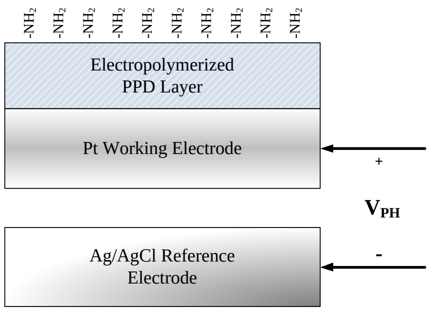

Fig. 3.7. Ag/AgCl reference electrode and Pt working electrode of the coil-type pH sensor.

For a popular calibrated voltaic pH sensor whose output voltage is proportional to the pH values, the typical output voltage range required to cover the dynamic pH values is about -0.5V to +0.5V. Usually the pH range of 7-8 is good for biomedical application while submersible pH sensor needs to cover pH values in the range of 4-10 with the same voltage range.

The sensor employed in this study is of the voltaic type, which utilizes an electropolymerized poly (phenylene diamine) (PPD) film on top of the working electrode, as depicted in Fig. 3.7. The mechanism of pH detection is based on the changes in the conductivity of the PPD film because of protonation of its amino groups.

3.2 pH Readout Systems

pH sensor output is usually a DC voltage or current signal, whose value is proportional to the pH level. Hence, a readout system is needed to transfer this information to a terminal such as a smart phone, computer, or other medical device to monitor and analyze the pH level. In some readout systems, analog-digital converter (ADC) is employed to acquire the pH information with digital signal processor (DSP) or microprocessor followed. This gives accurate readout information as ADC and DSP are powerful calculator. However, this requires expensive components and large power consumption, which is very unfavorable for low-power applications. In this session, other integrated alternatives to save cost and current consumption will be introduced and summarized.

3.2.1 Conventional pH Measurement Systems

A lot of reported pH sensor readout system are not monolithic IC, but a board-level system with different functional components. In [38], the EISCAP based pH measurement system is shown in Fig. 3.8.

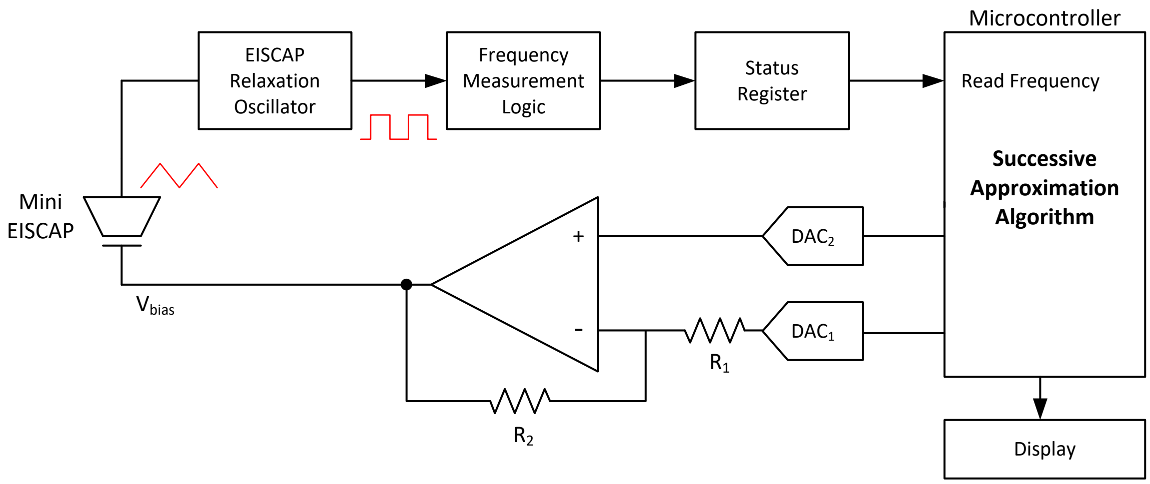

Fig. 3.8. Block diagram of the pH measurement system in [38].

As is shown in the figure, if we consider the EISCAP relaxation oscillator is the detection circuit, then several separate components are employed, such as frequency measurement logic, status register, microcontroller, DACs, and operational amplifier. However, there is no power conditioning unit used. And these components are expensive and power hungry.

In [43], a thermally powered integrated pH measurement ASIC is reported for on-body applications using an array of ISFETs, supported by design considerations for an on-body thermally powered device and evaluation of thermoelectric generators (TEGs) for this application, shown in Fig. 3.9. The ASIC is fabricated in 0.35-µm CMOS technology.

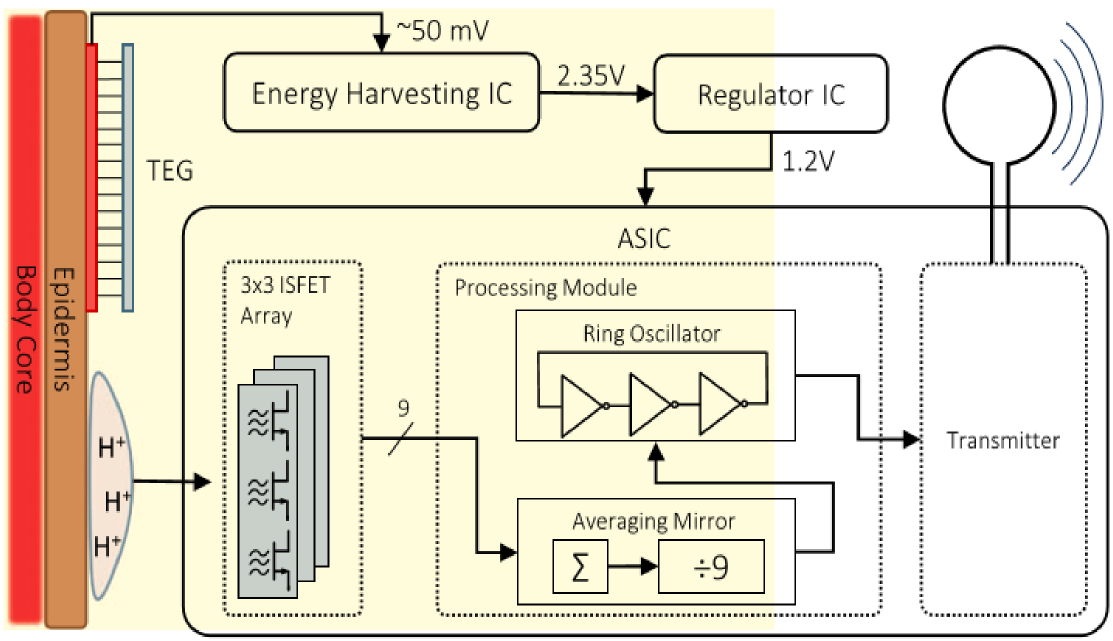

Fig. 3.9. The diagram of the system, showing the application set-up of an on-body TEG and skin-facing sensor, the main components of the ASIC and the power management ICs, reported in [43].

It is shown in Fig. 3.9 that the detection system includes two commercial power management ICs: one energy harvesting IC and one regulator IC. The reported ASIC includes a 3x3 ISFET array fabricated in a CMOS technology, a processing module, which includes a ring oscillator, and an averaging mirror and a divider. The ISFET array is employed to balance the benefits of noise reduction due to averaging with the increased power consumption brought a larger array. Output of each pixel is connected to the input of a single current mirror, with a ratio of 9:1 to perform an averaging operation. A ring oscillator is implemented to convert the ISFET sensed current to frequency, and then sent to a transmitter with a carrier frequency of 433 MHz, and on-off-keying (OOK) modulation method.

This system has a couple of advantages: first, it implements the ISFET with the readout part in on single chip; secondly, the readout circuit converts the ISFET output current into a frequency signal which eliminates the expensive ADC and following digital processing processor; the ring oscillator itself is very simple and low power, the transmitter is also implemented in the same ASIC. Thirdly, the averaging system helps reduce the noise and output accuracy.

However, the system still has some disadvantages. The entire system does not include integrated power conditioning unit, so it can only employ some commercial chip which make it not real monolithic. Also, the ring oscillator is very sensitive to process, power supply noise and temperature variations. The oscillator frequency can only demonstrate good linearity under a limited starved current. In other words, when the ISFET array needs to detect a broad range of pH values such as 0-14, then the wide range of current will make the oscillator saturate quickly and then limit the effective of the pH value detection range. This system can only detect a pH range of 5-7.

In [16], an implantable pH sensor system is presented based on coil-type electrical pH transducer discussed in Section 3.1.6 shown in Fig. 3.10. The system includes a voltaic pH sensor, an integrated CMOS pH measurement circuit fabricated in a 0.35-μm CMOS process. The readout circuit firstly converts the sensor output voltage into a current and use this current to feed a voltage-controlled relaxation oscillator. However, the linearity of the output frequency degrades substantially at higher pH levels because of the parabolic relationship of the output frequency with the sensor voltage, as analyzed in next section. Therefore, the readout circuit cannot achieve good linearity over a wide range either. The other drawback of this readout system is it does not include a power conditioning unit which makes the oscillator more vulnerable to get affected by the supply voltage noise. The readout include sensor consumes 120 μW of power with a very small detection range for biomedical applications. This can prevent the circuit from meeting the accuracy requirement in some other applications where wider detection range is required.

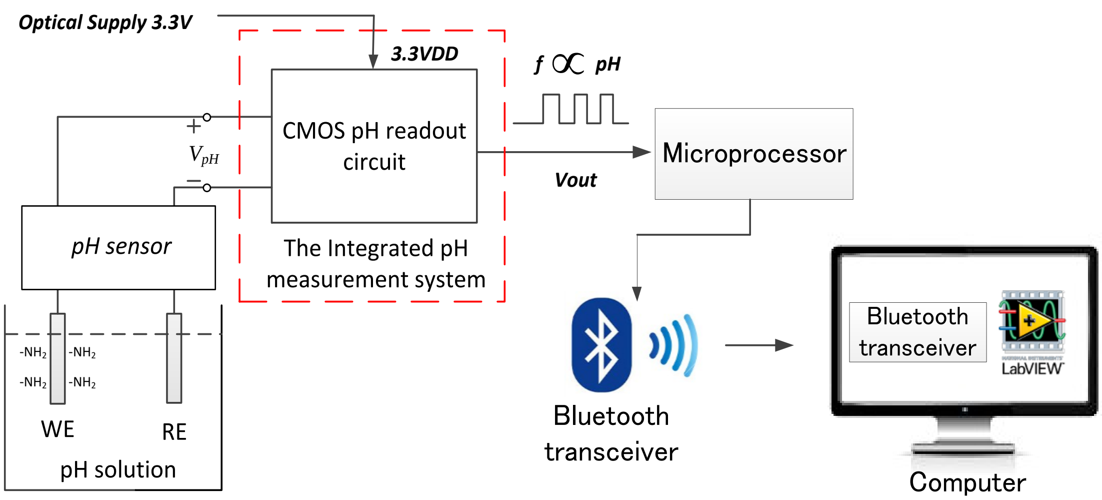

Fig. 3.10. pH sensor and measurement system [16]. This work is focused on the development of the pH signal processing unit and communication.

The output of the readout circuit is sent to a microprocessor and then into a Bluetooth transceiver. Finally, it will be communicating with a computer via Bluetooth and displayed with LabView program to monitoring real-time pH changing.

The pH measurement circuit is shown in Fig. 3.11, which is based on relaxation oscillator. MP0 with I_{bias} provides a level shifter which can lift the input voltage up to a positive voltage domain. Since the PMOS threshold V_{THP} is usually about -400mV in 0.35um process, so level shifter voltage will be positive which drives a NMOS MN1, generate a current which is proportional to $V_{PH} + V_{THP}$ (assume V_{TH} is much higher than overdrive). MP1 will sense this current and mirrored to MP2. MN2 will provide another mirror from M3 directly. The two current mirrors will charge/discharge Cc form the relaxation oscillator with Schmitt trigger [42].

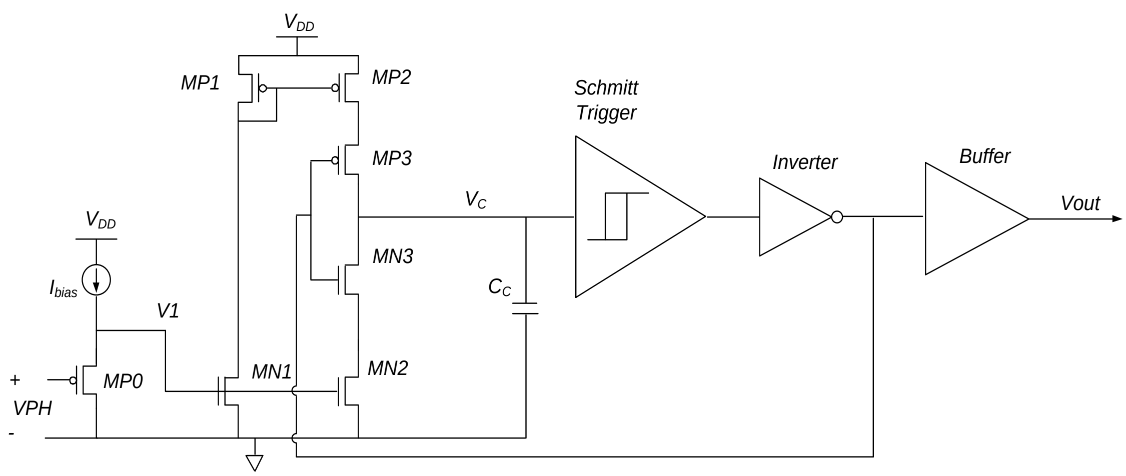

Fig. 3.11. Relaxation oscillator based readout circuit reported in [16].

Suppose Schmitt trigger upper/lower threshold is V_{t1} and V_{t2}, the difference will be $\Delta V = V_{t1}$-V_{t2}. Assume $I_{MN2} = I_{MP2} = I_C$, and t_r/t_f are rise time/fall time of Cc charging and discharging.

During C_C charging:

$$I_C t_r = C_C \Delta V \tag{3-13}$$

During C_C discharging:

$$I_C t_f = C_C \Delta V \tag{3-14}$$

So, the charging period *T* is given by:

$$T = t_r + t_f = 2C_C \Delta V / I_C \tag{3-15}$$

Ic is given by:

$$I_C = K_n * (V_{pH} + V_{THP} - V_{THN})^2 \tag{3-16}$$

Where *Kn* is the MOS parameter which can be obtained from process design kit (PDK) [2]. Apparently *Ic* has parabolic feature regarding to V_{pH} voltage which will introduce non-linearity of output frequency denoted as *f* intrinsically.

$$f = 1/T = I_C /(2C_C \Delta V) = K_n * (V_{pH} + V_{THP} - V_{THN})^2 /(2C_C \Delta V) \tag{3-17}$$

In Fig. 3 from the pH readout circuit in [5], the pMOS transistor MP0 with Ibias provides a level shifter which can shift the input voltage up to a positive voltage domain. Thus, the level shifter output node, V_1 is elevated to ($V_{PH} + V_{SG}$) where, V_{SG} is the source-to-gate voltage of MP0. This voltage drives MN1 and generates a current in MN1 following the MOSFET current square law [48]. MP1 senses this current and mirrors it to MP2. MN2 provides another mirror from MN1 directly. When MP3 is 'on', the current from MP2 will charge *Vc* which ramps up until it reaches the upper threshold V_{t1} of the Schmitt Trigger. This causes the inverter to flip and turn off MP3 and turn on MN3. This will allow the *Vc* to get discharged until it reaches the lower threshold, V_{t12} of Schmitt trigger which will turn MP3 back on and repeat the charging cycle.

This relaxation oscillator topology is employed due to its frequency predictability, small chip area, and low-power dissipation. Schmitt trigger is employed in this design to act as comparator with output '1' occurring when *Vc* is above the threshold V_{t1} and '0' occurring when *Vs* falls below the threshold, V_{t2} [48]. It will also provide full rail-to-rail square wave and the hysteresis is expressed as, $V_{HYS} = V_{t1} - V_{t2}$. Assuming the charging (I_{MP2}) and the discharging currents (I_{MN2}) are identical and denoted as I_C, the rise time and fall time of the charging and the discharging of the capacitor Cc are t_r and t_f, respectively, the output frequency can be expressed as:

$$f = 1/T = I_C /(2C_C V_{HYS}) = K_n * (V_{pH} + V_{SG} - V_{THN})^2 /(2C_C V_{HYS}) \tag{3-18}$$

where K_n is the MOS parameter which can be obtained from process parameters and is proportional to the W/L ratio of the device as well. V_{THN} is the threshold voltage of MN1. I_C has a parabolic relationship with the voltage V_{PH} which introduces non-linearity to the output frequency. In addition, the circuit has a very limited input range. The lower limit of V_{pH} is obtained when the PMOS threshold is very close to the NMOS threshold and can be negative which is not acceptable. The upper value of V_{pH} is limited when the current in MN1 is saturated and the drain voltage is close to V_{DD} as V_{pH} increases.

3.2.2 Power Conditioning Unit

To make a complete sensor solution, the other peripheral circuits are also needed. The power source, power conditioning unit, readout and processing unit are all crucial for a pH sensor system, which is the goal in this work.

The power for a biosensor can be from diverse sources. Battery is a popular one for portable devices. It is convenient and capable to provide good amount of power. The problem here is it has limited lifetime and needs to be replaced or recharged frequently. This makes it difficult to be used in biomedical applications, particularly in real-time monitoring scenario. Therefore, some other alternative power supplies are studies and developed recently such as inductive link [21] and photovoltaic cells [16]. Inductive link is another power source with the energy transferred from a transformer's primary coil outside to secondary coil implanted inside human body. However, the inductor is bulky, and the energy transfer efficiency degrades a lot as the distance increases. Inductive link is bulky with low efficiency. Photovoltaic cells [16] are frequently used for applications with access to the light source. Typical photovoltaic cell can provide up to several to tens of milli-watts (mW) of power. In [5], the power source is also coming from an optical power source from laser, which is also employed in this work. With a shorter channel length technology, the power source voltage range also shrinks to 1.5~1.8V. This can ensure that the entire pH sensor system can operate for a lengthy period without the need for a bulky battery or big power source.

These sources usually cannot be directly used for electronic circuits due to the fluctuations and noise on them. Therefore, an additional power conditioning unit is usually needed between these power sources and the electronic circuits. To regulate this DC signal furthermore and provide desired DC voltage level, a voltage regulator is usually employed.

Voltage regulator is one of most basic elements for a lot of systems needing a regulated power supply. It provides a regulated output supply voltage for a system with a certain output current capability. Table 3-1 shows the typical topologies employed mostly [52]. To make a brief comparison, circuit complexity, cost, topology size, noise, input/output voltage limit, efficiency are the main factors in consideration.

From the description above, linear regulator is the simplest and least expensive of the power-supply circuits. However, the input voltage must exceed output voltage, the difference between the two is added on the pass element (usually a MOSFET or BJT). With this price paid, the output voltage is monitored and gets feedback to control the pass element. But when input voltage is much higher than output, the voltage difference becomes bigger which results in bigger power loss on the element device, and the power loss sometimes can be much bigger than the effective output power.

Charge pumps are based on the principle of the electronic charge transfer between capacitors. With no inductors, the energy is transferred from the input to output via the capacitor with proper clock signals. With capacitors used, it can provide output voltage either high or lower than input.

TABLE 3-2 SUMMARY OF THE VOLTAGE REGULATOR TOPOLOGIES

Topologies	**Advantages**	**Disadvantages**
Linear regulator	• Easy to implement • Small size • Low quiescent current (Iq) • No switching noise	• VOUT < VIN • Big power loss under high Vin and/or large loads
Charge pump	• Easy to implement • Small size • Can boost or invert	• Can only support limited power • Can only support limited VIN/VOUT ratios
Step-Down (buck)	• Lowest peak current among switch-mode regulators	• VOUT < VIN • High-side FET driver is a little complex
Step-Up (boost)	• Low peak current • Simple driver (low-side driver) • Simple inductor • Low switch-stress voltage	• VOUT > VIN • VOUT is at least a diode drop below VIN • No short-circuit protection
Inverter	• Simple inductor	• Negative output only • High-side FET driver is a little complex • High peak current
Flyback	• VOUT is isolated from VIN • Can have multiple outputs • Can make step up/down, invert • Simple driver (low-side driver)	• Need transformer • High peak currents • High switch-stress voltage

Fig. 3.12 shows the brief shots of the topologies.

However, since all energy is transferred via capacitors, the output power cannot be very big due to the limited capacitor size density in a CMOS process. Since clock signals are a must (usually several phases), charge pumps create noise as they charge and discharge the capacitor(s) connected to the device. However, due to the light load limits and lack of an inductor, this noise is still smaller in magnitude than a comparable switching regulator generally.

Switch-mode regulators employ both inductor and capacitor to transfer energy from input to output. However, they are also noticeably more complex. There are several important parameters

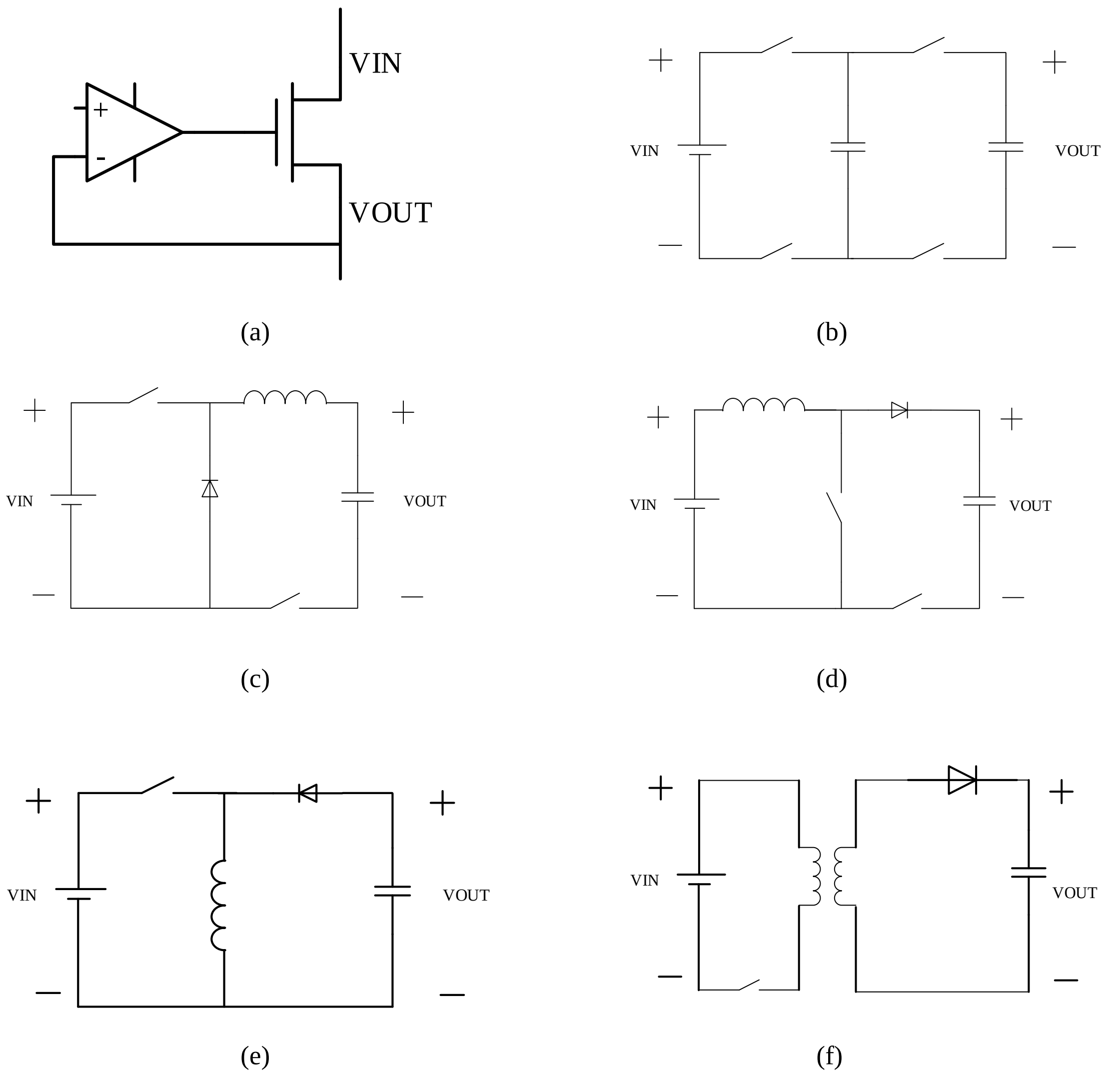

Fig. 3.12. Six typical voltage regulator topologies, (a) linear regulator, (b) charge pump, (c) step-down (Buck), (d) step-Up (Boost), (e) inverter, and (f) Flyback. The input voltage is V_{IN} and the output voltage is V_{OUT}. From (c) to (f), these four topologies are so-called "switch-mode regulators".

to choose/design to implement a switch-mode regulator, including output inductor/capacitor, output current ripples, switching frequency, voltage ratings and R_{DSON} of the power switches, and so on. With more building blocks inside, and more complex controlling methods under light/heavy loads, the switch-mode regulators usually achieve much better efficiency than the linear regulators. However, the switching mechanism still creates more considerable noise than linear counterparts, and the inductor potentially creates electro-magnetic interference (EMI) issues.

For this work, the power consumption is relatively small, and to avoid expensive inductors, only linear regulator or charge pump can be suitable. While charge pump need different clock phases, to avoid noisy clocking signals, linear regulator is selected as the voltage regulator topology employed in this work, shown in Fig. 3.13. Sometimes it is also called "low drop-out" (LDO) regulator; the name is based on the drop-out voltage on the pass element Q_0 which is a PMOS device in this situation. When input voltage is close to output voltage, the drop-out voltage is small; otherwise the power loss increases on the pass element to degrade the efficiency.

The output voltage V_{OUT} is sensed by the resistor divider and compared with the reference voltage V_{REF} which usually comes from bandgap reference. The control circuit will generate an error signal which contains the difference between the output and reference voltage and drive the pass element until V_{OUT} is equal to V_{REF}.

The design requirements for an LDO usually include the output regulation accuracy, efficiency, line regulation, load regulation, frequency response, transient response, and so on [43]. Fortunately, in this application the load current is not big (~mA range) and the transient response does not require very fast speed.

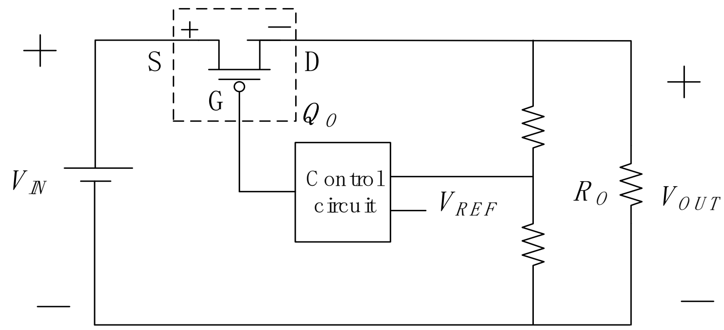

Fig. 3.13. Typical topology of a linear voltage regulator.

3.3 The proposed pH readout system

This section introduces the main two main parts in this pH readout system. One is the pH measurement circuit and the other one is the power conditioning unit. Some other auxiliary circuit such as bandgap, comparator, oscillator will be discussed in Chapter 4.

The proposed readout system is shown in Fig. 3.14. The goal of this proposed system is to achieve a complete, monolithic, low-power, high-linearity and stable pH measurement system with a power conditioning unit, and a novel pH detection circuit to cover wide range of pH levels from 0-14, while maintaining a good linearity all over the pH range.

To achieve low power, a 0.13-μm standard CMOS process is employed which enables this system working at 1.3V supply or lower. Low-power circuits are implemented to achieve functionalities. To achieve high linearity, the same coil-type electrochemical pH sensor in [16] is employed, which can provide very good linearity. Then to achieve the good linearity for the entire system, the readout circuit also needs to provide high linearity. To do that, a novel low-power pH readout circuit is proposed here to provide a low-cost solution which will be discussed in next chapter. Calibration is also implemented to help trim the output frequency and tune the sensitivity.

There is a slight difference of data communication from the previous work. The output signal from the proposed measurement system is fed to a data acquisition system with cables and then connected into a computer with LabView program to display the real-time pH monitoring.

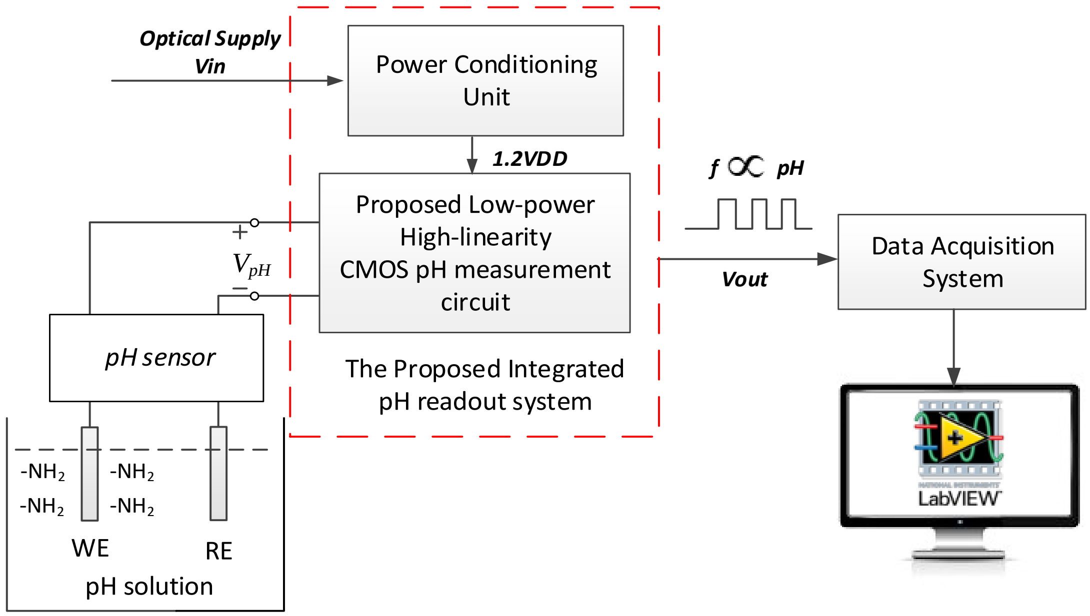

Fig. 3.14. The schematic of the proposed pH sensing and measurement system. This work is focused on the development of the monolithic pH measurement system.

Chapter 4 Design of Low-Power High-Linearity pH Readout System with Large Dynamic Range

From the previous chapter, the linearity of the pH readout system output frequency depends on the current inverted from pH sensor voltage [16], which is parabolic. When this voltage rises to certain threshold the current will go even higher which shows a big non-linearity. This non-linearity will introduce an inaccurate readout and detection of the real pH value. Therefore, good linearity is desired for the pH readout circuit.

This chapter will describe the proposed pH readout circuit with high linearity and low power. The principle will be described with a brief math derivation, and the details of the circuit is illustrated with design considerations and trade-off.

4.1 Proposed pH Measurement System Design

To overcome the non-linearity issue, a new topology is proposed in Fig. 4.1. The first state is the same as Fig. 3.12, sensed V_{PH} will be lifted by level shifter MP0, so V_1 is a PMOS threshold higher than V_{PH}. Node V_1 is buffered by an OTA and drives a resistor R_S, which creates a current through R_S directly proportional to V_1:

$$I_S = V_1 / R_S = (V_{pH} + V_{SG}) / R_S \tag{4-1}$$

Similarly, this current will be mirrored out by MP1, MP3 and MN2. Assume $I_{MP3} = I_{MN2} = Ic$. The Schmitt Trigger in the original circuit has been replaced by two comparators with an RS trigger, which can help improve the accuracy of frequency.

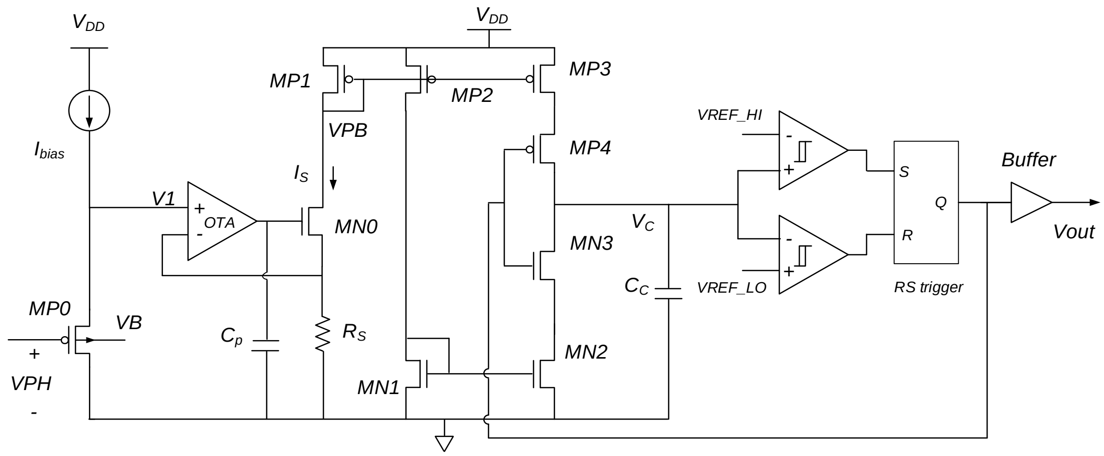

Fig. 4.1. The circuit schematic of the proposed measurement system.

The comparator reference voltages V_{REF_HI} and V_{REF_LO} are provided by the LDO output resistor divider. Schmitt Trigger has much simpler structure than a comparator; however, the trigger threshold voltages are vulnerable to process, temperature and supply voltage variations. The R_S trigger makes sure V_1 voltage will not be out of the range from V_{REF_LO} to V_{REF_HI}. With the accurate reference from the bandgap and LDO, the comparator can provide much better triggering threshold and ΔV for the readout circuit.

From previous chapter, the charging period T is given by:

$$T = t_r + t_f = 2C_1\Delta V / I_C \tag{4-2}$$

Where $\Delta V = V_{REF\_HI} - V_{REF\_LO}$.

And the output frequency, f can be expressed as:

$$f = 1/T = I_C/(2C_1\Delta V) = (V_{pH} + V_{SG})/(2R_SC_1\Delta V) \tag{4-3}$$

Therefore, the output frequency will be linearly proportional to V_{PH} voltage.

4.1.1 Small-Signal Analysis

This measurement system's small-signal analysis can be divided into three stages. The first stage can be the input PMOS MP0 with the biasing current, the second stage is the OTA and the source follower MN0 after it, which forms a small loop as well while the third stage is the oscillator loop.

From a large-signal standpoint, the output voltage is equal to the input voltage minus the gate-source voltage. The gate-source voltage consists of two parts: the threshold and the overdrive. If both parts are constant, the resulting output voltage is simply offset from the input, and the small-signal gain would be unity. Therefore, the source follows the gate, and the circuit is also known as a source follower. In practice, the body effect changes the threshold voltage, and the overdrive depends on the drain current, which changes as the output voltage changes unless $r_L \to \infty$. Furthermore, even if the current were exactly constant, the overdrive depends to some extent on the drain-source voltage unless the Early voltage is infinite.

The input stage and its small-signal equivalent circuit are shown in Fig. 4.2. Since the body terminal is not shown in Fig. 4.2 (a), we assume that the body is connected to the lowest supply voltage (ground here) to keep the source-body PN junction reverse biased. As a result, v_{bs} changes when the output changes because the source is connected to the output, and the g_{mb} generator is active in general.

For input terminals,

$$v_o = v_{sg} + v_i \tag{4-4}$$

For output terminals with assumption of $i_o = 0$,

$$g_m v_{sg} - g_{mb} v_o - v_o / r_L - v_o / r_o = 0 \tag{4-5}$$

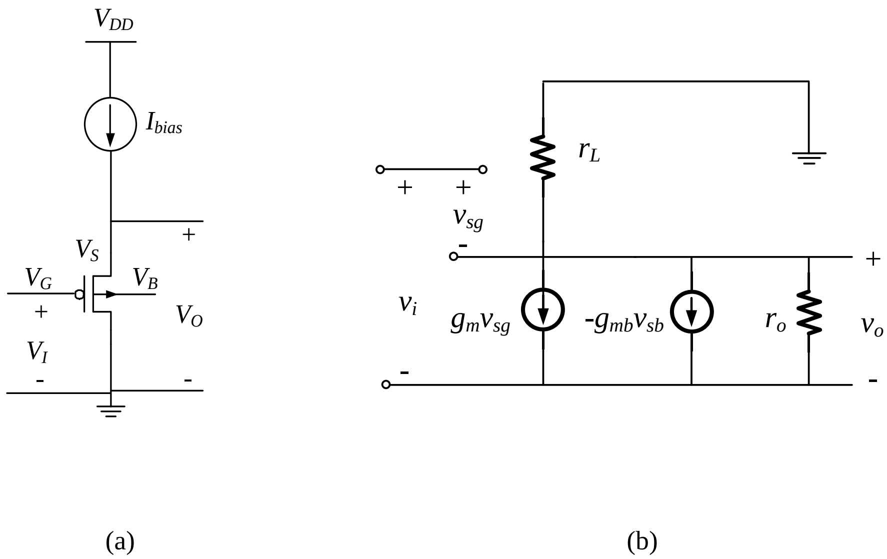

Fig. 4.2. (a) Input stage of the proposed pH readout system and (b) the small-signal equivalent circuit model with body effect.

Solving (4-4) for v_{gs}, substituting into (4-5), and rearranging gives

$$\left.\frac{v_o}{v_i}\right|_{i_o=0} = \frac{g_m}{g_m + g_{mb} + \dfrac{1}{r_L} + \dfrac{1}{r_o}} = \frac{g_m r_o}{1 + (g_m + g_{mb}) r_o + \dfrac{r_o}{r_L}} \tag{4-6}$$

In here, the r_L is the equivalent of the current source, which is usually the intrinsic resistance of a PMOS, denoted as r_o, and considered as infinite. So, equation (4-6) can be simplified to

$$\lim_{r_L \to \infty} \left.\frac{v_o}{v_i}\right|_{i_o=0} = \frac{g_m r_o}{1 + (g_m + g_{mb}) r_o + \dfrac{r_o}{r_L}} = \frac{g_m}{g_m + g_{mb}} \tag{4-7}$$

Usually the $g_m r_o$ (so-called intrinsic gain) is much higher than 1, so equation (4-7) can be further simplified to

$$\lim_{\substack{r_L \to \infty \\ g_m r_o \to \infty}} \left.\frac{v_o}{v_i}\right|_{i_o=0} = \frac{g_m}{(g_m + g_{mb})} = \frac{1}{1+\chi} \tag{4-8}$$

where χ is equal to g_{mb}/g_m, which is typically in the range of 0.1 to 0.3.

The second stage of the proposed readout system and its small signal equivalent circuit are shown in Fig. 4.3. From Fig. 4.3 (a), it begins with the output of first input stage and includes a unity buffer with an OTA and NMOS, R_S, MP1 and an extra capacitor C_P to help stabilization.

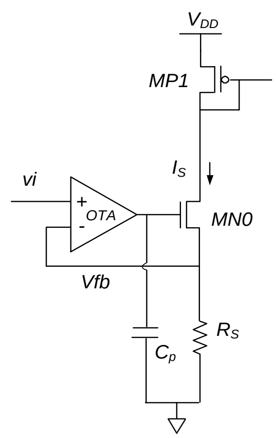

(a)

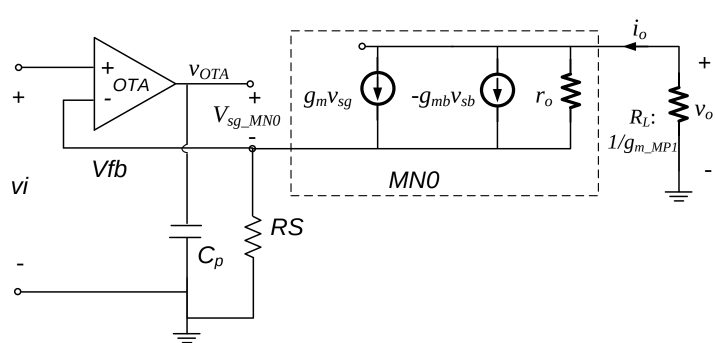

(b)

Fig. 4.3. (a) Voltage buffer including the OTA and MN0 with source degeneration R_S to generate current proportional to input voltage with MP1 as load and (b) its small signal model including body effect. MP1 is diode-connected and can be modeled as a resistor $1/g_{m\_MP1}$.

If the OTA has intrinsic gain of A, and the negative voltage is v_{fb}, the output v_{OTA} can be expressed as,

$$v_{OTA} = A(v_i - v_{fb}) \tag{4-9}$$

The output current i_o can be expressed as:

$$i_o = g_{m\_MN0}(v_{OTA} - v_{fb}) - g_{mb}v_{fb} - v_{fb}/r_o = -v_o/R_L = v_{fb}/R_S \tag{4-10}$$

The load resistor is a diode-connected MP1, which has the equivalent resistance of $1/g_{m\_MP1}$. Hence, the gain of this part can be expressed as:

$$A_v = v_o/v_i = -\frac{g_{m\_MN0}A}{g_{m\_MP1} + g_{m\_MP1}R_S(Ag_{m\_MN0} + g_{m\_MN0} + g_{mb} + \frac{1}{r_o})} \tag{4-11}$$

Here the OTA gain, A can be considered large enough (>60dB). If $AR_S g_{m\_MN0} >> 1$, which is usually easy to achieve then the equation above can be simplified as,

$$A_v = v_o/v_i = -\frac{1}{g_{m\_MP1}R_S} \tag{4-12}$$

Combining equation (4-8), the signal gain from V_{PH} to V_{PB} can be expressed as,

$$A_v = -\frac{1}{(1+\chi)g_{m\_MP1}R_S} \tag{4-13}$$

The third part includes all the circuitry from V_{PB} to *Vout*, which can be analyzed by a standard oscillator model [47, 48].

4.1.2 Input Common-Mode Range Analysis

As discussed before, the calibrated pH sensor output voltage varies from -0.5V to +0.5V. Assume the OTA has rai-to-rail input common mode range which is from 0~1.2V. Then the source voltage of MP0 in Fig. 4.3:

$$V_1 = V_{pH} + V_{THP} = V_{pH} + V_{TH0} + \gamma(\sqrt{2\phi_f + V_{SB}} - \sqrt{2\phi_f}) \tag{4-14}$$

where V_{TH0} is the threshold voltage when $V_{SB} = 0$, γ and ϕ_f are well-known process parameters. V_1 must be always positive to ensure valid operation in this topology. In sub-micron processes, the V_{TH0} can be as small as 300 mV or even lower. In such cases, when V_{PH} is -0.5V, V_{TH0} will not be able to compensate the negative voltage if $V_{SB} = 0$. Hence, the body terminal can be used to manipulate the threshold voltage and provide enough compensation to make V_1 positive.

4.2 Circuit Design

The prototype of the proposed pH sensor readout circuit is designed and simulated in a standard 0.13-µm CMOS process. Cadence Spectre™ is employed for simulation. Equation (4-3) shows a basic principle for the proposed circuit to gain good linearity. However, to achieve that, several design considerations need to be counted in the circuits design.

The first one will be MP0's threshold voltage. V_{PH} can vary from -0.5 to +0.5V for a PH value from 0 to 14 from the sensor. So V_1 can be negative with -0.5V input if the V_{GS} is too low. It'll not be a problem for a less advanced technology such as 0.5-µm, since the typical threshold voltage is usually higher than 0.5V. But for sub-micron process such as the 0.13-µm used here, a typical PMOS threshold is about 0.25V or less [53]. To make it active with -0.5V input, the V_{GS} voltage needs to be carefully designed. In the proposed circuit, a low W/L ratio is used with about 200nA current, which can give about 550mV V_{GS} for MP0.

On the other hand, when V_{PH} reaches the top limit such as +0.5V, after the level shifter, the voltage of V_1 can get very close to VDD, which can degrade the current source (push the current source PMOS into triode region) and make the V_{GS} of MP0 less than expected, and eventually affect the linearity.

So, the voltage supply has to sit with a little margin for the top limit of PH value. Here 1.2V is selected for the readout circuit which will provide good margin for the limit.

The OTA design will be another challenge as well. If the offset of the OTA is V_{OS}, and then equation 4-3 will become:

$$f = 1/T = I_C/(2C_1\Delta V) = (V_{pH} + V_{THP} + V_{OS})/(2R_S C_1 \Delta V) \tag{4-15}$$

Basically, any offset voltage V_{OS} will introduce direct non-linearity into the current generated on R_S. As mentioned before, V_1 can change from almost 0V to VDD, which is full-rail swing. So, a rail-to-rail OTA topology is a must for the OTA.

4.2.1 Comparator

Schmitt Trigger shown in Fig. 4.4 used in [16] as simple comparator to provide two threshold voltages to form ΔV. From [48], assume the high/low threshold voltages can be denoted as V_{SPH} and V_{SPL}, and the NMOS threshold voltage is V_{THN}, PMOS threshold voltage is V_{THP}. W and L are the width and length of a certain transistor, and β is the aspect ratio as W/L. Then we have:

$$\frac{\beta_1}{\beta_3} = \frac{W_1 L_3}{L_1 W_3} = [\frac{V_{DD} - V_{SPH}}{V_{SPH} - V_{THN}}]^2 \tag{4-16}$$

$$\frac{\beta_5}{\beta_6} = \frac{W_5 L_6}{L_5 W_6} = [\frac{V_{SPL}}{V_{DD} - V_{SPL} - V_{THP}}]^2 \tag{4-17}$$

It can be concluded both V_{SPH} and V_{SPL} are depending on threshold voltage, which is subject to the process and temperature variations.

In this work, two separate comparators are employed here to provide better control for the trigger threshold voltages. Fig 4.5 shows the comparator schematic. It is a typical PMOS type input pair structure. Hysteresis is added through MN3, which is adding more current to MN2 to twist the gain stage when output flips, which is similar with the way in the comparator reported in [54]. When *V+* is less than *V-*, the nets '*n1*' and '*n3*' are low level, MN4 is off; when *V+* is passing V-, n1 and n3 will flip quickly due to high gain and turn on MN4 and MN3 will add offset loading to MP2 and then hysteresis is formed and prevent output flipping back and forth. The offset voltage simulated is about 25mV and the propagation delay from input to output is 35ns, measured from when V+ is 5mV higher than V- to *Vout* flips from '0' to '1'.

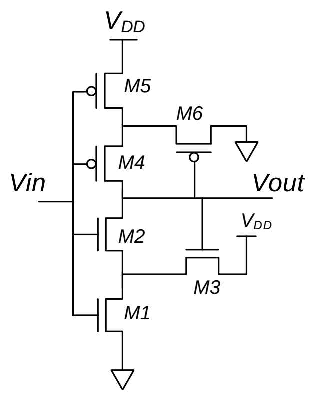

Fig. 4.4. Schematic of the CMOS Schmitt Trigger in [16].

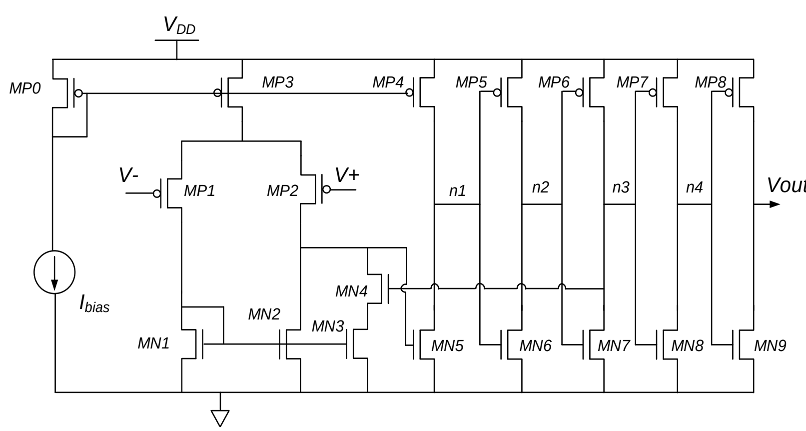

Fig. 4.5. Schematic of the comparator used in the pH circuit.

4.2.2 OTA

The operational transconductance amplifier (OTA) used in this system needs to be able to operate at low power supply voltage with low quiescent current. What's more important is it needs to work with rail-to-rail input voltage range.

The topology of the OTA is shown in Fig. 4.6. It has two pairs of input to cover rail-to-rail input common mode range. To realize high gain without eat up too much output headroom, a folded-cascode like gain stage is employed here. MN7 and MP8 are sized carefully to bias MN8 and MP9, to make sure *Vout* can vary from [$V_{DS,SAT\_MN8} + V_{DS,SAT\_MN10}$] to [$V_{DD} - (V_{DS,SAT\_MP7} + V_{DS,SAT\_MP9})$].

4.2.3 Voltage Regulator

The voltage regulator, in here also can be called low drop-out (LDO) regulator is used to generate a regulated stable output for the pH sensor readout circuit [55]. In this sensor system, the input source is coming from the solar cells which have 4 cells and each cell outputs 0.5V nominally.

However, under higher load, the LDO can be overloaded and each cell output drops. Fortunately, the total power consumption for the sensor system is very small in terms of overloading the solar cells, usually small than 5mA.

LDO usually is composed of two parts: error amplifier and output stage. Error amplifier needs a reference voltage and senses the difference between reference and feedback voltage and generate an output drive signal to drive the pass device. Under regulation, the output feedback voltage to equal the reference. The output stage burns as much current as the loads requires if it is not overloaded. But the error amplifier itself consumes certain power to maintain regulation. Hence, it is desirable to have as much low quiescent current as possible. Fig. 4.7 shows the topology of the LDO design in this readout circuit.

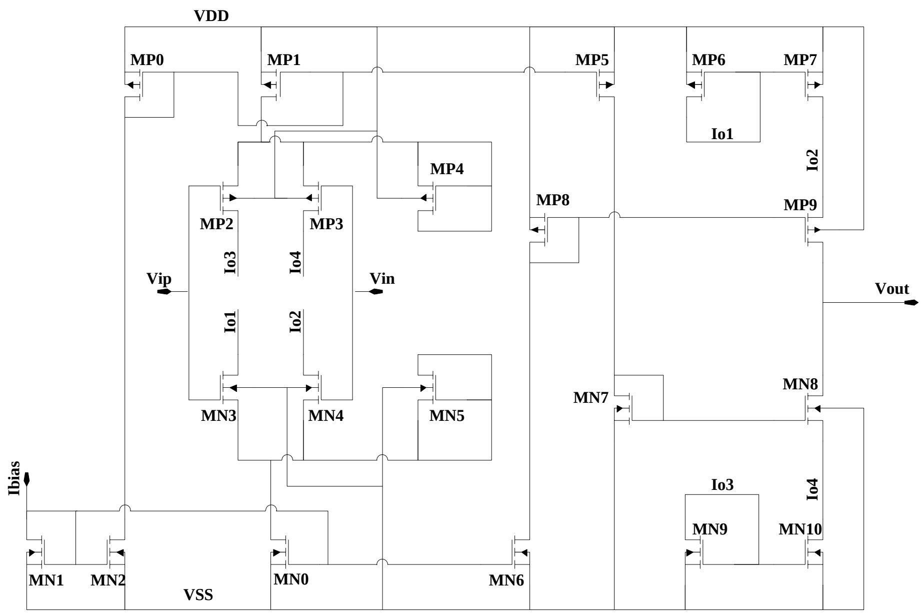

Fig. 4.6. Schematic of the OTA used in the pH circuit.

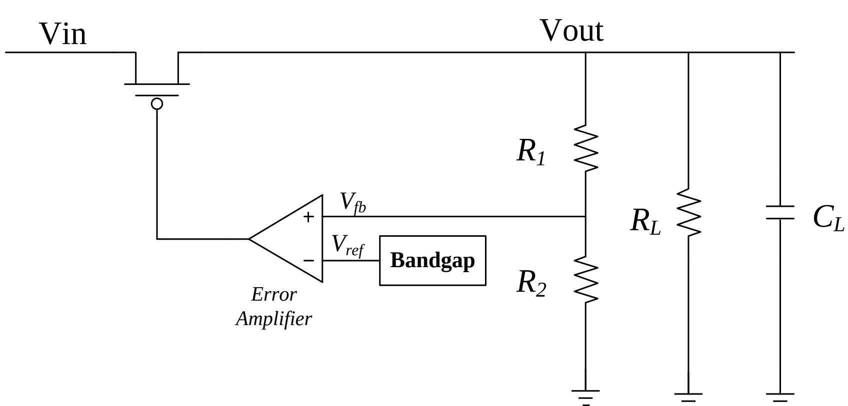

Fig. 4.7. Typical topology of an LDO.

Bandgap reference shown in Fig. 4.8 becomes a challenge in short channel process, due to the limitation of the power supply, and the shrunk channel length caused intrinsic gain reduction.

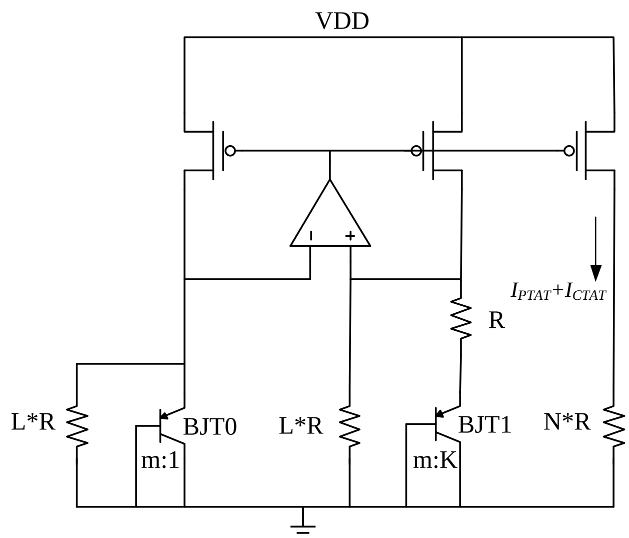

Fig. 4.8. Low supply voltage bandgap reference circuit.

$$I_{PTAT} = nV_T * \ln K \tag{4-18}$$

Where V_T is the thermal voltage, n is the thermal coefficient. K is the base area ratio of the two bipolars BJT0 and BJT1. The current through the added resistors (the CTAT portion of the circuit) is:

$$I_{CTAT} = \frac{V_{BJT1}}{L * R} \tag{4-19}$$

The total current is driven through the N*R to generate the reference voltage:

$$V_{REF} = nV_T * N * \ln K + \frac{N}{L} V_{BJT1} \tag{4-20}$$

So, the temperature behavior of the bandgap is:

$$\frac{\partial V_{REF}}{\partial T} = n*N*\ln K*\frac{\partial V_T}{\partial T} + \frac{N}{L}\frac{\partial V_{BJT0}}{\partial T} = n*N*\ln K*\frac{k}{q} + \frac{N}{L}\frac{\partial V_{BJT0}}{\partial T} \qquad (4\text{-}21)$$

k/q term is well-known as a constant about 0.085mV/C. $\frac{\partial V_{BJT0}}{\partial T}$ is negative value and varies upon different processes. In this CMOS process employed, this value is about -1.6mV/^{o}C. Give these numbers, to make zero temperature coefficient (TC), the L can be expressed as:

$$L = \frac{1.6}{n \ln K * 0.085} \qquad (4\text{-}22)$$

K = 8 is used in this circuit for good matching in layout. Then the N value can be obtained by:

$$N = \frac{V_{ref}}{nV_T \ln K + V_{D1}/L} \qquad (4\text{-}23)$$

This is desirable because it gives a formula to generate a good range of reference voltage needed. This topology is specially designed for low voltage supply in sub-micron process. The two current mirrors MP0 and MP1 generate IPTAT current in order to create the thermal voltage term. However, usually in sub-micron technology, the current mirror mismatch also increases and becomes significant. Hence, the OTA A0 is added to regulate the drains of MP0 (V_-) and MP1 (V_+) equal to make sure the current generated by the current mirrors stays identical.

$$V_{REF} = nV_T * N * \ln K + \frac{N}{L} V_{BJT1} \qquad (4\text{-}24)$$

Here V_T is the thermal voltage denoted as kT/q which provides a positive temperature coefficient around 0.085mV/^{o}C, while the VBJT1 is negatively proportional to temperature which is about -1.6mV/^{o}C in this CMOS process employed. With the two complementary terms combined the bandgap voltage is obtained constantly regardless of the temperature variations.

Fig. 4.9 shows the details of the LDO circuit with built-in bandgap circuit. Basically, this is a low supply voltage, so an OTA is employed to enhance the current mirror accuracy. The nominal output of the bandgap (BGR_OUT) is about 0.53V.

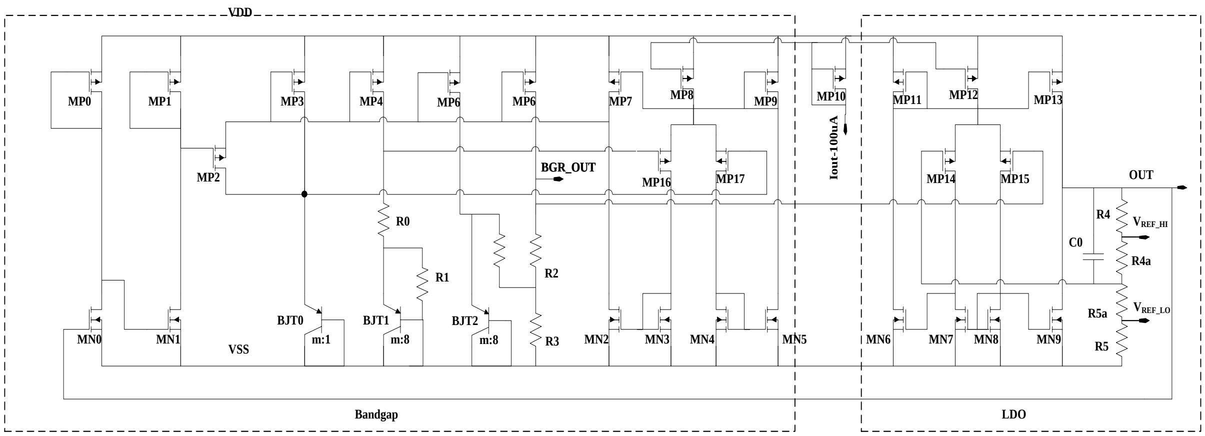

Fig. 4.9. Schematic of low voltage, high PSRR LDO with bandgap reference circuit.

Fig. 4.10 shows the essential elements of a linear regulator [45]. The error amplifier is modeled by a transconductor (g_m) with a load comprised of capacitor C_{par} and resistor R_{par}. The series pass element (MOS transistor) is modeled by a small signal model with transconductance gp. An output capacitor C_o with an equivalent series resistor (R_{ESR}) and a bypass capacitor C_b is added.

From Fig. 4.10, the output impedance is given by:

$$\begin{aligned} Z_O &= R_{12p} \parallel (R_{ESR} + \frac{1}{sC_O}) \parallel \frac{1}{sC_b} \\ &= \frac{R_{12p}(1 + sR_{ESR}C_O)}{s^2 R_{12p} R_{ESR} C_O C_b + s[(R_{12p} + R_{ESR})C_O + R_{12p} C_b] + 1} \end{aligned} \tag{4-25}$$

where $R_{12p} = R_{ds} \parallel (R_1 + R_2) \approx R_{ds}$.

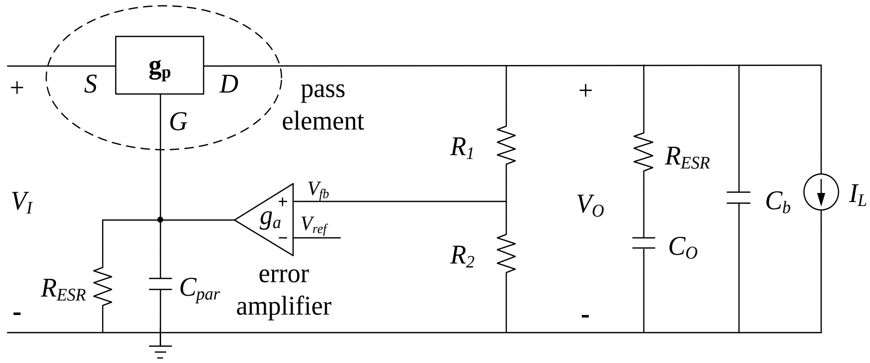

(a)

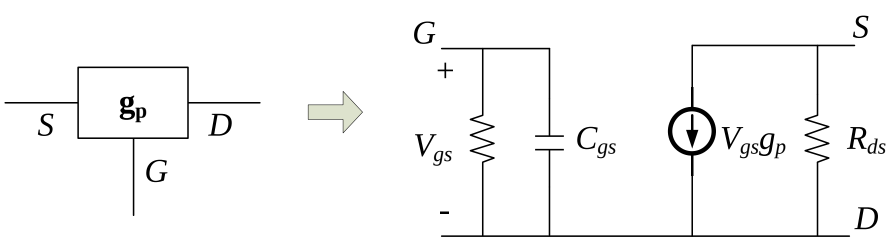

(b)

Fig. 4.10. (a) Small-signal model of a typical LDO, and (b) pass element small-signal model.

Typically, the output capacitor value C_O is considerably larger than the bypass capacitor C_b. Thus, the output impedance Z_O approximates to:

$$Z_O = \frac{R_{ds}(1+sR_{ESR}C_O)}{[1+s(R_{ds}+R_{ESR})C_O]\times[1+s(R_{ds}\parallel R_{ESR})C_b]} \tag{4-26}$$

From the equation above, a part of the overall open-loop transfer function for the regulator is obtained, and the zero and poles can be found. The first pole is

$$P_0 : s(R_{ds}+R_{ESR})C_O = -1 \tag{4-27}$$

Therefore, $f_{p_0} = -\dfrac{1}{2\pi(R_{ds}+R_{ESR})C_O} \approx -\dfrac{1}{2\pi R_{ds} C_O}$ (because $R_{ds} >> R_{ESR}$).

The second pole is obtained from equation (4-25) again,

$$P_b : s(R_{ds}+R_{ESR})C_b = -1 \tag{4-28}$$

Therefore,

$$f_{pb} = \frac{-1}{2\pi(R_{ds} \parallel R_{ESR})C_b} \approx \frac{-1}{2\pi R_{ESR} C_b} \tag{4-29}$$

The zero is $Z_{ESR} : sR_{ESR}C_O = -1$.

Therefore,

$$f_{Z(ESR)} = \frac{-1}{2\pi R_{ESR} C_O} \tag{4-30}$$

In addition, another pole exists from the input impedance of the pass element (i.e. the output impedance of the amplifier, R_{par}, C_{par}). The approximated poles and the zero are then given by,

$$P_O = \frac{1}{2\pi R_{ds} C_O} \approx \frac{I_L}{2\pi V_A C_O} \tag{4-31}$$

$$P_b = \frac{1}{2\pi R_{ESR} C_b} \tag{4-32}$$

$$P_a = \frac{1}{2\pi R_{par} C_{par}} \tag{4-33}$$

$$Z_{ESR} \approx \frac{1}{2\pi R_{ESR} C_O} \tag{4-34}$$

where $R_{ds} \approx \dfrac{V_A}{I_L}$, $V_A = \dfrac{1}{\lambda}$ for MOS device, λ is the channel-length modulation parameter. Pole Pa is the only one introduced at the input of the pass device, not at the output of the device. Fig. 4.11

illustrates the typical frequency response of the LDO voltage regulator.

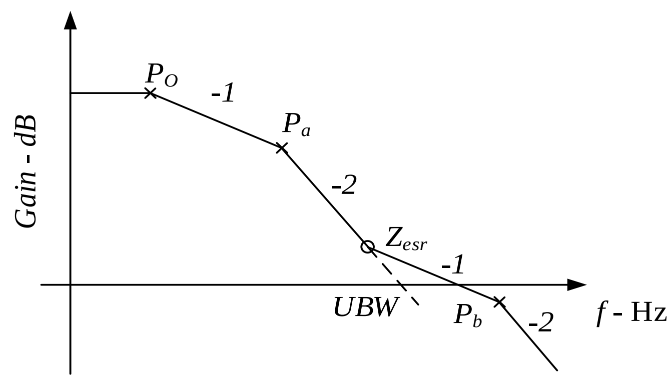

Fig. 4.11. Frequency response of the LDO voltage regulator.

From the poles/zero location, a zero is needed to stabilize the loop. Fortunately, the ESR zero can be used to do this job if the ESR zero is set correctly. From Fig. 4.11, if there is no zero, then UBW is obtained when the -40 dB/dec slope curves intercept the x-axis. Hence, the zero has to be lower than UBW to do the compensation.

Simulation of the LDO is performed with Cadence Spectre™ tool, including the line and load responses, as shown in Fig. 4.12. From the simulation, the LDO output is observed to be regulated at 1.25V, the voltage variations are less than 5mV with or without the load. In addition, overshoot and undershoot in both line and load responses are less than 15mV.

4.2.4 Output Error and Calibration

There are several sources of error contributions. If we count all the main sources, equation (4-15) can be re-derived as:

$$f = \frac{(V_{pH} + V_{SG} + \Delta V_{SG} + V_{OS})}{2(R_S + \Delta R)(C_C + \Delta C)(V_{HYS} + \Delta V)} \tag{4-35}$$

where ΔV_{SG}, ΔR, ΔC, ΔV are the variations of the parameter V_{SG}, Rs, C_C, V_{HYS} respectively

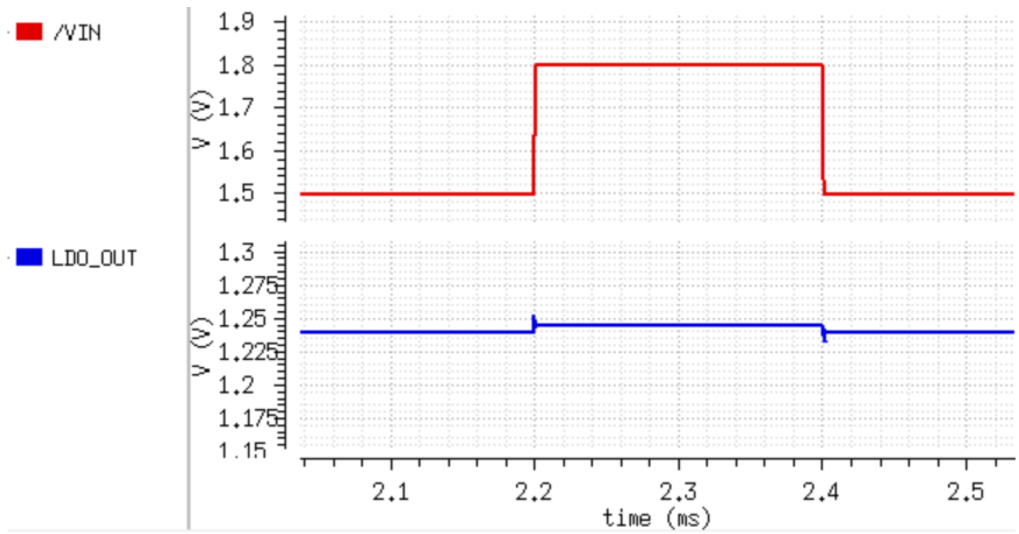

(a) Line regulation response with load current set to 1mA.

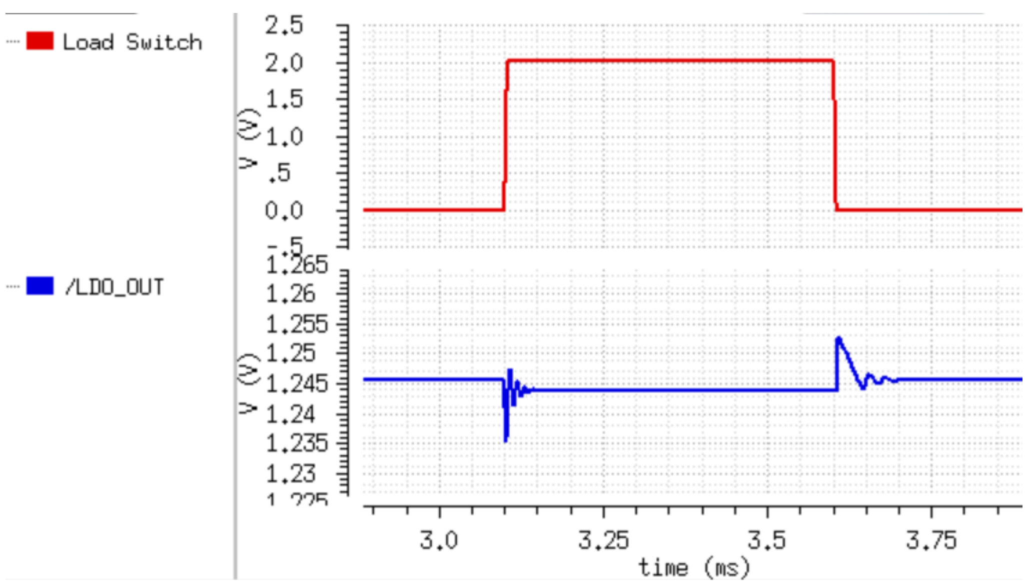

(b) Load regulation response, with 0~5mA load pulse. Vin is set 1.5V.

Fig. 4.12. LDO simulation with Cadence Spectre™, with (a) line regulation (b) load regulation.

over the process, voltage supply and temperature (PVT) corners, V_{OS} represents the offset voltage of the OTA. These variations can contribute to the output frequency gain.

If we look at the output frequency to input voltage gain from equation (5), we can have:

$$\frac{\partial f}{\partial V_{pH}} = \frac{1}{2(R_S + \Delta R)(C_C + \Delta C)(V_{HYS} + \Delta V)} \tag{4-36}$$

As expected, the gain is constant without PVT variation. So theoretically all the variation can be trimmed with two steps described as below. Thanks to the digital signal process software developed in LabView^{TM}, it is very simple to calibrate this circuit over PVT corners, to have a constant output frequency gain and constant frequency value for a certain input voltage. Fig. 4.13 shows the proposed circuit with calibration part.

Step1: it will need to calibrate the gain first, which means to calibrate the denominator term in equation (5). Three digital bits are added to tune C_C (tuning Rs will be another option) with binary weight and LSB of 1/8*C_C. Use the nominal value from the simulation to calculate the term in (5). In the real silicon, set V_{pH} = 0V as first point to read the frequency f_0 from LabView; then set V_{pH} = 0.1V. According to (5), calculate the target frequency value f_t with 0.1V V_{pH} and sweep the code [bv2:bv0] monotonically until the read frequency is above target frequency. Then latch this code to <bv2:bv0>. This ensures the calibrated gain error is less than 1 LSB (bv0).

Step 2: with the gain trimmed, this step is to calibrate the numerator in equation (5). Similarly, I_{bias} also has three bits <bi2:bi0> with binary weight to tune V_{SG} of MN1. Set V_{pH} = 0V, and then sweep <bi2:bi0> from 000 to 111, output frequency will be gradually reduced until it is below the target frequency. Then latch this code to <bi2:bi0>. This ensures the absolute frequency is within 1 LSB (bi0). Therefore, <bv2:bv0> <bi2:bi0> will be used to burn into memory cell such as EEPROM which is available in most of the standard CMOS processes.

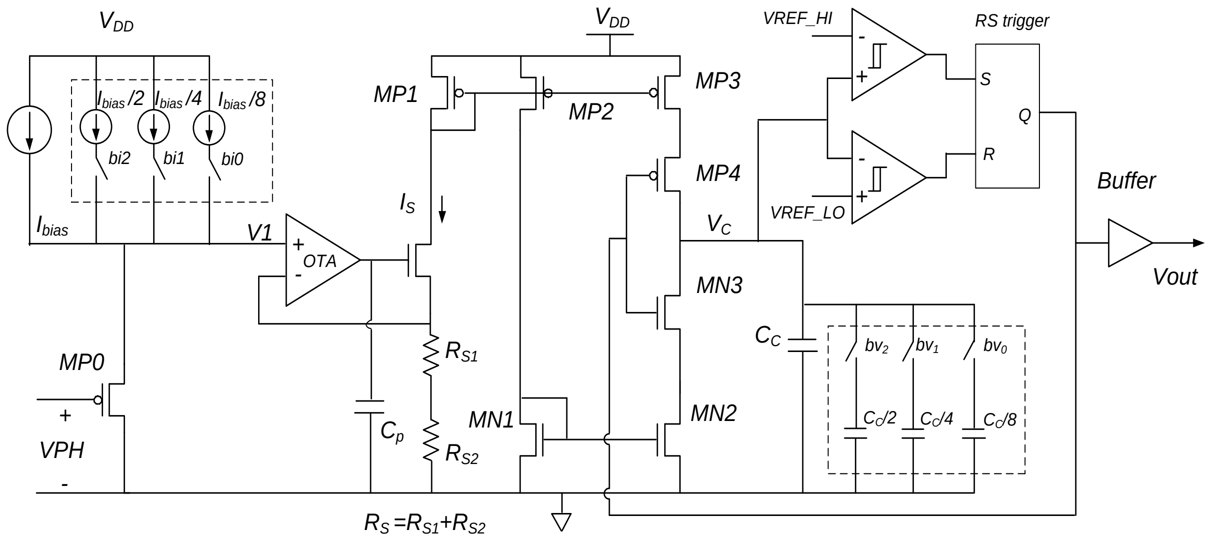

Fig. 4.13. Proposed pH sensor readout circuit with calibration scheme.

Table 4-1 shows the output frequency from both measurement and ideal. The ideal frequency is calculated based on the slope around 0V pH sensor voltage, which should give a constant slope all over the range. It can be found the measured frequency shows a big error at -0.5V, but still good linearity at 0.6V, which gives a good reason needing calibration. The calibration result gives much better frequency variations at -0.5V and also introduces bigger errors at +0.5V and more, which is expected and still acceptable from -0.5V ~ +0.5V.

4.2.5 Effect of Noise on the Output Frequency Accuracy

Noise is ubiquitous in circuits. According the sources, noise can be sorted into several types. But the main noise sources are thermal, flicker (1/*f*), shot, burst, transit-time noise [56]. However, the most significant contributors are thermal and flicker noises. Thermal noise is generated by the random motion of electrons in a conductor, which introduces fluctuations in the voltage measured

TABLE 4-1 ERRORS IN OUTPUT AT DIFFERENT pH VALUES

pH voltage (V)	**pH value**	**Ideal Freq. (KHz)**	**Measured Freq. (KHz)**	**Output freq. error (%)**	**Error after cal.**
-0.5	0	1	1.686	68	9.5
-0.36	2	2.64	2.66	3	3.5
-0.21	4	4.29	4.26	0.45	1
-0.07	7	6.6	6.62	0	0.2
0.21	10	8.95	9.02	1.1	1.5
0.36	12	10.56	10.7	1.4	2
0.5	14	12.1	12.3	1.65	3
0.57	15	12.87	13.02	1.2	10
0.6	16	13.2	13.35	1.2	20

across the conductor even if the average current is zero. In this work it exists in the resistors and transistors. Flicker noise, also known as $1/f$ noise, is a signal or process with a frequency spectrum that falls off steadily into the higher frequencies, with a pink spectrum. It occurs in almost all electronic devices, and results from a variety of effects. A main source of flicker noise is believed from the charge carriers move at the interface between the gate oxide and the silicon substrate in a MOSFET, where some charge carriers are randomly trapped and later released by such energy states [57]. To analyze the noise effect to the oscillator output frequency, the readout circuit is divided by three parts: level shifter, OTA, and current mirror.

Level Shifter

The level shifter here is a PMOS source follower. Consider the source follower depicted in Fig. 4.14, where M2 serves as the bias current source. Since the input impedance of the circuit is quite high, even at relatively high frequencies, the input-referred noise current can usually be neglected for moderate driving source impedances.

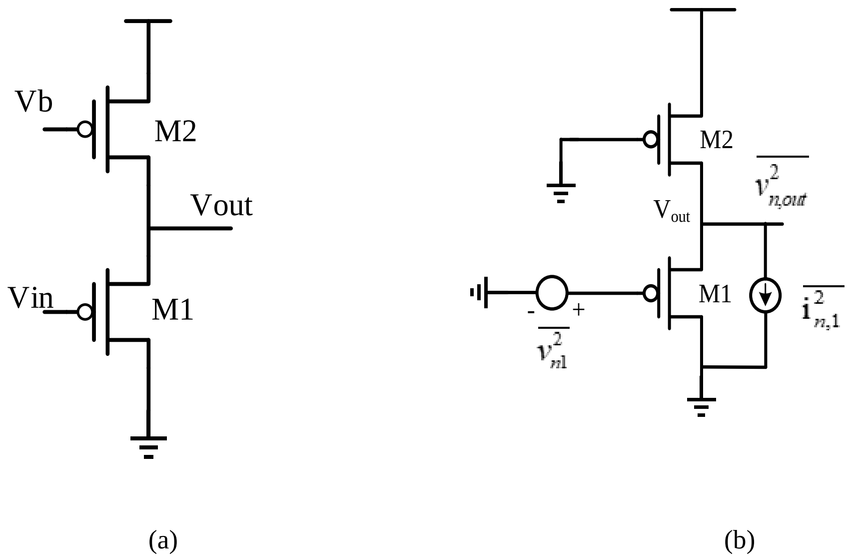

Fig. 4.14. **(a)** Basic level shifter structure and (b) noise model for the level shifter device.

To compute the input-referred thermal noise voltage, using Fig. 4.14, the output noise can be derived as:

$$\overline{v_{n,out}^2\Big|_{M2}} = \overline{I_{n,2}^2}\left(\frac{1}{g_{m1}} // \frac{1}{g_{mb1}} // r_{o1} // r_{o2}\right)^2 \tag{4-37}$$

The voltage gain is about

$$A_v = \frac{\frac{1}{g_{mb1}} // r_{o1} // r_{o2}}{\frac{1}{g_{mb1}} // r_{o1} // r_{o2} + \frac{1}{g_{m1}}} \tag{4-38}$$

Thus, the total input-referred noise voltage is:

$$\overline{v_{n,in}^2} = \overline{v_{n,1}^2} + \frac{\overline{v_{n,out}^2\Big|_{M2}}}{A_v^2} = 4kT\frac{2}{3}\left(\frac{1}{g_{m1}} + \frac{g_{m2}}{g_{m1}^2}\right) \tag{4-39}$$

In this work in Fig. 4.13, the noise at node V_1 is about (assume level shifter gain is 1),

$$\overline{v_{n,out}^2\Big|_{M2}} = 4\mathrm{k}T\frac{2}{3}(\frac{1}{g_{mp0}} + \frac{g_{m\mathrm{bias}}}{g_{mp0}^2}) \tag{4-40}$$

The flicker noise can be expressed as:

$$\overline{v_{n,out}^2} = \frac{K}{C_{ox}(WL)_1}\frac{1}{f}(g_{m1}R_{out})^2 + \frac{K}{C_{ox}(WL)_2}\frac{1}{f}(g_{m2}R_{out})^2 \tag{4-41}$$

$$R_{out} = (\frac{1}{g_{m1}} \| \frac{1}{g_{mb1}} \| r_{o1} \| r_{o2}) \tag{4-42}$$

$$\overline{v_{n,in}^2} = \frac{\overline{v_{n,out}^2}}{A_v^2} = \frac{K}{C_{ox}f}[\frac{1}{(WL)_1} + \frac{g_{m2}^2}{(WL)_2 g_{m1}^2}] \tag{4-43}$$

Hence, the total input referred noise spectrum density is:

$$\overline{v_{n,in}^2} = 4kT\frac{2}{3}(\frac{1}{g_{m1}} + \frac{g_{m2}}{g_{m1}^2}) + \frac{K}{C_{ox}f}[\frac{1}{(WL)_1} + \frac{g_{m2}^2}{(WL)_2 g_{m1}^2}] \tag{4-44}$$

OTA Noise

Folded-cascode provides high output impedance and voltage gain, with self-stable feature. However, the noise performance is a little higher than conventional amplifier without cascode topology. The noise analysis is started with a basic cascode structure shown in Fig. 4.15.

From Fig. 4.15(b), at low frequencies, the noise currents of M1 and R_D flow through R_D, the noise contributed by these two devices is quantified as in a common-source stage:

$$\overline{v_{n,in}^2\Big|_{M_1,R_D}} = 4kT(\frac{2}{3g_{m1}} + \frac{1}{g_{m1}^2 R_D}) \tag{4-45}$$

where 1/*f* noise of M1 is ignored.

M2 contributes negligibly to noise at the output, especially at low frequencies. If channel-length modulation of M1 is neglected, then $I_{n2} + I_{D2} = 0$ and hence M2 does not affect $V_{n,out}$. From another perspective, in the equivalent circuit of Fig. 4.15 (b), voltage gain from V_{n2} to the output is small if impedance at node 'x' is large, which plays as a source degeneration effect.

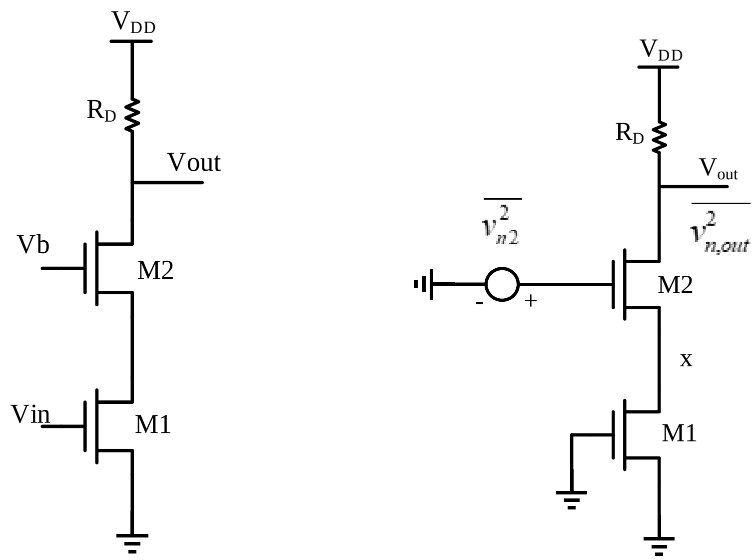

(a) (b)

Fig. 4.15. (a) Basic cascode structure and (b) noise model for cascode device (b)

Then a simple conclusion about the cascode structure is, the flicker noise can be ignored. Back to Fig. 4.6, we can divide the noise analysis into thermal and flicker noise part.

The n-type input pair MN3/MN4 produces an output current given by,

$$i_{o1} = g_{mn3} v_{n,mn3} \tag{4-46}$$

Similarly, the other p-type input pair MP2/MP3 produces:

$$i_{o2} = g_{mp2} v_{n,mp2} \tag{4-47}$$

Here, it is assumed g_{m3} has same value with g_{m4}. Same assumption applies for MP2/MP3, MP6/MP7. MP6 and MP7 generates an output current,

$$i_{o6} = g_{\mathrm{mp}6} v_{n,\mathrm{mp}6} \tag{4-48}$$

Similarly, for MN9, MN10, each generates,

$$i_{o9} = g_{m\mathrm{n}9} v_{n,m\mathrm{n}9} \tag{4-49}$$

Neglecting all noise contributions of the cascode devices at low and medium frequencies, the output noise current can be expressed as,

$$i_{out}^2 = 2(i_{o1}^2 + i_{o3}^2 + i_{o6}^2 + i_{o9}^2) \tag{4-50}$$

The same analysis applies for the p-type input pair M1/M2, so the output referred thermal noise current spectral density is,

$$i_{o,tot}^2 = 2(g_{\mathrm{mp}2}^2 v_{n,\mathrm{mp}2}^2 + g_{mn3}^2 v_{n,mn3}^2 + g_{m6}^2 v_{n6}^2 + g_{m9}^2 v_{n9}^2) \tag{4-51}$$

Therefore, the total input referred thermal noise density becomes,

$$v_{eq,in}^2 = \frac{2(g_{mn3}^2 v_{n,mn3}^2 + g_{mp6}^2 v_{n,mp6}^2)}{g_{mn3}^2} + \frac{2(g_{mp2}^2 v_{n,mp2}^2 + g_{mn9}^2 v_{n,mn9}^2)}{g_{\mathrm{mp}2}^2} \tag{4-52}$$

Hence, it is helpful to improve noise if g_{mp2} and g_{mn3} are large and smaller g_{mp6} and g_{mn9} can help reduce noise as well.

For flicker noise, the input pair contributes,

$$\overline{v_{n,in}^2} = \frac{K}{C_{ox} W L f} \tag{4-53}$$

Considering the other devices, the input referred flicker noise voltage spectrum density is the summation of only the devices that contributing flicker noise [57]:

$$\overline{v_{n,in,1/f}^2} = 2[\overline{v_{n,MN3}^2} + \overline{v_{n,MP2}^2} + \overline{v_{n,MN10}^2} g_{m,MN10}^2 (\frac{1}{g_{m,MN3}^2} + \frac{1}{g_{m,MP2}^2}) + \overline{v_{n,MP7}^2} g_{m,MP7}^2 (\frac{1}{g_{m,MN3}^2} + \frac{1}{g_{m,MP2}^2})]$$

$$= 2[\overline{v_{n,MN3}^2} + \overline{v_{n,MP2}^2} + (\overline{v_{n,MN10}^2} g_{m,MN10}^2 + \overline{v_{n,MP7}^2} g_{m,MP7}^2)(\frac{1}{g_{m,MN3}^2} + \frac{1}{g_{m,MP2}^2})]$$

(4-54)

Thus, adding thermal noise part, the total noise spectrum density is,

$$\overline{v_{n,tot}^2} = \frac{16}{3} kT \ (1 + \frac{g_{mp6}^2}{g_{mn3}^2}) + \frac{16}{3} kT \ (1 + \frac{g_{mn9}^2}{g_{mp2}^2})$$

$$+ \frac{2K_{MN3}}{C_{ox} W_{MN3} f} [\frac{1}{L_{MN3}} + (\frac{K_{MP7}\mu_n}{K_{MN3}\mu_p})(\frac{I_{MP7}}{I_{MN3}}) \frac{L_{MN3}}{L_{MN10}^2} + (\frac{K_{MN10}}{K_{MN3}})(\frac{I_{MN10}}{I_{MN3}}) \frac{L_{MN3}}{L_{MN10}^2}]$$

$$+ \frac{2K_{MP2}}{C_{ox} W_{MP2} f} [\frac{1}{L_{MP2}} + (\frac{K_{MP7}}{K_{MP2}})(\frac{I_{MP7}}{I_{MP2}}) \frac{L_{MP2}}{L_{MP7}^2} + (\frac{K_{MN10}\mu_p}{K_{MP2}\mu_n})(\frac{I_{MN10}}{I_{MP2}}) \frac{L_{MP2}}{L_{MN10}^2}]$$

(4-55)

Current Mirror Noise

The current mirror noise model is shown in Fig. 4.16.

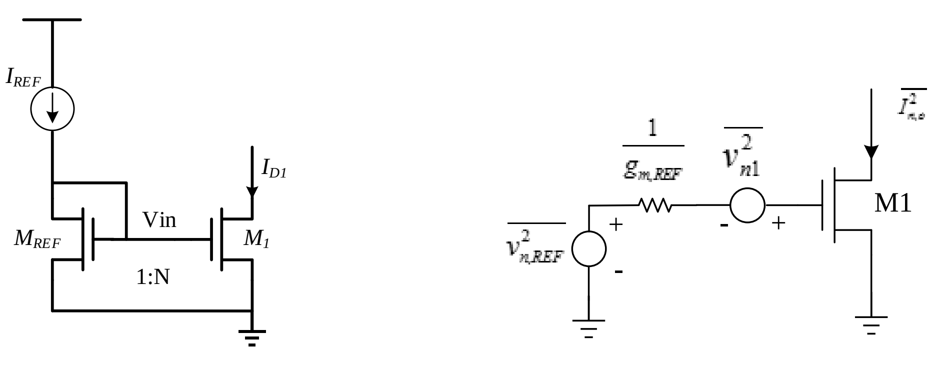

(a) (b)

Fig. 4.16. (a) Basic current mirror structure and (b) circuit model for noise analysis.

Assume the current mirror reference device M_{REF} has $g_{m,REF}$ as its transconductance. The noise voltage is $V_{n,REF}$, and the equivalent resistance is $1/g_{m,REF}$. The noise voltage at node V_{in} and V_{n1} add and drive the gate of *M1* producing,

$$\overline{I_{n,out}^2} = (\overline{V_{n,REF}^2} + \overline{V_{n1}^2})\ g_{m1}^2 \tag{4-56}$$

Since $(W/L)_1 = N(W/L)_{REF}$, and in here $L_1 = L_{REF}$, so we observe

$$\overline{V_{n,REF}^2} = N\overline{V_{n1}^2} \tag{4-57}$$

In this work, N = 2, so it follows that

$$\overline{I_{n,out}^2} = 3g_{m1}^2\overline{V_{n1}^2} \tag{4-58}$$

where $\overline{I_{n,out}^2} = 3g_{m1}^2\overline{V_{n1}^2}$ can be simply expressed as,

$$\overline{v_{n,1}^2} = 4kT\frac{2}{3g_{m1}} + \frac{K}{C_{ox}WLf} \tag{4-59}$$

Hence for current mirror, the noise current is simply coupled to output with the gain of the current mirror ratio.

Back to the readout circuit, from the previous noise analysis, the total noise is accumulated by level shifter, OTA, current mirror contributes,

$$\overline{v_{n,out}^2}\Big|_{\mathrm{tot}} = \overline{V_{n,1}^2} + \overline{V_{n,\mathrm{OTA}}^2} + \overline{V_{n,RS}^2} + \overline{V_{n,M\mathrm{P}1}^2} + \overline{V_{n,M\mathrm{P}2}^2} + \sum_{\mathrm{x}=0}^{4}\overline{V_{n,MNx}^2} \tag{4-60}$$

From the analysis, the whole readout circuit has noise sources mainly from level shifter, OTA, and current mirrors which do not have high gain or large noise contributors. Fig. 4. 17 shows the simulated input-referred noise with unit of $V/\sqrt{Hz}$. The $1/f$ corner frequency is around 1KHz.

Considering the interested bandwidth is less than 1MHz, the total noise from 1Hz to 1MHz bandwidth is about 220 μV level. Compared with the voltage -500mV ~ +500mV range, the noise contribution can still be ignored.

4.2.6 Temperature Effect

The MOSFET threshold voltage is given by:

$$V_T = V_{FB} + 2\phi_F + \gamma\sqrt{2\phi_F} \tag{4-61}$$

where $V_{FB} = \phi_{\mathrm{gs}} - (Q_{SS}/C_{ox})$ is the flat band voltage, with the gate-substrate contact potential $\phi_{\mathrm{gs}} = \phi_{\mathrm{T}} * \ln(N_A N_G / n_i^2)$. N_A and N_G are the substrate and gate doping concentrations, respectively, Q_{SS} is the surface charge density and C_{ox} is the oxide capacitance; $\gamma = C_{ox}(2q\varepsilon_{Si} NA)^{0.5}$ is a body effect parameter, with ε_{Si} the relative permittivity of Si; $\phi_{\mathrm{F}} = \phi_{\mathrm{T}} * \ln(N_A / n_i)$ is the Fermi energy with the thermal voltage $\phi_{\mathrm{T}} = kT/q$, and n_i is the intrinsic carrier concentration of Si.

Of the parameters in (4-61), ϕ_{gs} and ϕ_{F} vary with temperature (each contains ϕ_{T} and ni terms). The threshold voltage temperature dependence $\partial V_T/\partial T$ may thus be written as [11]:

$$\frac{\partial V_T}{\partial T} = \frac{\partial \phi_{gs}}{\partial T} + 2\frac{\partial \phi_F}{\partial T} + \frac{\gamma}{\sqrt{2\phi_F}}\frac{\partial \phi_F}{\partial T} \tag{4-62}$$

where the temperature dependencies of ϕ_{gs} and ϕ_{F} are:

$$\frac{\partial \phi_{gs}}{\partial T} = \frac{1}{T}(\phi_{gs} + \frac{E_{G0}}{q} + \frac{3kT}{q}) \tag{4-63}$$

$$\frac{\partial \phi_{\mathrm{F}}}{\partial T} = \frac{1}{T}[\phi_F - (\frac{E_{G0}}{2q} + \frac{3kT}{2q})] \tag{4-64}$$

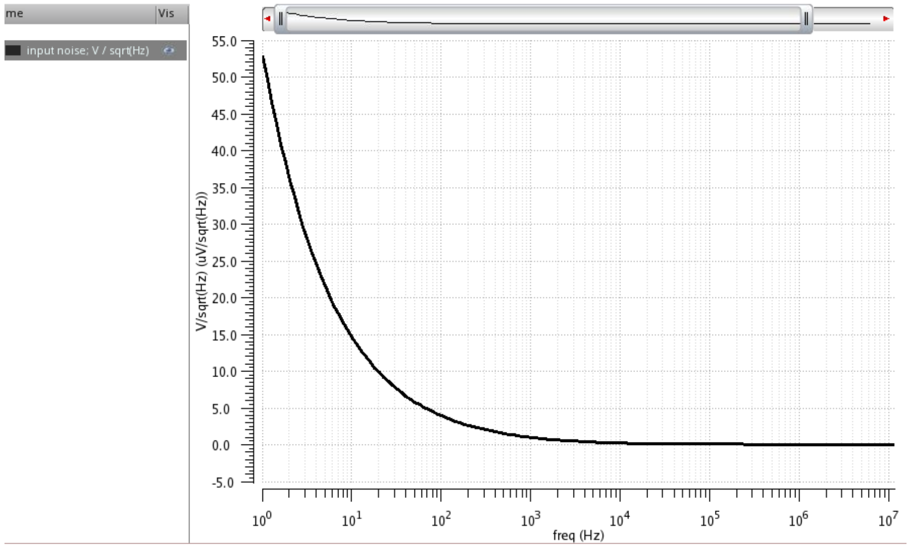

(a) Input-referred noise spectrum density

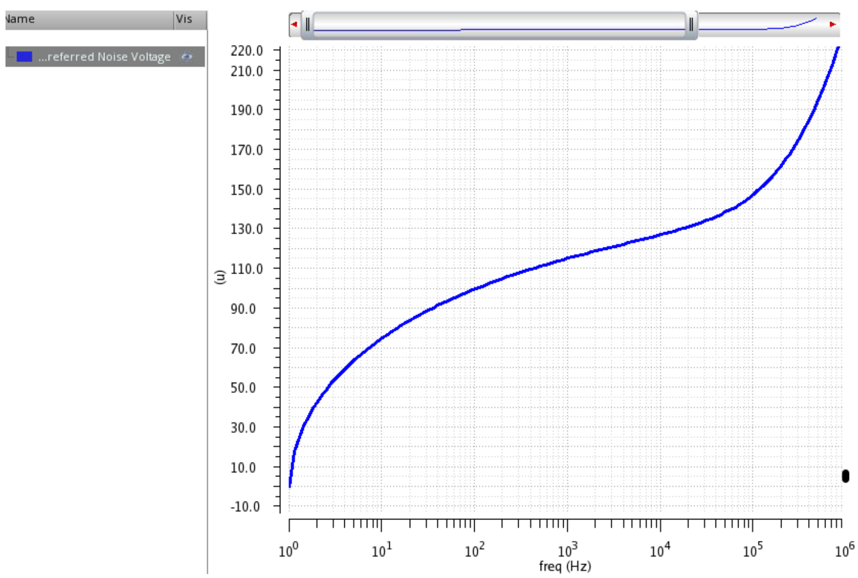

(b) Integrated input-referred noise voltage, integrating from 1Hz to 1MHz.

Fig. 4.17. Simulated input-referred noise spectrum density affecting the relaxation oscillator. Cadence Spectre™ is used, V_{pH} = 0.1V for the DC calculation.

In this work, a standard 0.13-μm CMOS technology is employed. The technology shows a temperature coefficient value $\frac{\partial V_T}{\partial T}$ of -0.78mV/°C.

Considering equation (4-15),

$$f = 1/T = I_C/(2C_C\Delta V) = (V_{pH} + V_{THP} + V_{OS})/(2R_S C_C \Delta V)$$

taking the derivative of the frequency with respect to the temperature, we can get the frequency versus temperature equation,

$$\frac{\partial f}{\partial T} = \frac{1}{2R_S C_C \Delta V}\frac{\partial V_{TH}}{\partial T} - \frac{(V_{pH} + V_{THP})}{2R_S^2 C_C \Delta V}\frac{\partial R_S}{\partial T} - \frac{(V_{pH} + V_{THP})}{2C_C^2 \Delta V}\frac{\partial \mathrm{C}_C}{\partial T} \tag{4-65}$$

For the process used in this work, $\frac{\partial V_{\mathrm{TH}}}{\partial T}$ = -0.78mV/°C; C_C is MIMCAP which has negative temperature coefficient with X_C denoted as the percentage of capacitance variation as well: $\frac{\partial C_C}{\partial T}$ = X_C *C_C/°C.

For the resistor part, in this process, it provides couple of types of poly resistors, which have different polarities of resistance coefficients. There are three main poly type resistors in this process. '*Oprpp*' type has temperature coefficient of +1.389E-4/°C, while '*Opppc*' type has -6.76E-5/°C which is about half of the absolute value of that of '*Oprpp*' type resistor. Type '*Oprrp*' has about -5.597E-4/°C, which has about 4x of temperature coefficient of '*Oprpp*" type. To make the resistor R_S, there will be two resistors used: '*Oprpp*' type resistor R_{S1} which contributes resistance of about 1/3**Rs* and '*Opppc*' type resistor R_{S2} which contributes about 2/3*R_S, in this way the total resistance is *Rs* but the temperature coefficient is almost 0. So, equation (4-65) becomes,

$$\frac{\partial f}{\partial T} = \frac{1}{2R_S C_1 \Delta V}\frac{\partial V_{TH}}{\partial T} - \frac{(V_{pH} + V_{THP})}{2C_1^2 \Delta V}\frac{\partial \mathrm{C}_1}{\partial T} \tag{4-66}$$

To make the temperature coefficient 0, we can let,

$$\frac{\partial f}{\partial T} = \frac{1}{2R_S C_1 \Delta V} \frac{\partial V_{TH}}{\partial T} - \frac{(V_{pH} + V_{THP})}{4C_1^2 \Delta V} \mathrm{X}_C \mathrm{C}_1 \tag{4-67}$$

Thus, the frequency variation percentage can be derived as,

$$\frac{\partial f / f}{\partial T} = \frac{1}{V_{pH} + V_{THP}} \frac{\partial V_{TH}}{\partial T} - \frac{1}{2} \mathrm{X}_C \tag{4-68}$$

In here, $V_{pH} + V_{THP}$ is not fixed value, but the other parameters are fixed. Using the process data for the equation above, X_C is -22%, we can get,

$$\frac{\partial f / f}{\partial T} = 1.1m - \frac{1}{V_{pH} + V_{THP}} * 0.78m \tag{4-69}$$

When V_{pH} is negative, $V_{pH} + V_{THP}$ can be very small, then the temperature coefficient can be considerate. If we use the middle value 0.5V then,

$$\frac{\partial f / f}{\partial T} = 1.1m - 2 * 0.78m = -0.46m \tag{4-70}$$

Using the interested temperature from -40°C to 125°C (ΔT = 165°C) for general commercial use, then the frequency variation is about -7.3%. If it is used for the environment detect such as water pollution detection, then the temperature usually is -20°C to 50°C, then the variation becomes -3.2%. If for biomedical use which usually has a temperature range of 20°C to 40°C, the frequency variation is only -0.84%.

4.3 Test Bench and Simulation

The structure reported in [16] is also designed in this chip for a more valuable comparison. So, the simulation is also performed together. Fig. 4.18 shows the test bench for the two sensor readout circuits. Three solar cells will provide a voltage around 1.5 ~ 1.8V for the LDO, the LDO will output 1.2V regulated DC output for PH readout circuit.

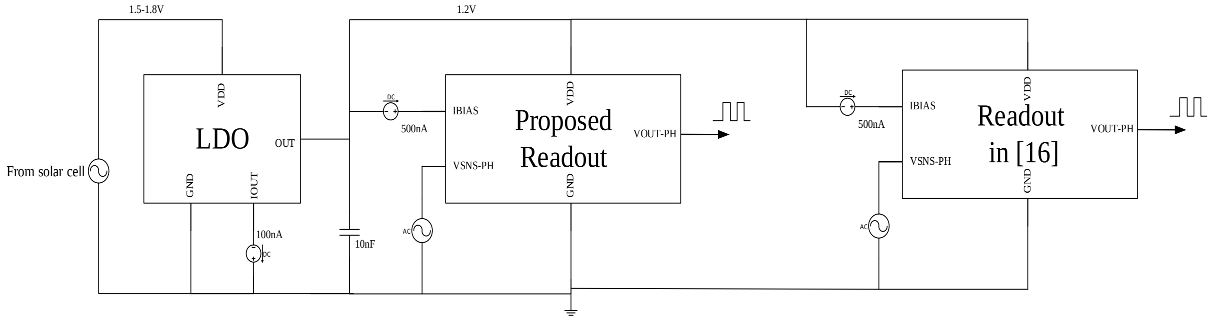

Fig. 4.18. The test bench setup.

Figure 4.19 shows the linearity of the pH readout circuit reported in [16]

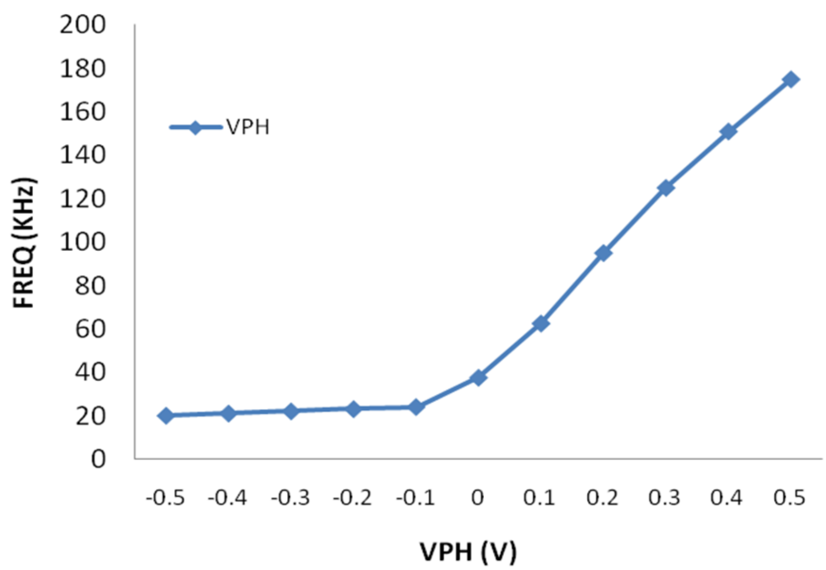

Fig. 4.19. Linearity of the old PH Readout circuits implemented in 0.13-µm process as a comparison.

Fig. 4.20 shows the output frequency versus the input voltage when sweeping input voltage from -0.5V to +0.5V. From the output frequency we can see the linearity is very well except at the low input voltage range.

Usually the test object does not need a full pH range from 0-14. Some range is very narrow and may need higher sensitivity which is also described as the output frequency gain in terms of V_{PH}. Take the human body pH detection for an example, from Table 3-1, if intracellular fluid is under detection, which is around 6.0-7.2. The pH sensor will output voltage ranging from -70mV to +14mV. From Fig. 4.19, with 1μA bias current or lower, the readout output frequency may not turn out large enough sensitivity.

To handle that issue, from equation (4-3), either charge capacitor C_C, sensing resistor Rs, or the two reference voltages difference ΔV can be reduced to improve the frequency – voltage gain.

$$f = 1/T = I_C/(2C_C\Delta V) = (V_{pH} + V_{THP})/(2R_S C_C \Delta V) \tag{4-3}$$

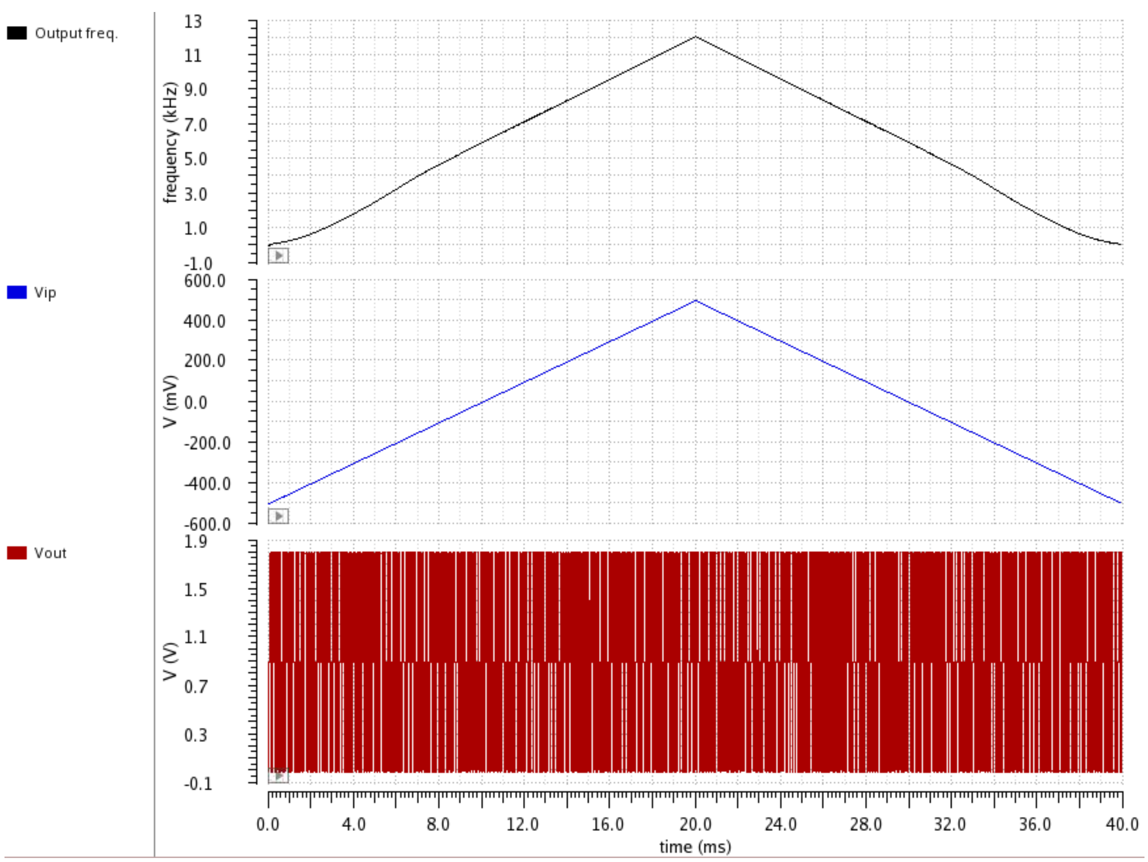

Fig. 4.20. The simulated output frequency sweeping V_{pH} values.

One of the advantage of this readout circuit is the three variables C_C, Rs, and ΔV are all linear factors which means frequency is changing linearly with the three parameters which can be derived from equation (4-15):

$$\frac{\partial f}{\partial VpH} = \frac{1}{2R_S C_C \Delta V} \tag{4-71}$$

If R_S is scaled down by half, then output frequency will be doubled. A simulation is performed to have single R_S, 2 R_S in parallel (total resistance R_S /2), 4 R_S in parallel (total resistance R_S /4), 8 R_S in parallel (total resistance R_S/8). The simulation result shown in Fig. 4.21 demonstrates promising scale of output frequency.

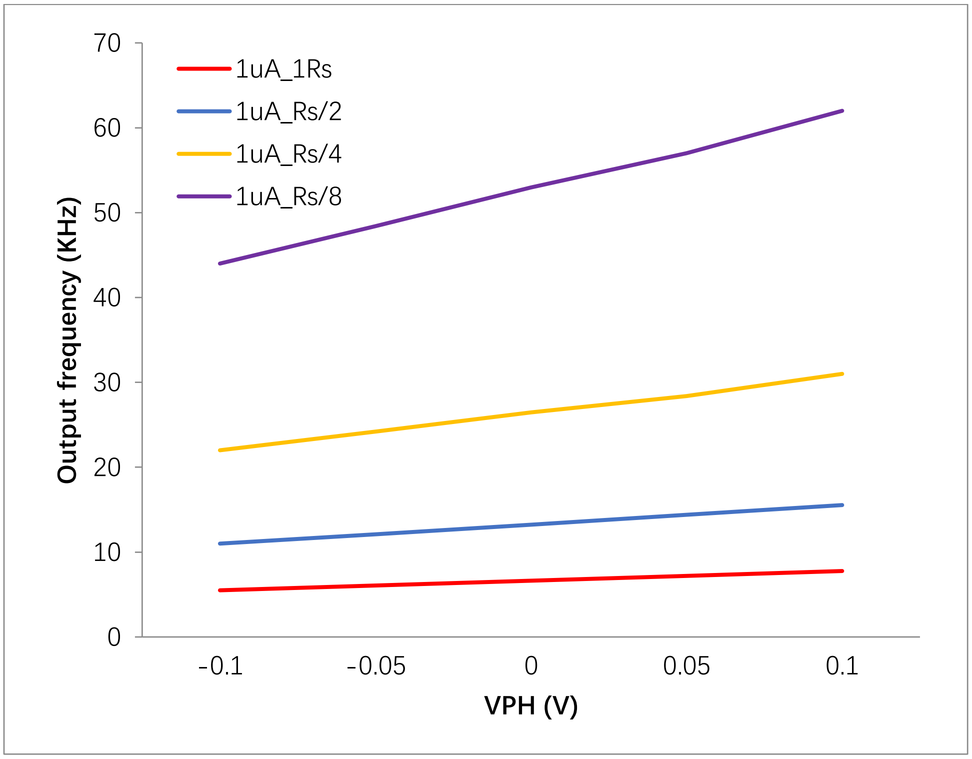

Fig. 4.21. The simulated output frequency under 1μA I_{bias} and different scaled resistance. The sensitivity increases from 11.35KHz/V to 90KHz/V. The current consumption increases as well, but it is scaled up. The simulated current for R_s, $R_s/2$, $R_s/4$, $R_s/8$ are 11.2 μA, 12.8 μA, 16.1 μA and 20.5 μA, respectively.

Table 4-2 shows the power consumption in each block.

Fig. 4.22 shows the LDO and bandgap layout used in the pH readout circuit.

TABLE 4-2 POWER CONSUMPTION IN BLOCKS

blocks	bandgap	LDO (core)	OTA	Others in Readouts	Total
Supply(V)	1.5-1.8	1.5-1.8	***1.25***	1.25	1.25
Current (μA)	2	***3***	2	4	11

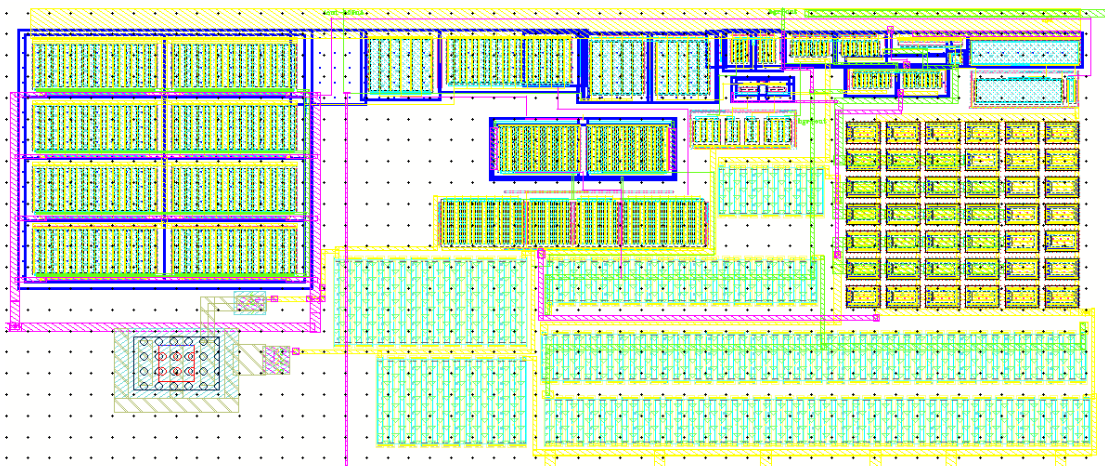

Fig. 4.22. Layout of the LDO and Bandgap Circuit (250μm x 100μm).

Fig. 4.23 shows the layout of the proposed pH sensor readout circuit, and Fig. 4.24 shows the conventional pH sensor readout circuit in [16] implemented in the same 0.13-μm process. The proposed readout circuit occupies a chip area of 160μm x 110μm, while the work in [16] implemented on same chip occupies 114μm x 86μm. The OTA in the proposed circuit is the main contributor of the area addition. LDO with bandgap occupies 250μm x 100μm. So total silicon size for this pH measurement system including proposed readout circuit and LDO are 0.043 mm^2.

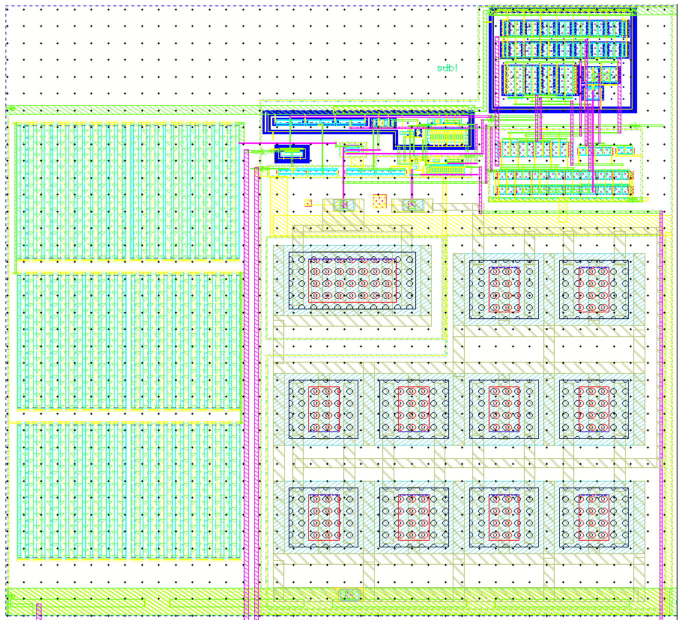

Fig. 4.23. Layout of the proposed pH Readout Circuit (200µm x 140µm).

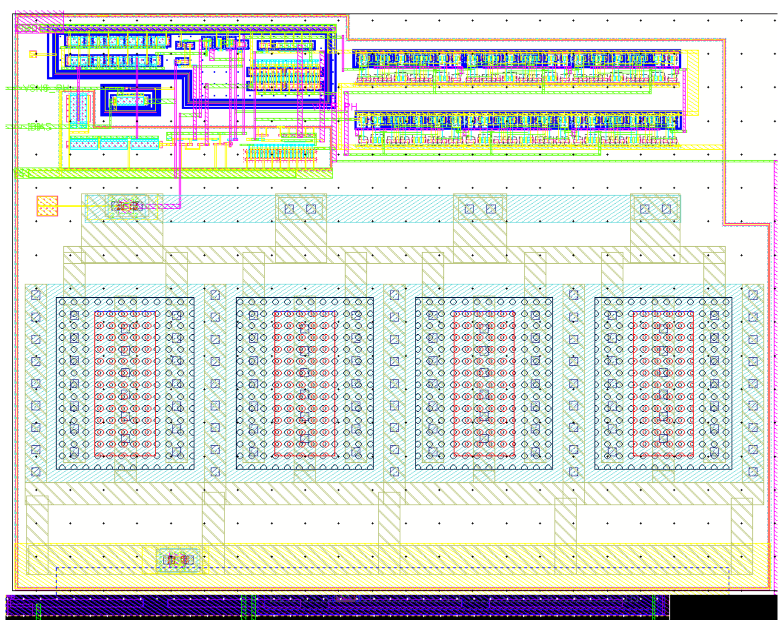

Fig. 4.24. Layout of the old pH Readout Circuit (114 µm x 86µm).

Chapter 5 Chip Test and Measurement

Both the proposed circuit and the conventional one in [16] are fabricated in the same chip. Fig. 5.1 shows the die photo for this chip. Fig. 5.2 shows several typical output waveforms under different input pH sensor voltages. Note that different I_{bias} can give different output frequency. This feature can be used to trim the output frequency at targeted pH range.

5.1 Chip Test and Measurement

Table 5-1 shows both the simulation and test results of the output frequency versus input voltage. The simulation result shows very good linearity almost all over the input V_{PH} range, while the test results matches the simulation ones very well in most of the input range. The frequency variation error is defined to be the difference between test and simulation results divided by the simulation results, where simulation results are considered as reference. It is clearly shown the calibrated results has better linearity all over the interested input range, especially for the small V_{PH} values.

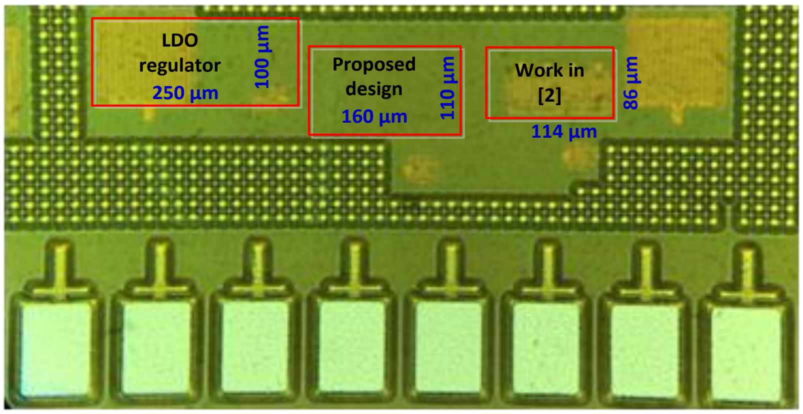

Fig. 5.1. Chip photo with bond pads.

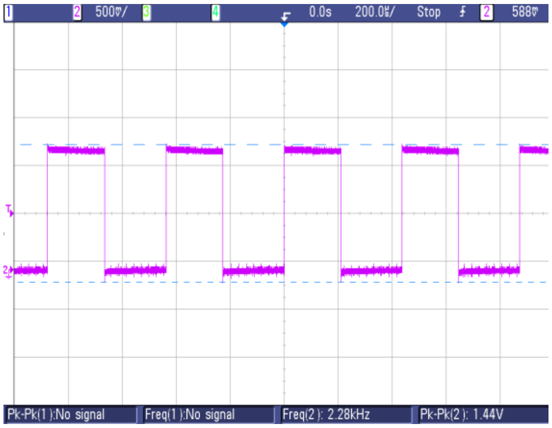

(a)

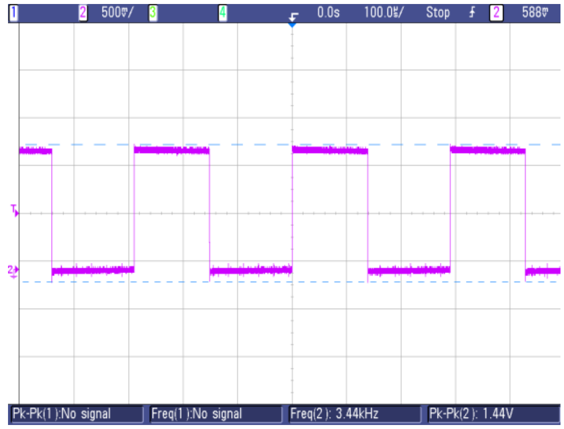

(b)

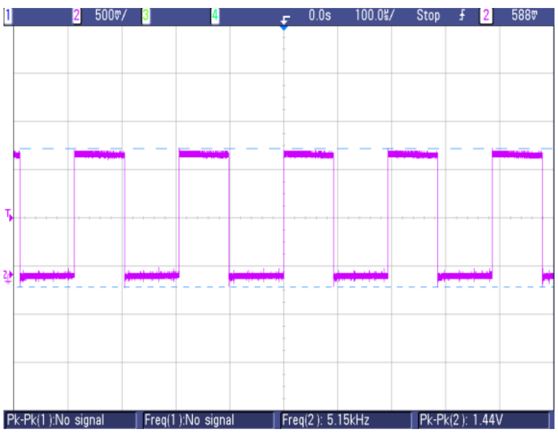

(c)

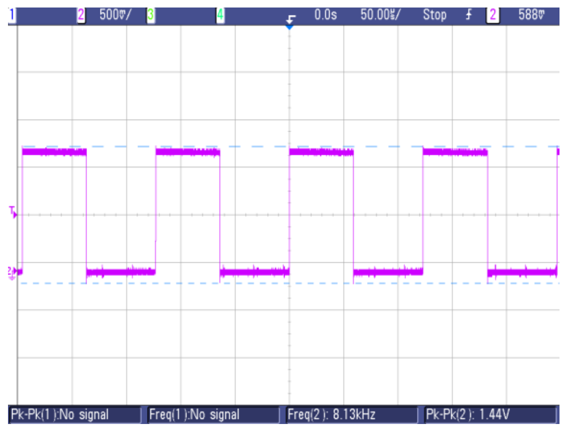

(d)

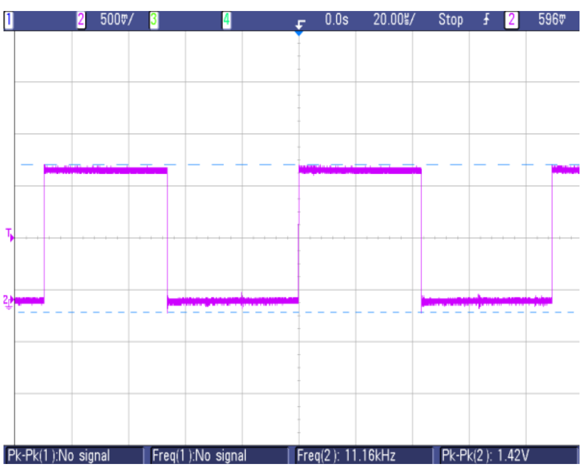

(e)

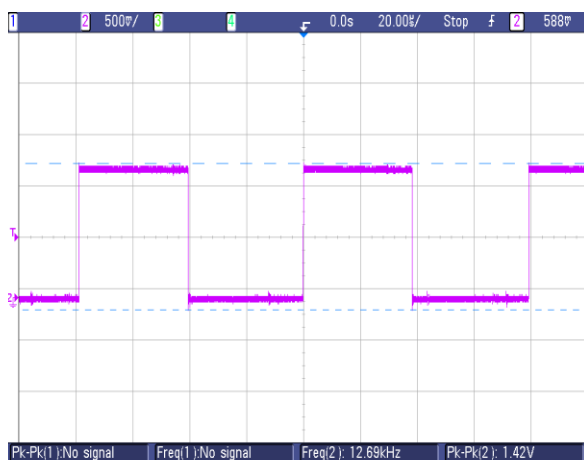

(f)

Fig. 5.2. The output square wave of proposed sensor readout circuits under different V_{pH} voltages. (a) V_{pH} = -400mV, (b) V_{pH} = -300mV, (c) V_{pH} = -50mV, (d) V_{pH} = 150mV, (e) V_{pH} =400mV, (f) V_{pH} = 530mV.

TABLE 5-1 ERRORS IN THE OUTPUT AT DIFFERENT PH VALUES

pH voltage (V)	**pH value**	**Simulated Freq. (KHz)**	**Measured Freq. (KHz)**	**Output freq. error (%)**	**Error after cal.**
-0.5	0	1	1.686	68	9.5
-0.36	2	2.64	2.66	3	3.5
-0.21	4	4.29	4.26	0.45	1
-0.07	7	6.6	6.62	0	0.2
0.21	10	8.95	9.02	1.1	1.5
0.36	12	10.56	10.7	1.4	2
0.5	14	12.1	12.3	1.65	3

The prototype of the proposed pH sensor readout circuit is designed and fabricated using a standard 0.13-µm CMOS process. To make a better comparison, the readout circuit in [2] is also redesigned in the same chip.

Fig. 5.3 shows the test results of the output frequency versus the input pH sensor voltage for both the circuits. The simulation result of the proposed circuit is also presented in the same figure. For the proposed circuit, the output frequency changes linearly with the input voltage which represents the pH values, while the conventional circuit in [16] shows obvious parabolic feature for the first part from -0.5V to 0V and then saturates after 0V due to the limited headroom of the node V_1.

Five chip prototypes are tested to verify the output frequency consistency under different process variations. Table 5-2 shows the measured frequency with calculated mean value and standard deviation based on the five chips. The worst standard deviation is about 0.095 KHz when V_{pH} is

-0.5V which gives 5% of output frequency error at the worst case. The last row of output error is defined as standard deviation divided by mean value. As V_{pH} increases, the standard deviation remains almost constant which means the frequency error decreases as is shown in the table.

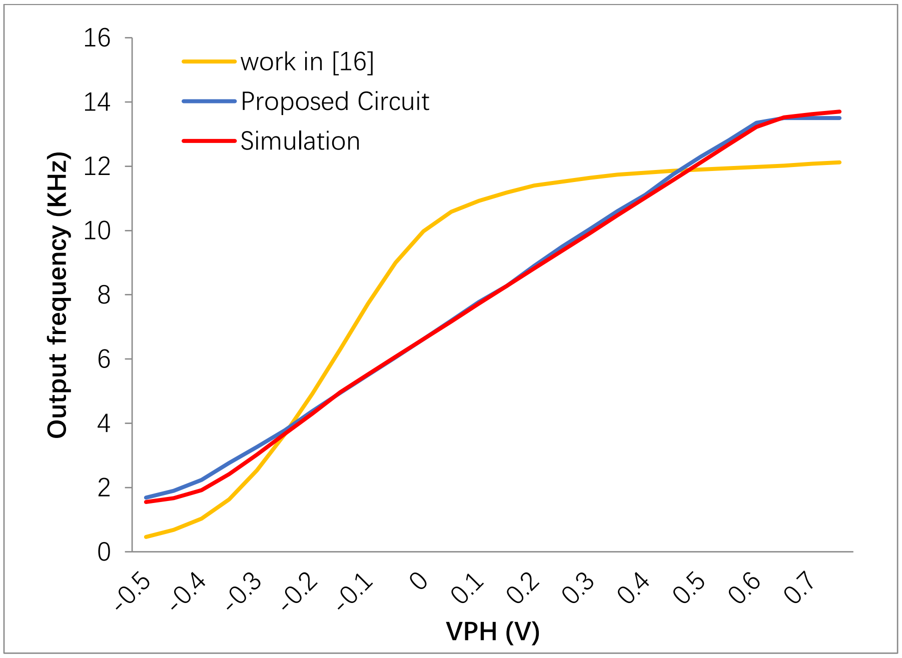

Fig. 5.3. Test results of linearity of proposed sensor readout circuits compared with the one in [2], and the simulation result.

Fig. 5.4 shows the output frequencies for 200nA and 1μA I_{bias} current. As is expected, lower bias current can achieve lower frequencies. The lower bias current, the easier to get frequency saturated at small V_{PH}, but the better linearity can be achieved at large V_{PH} value. So, it is very convenient to create different measurement options for different input pH range. For example, for acid environment especially acid environment, pH value is usually small and less than 7, lower I_{bias} value can be chosen to have better linearity within interested input pH range. Higher bias current can be employed for alkaline applications.

TABLE 5-2 OUTPUT FREQUENCIES TEST OVER FIVE CHIPS.

Chip #	**f_{out} (KHz) -0.5VpH**	**f_{out} (KHz) -0.21VpH**	**f_{out} (KHz) -0.07VpH**	**f_{out} (KHz) 0.21VpH**	**f_{out} (KHz) 0.5VpH**
1	1.686	4.29	6.6	8.95	12.1
2	1.69	4.29	6.62	8.95	12.1
3	1.9	4.35	6.72	9.06	12.2
4	1.677	4.19	6.5	8.84	12
5	1.7	4.39	6.7	9.1	12.2
Mean	1.731	4.302	6.628	8.97	12.12
Standard deviation	0.095	0.076	0.087	0.09	0.083
Output error	5.5%	1.76%	1.32%	1%	0.7%

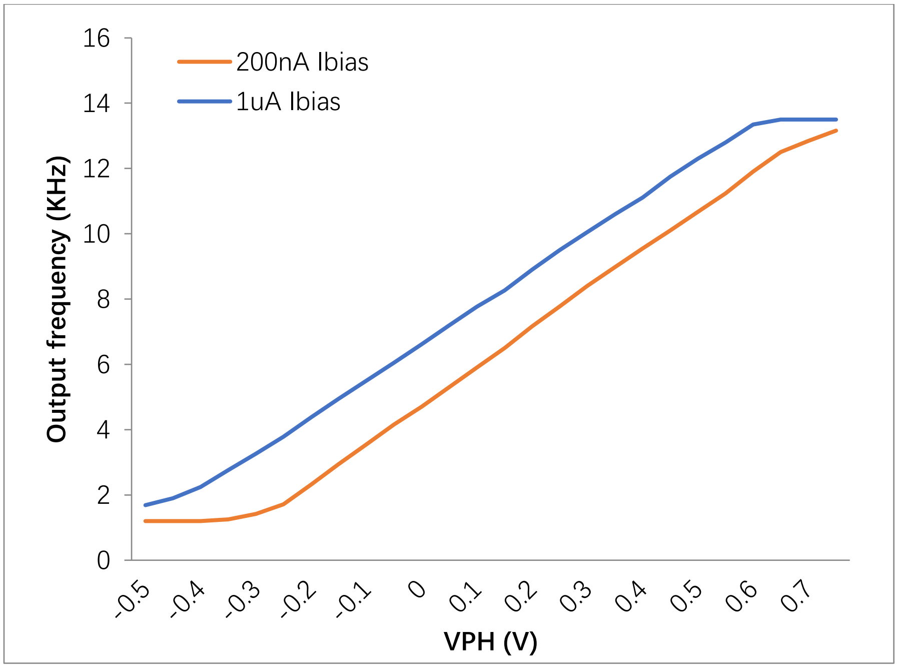

Fig. 5.4. Output frequency comparison with 200nA and 1μA I_{bias} current.

Fig. 5.5 shows the test result for the LDO, including the line regulation (a) and load regulation response (b). From the test result it can be concluded the LDO output voltage can be held within 100mV under line regulation and less than 20mV fluctuation under load regulation. The response time is around 15 µs which is fast enough for the biomedical application.

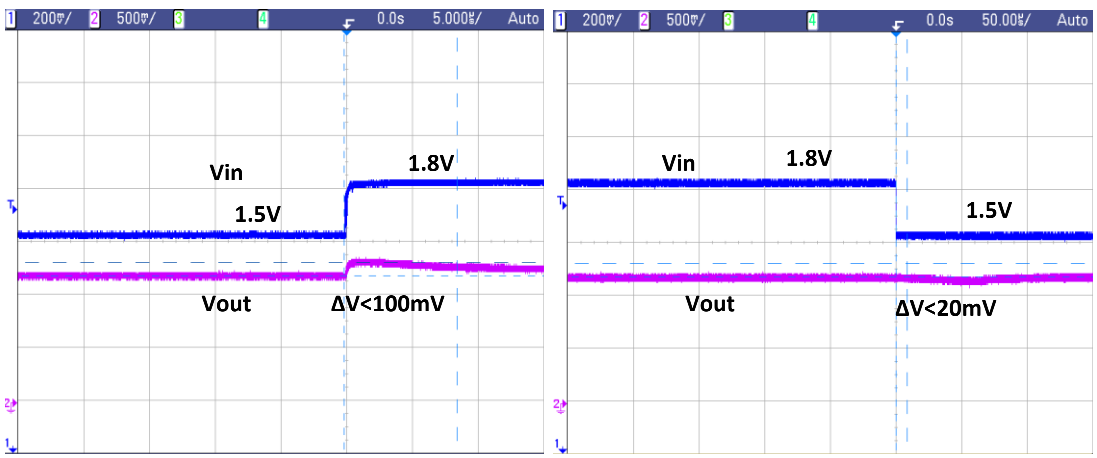

(a) Line regulation response, Vin is set to be a waveform ranging from 1.5V to 1.8V with 10ns rise/fall time, load current is 1mA.

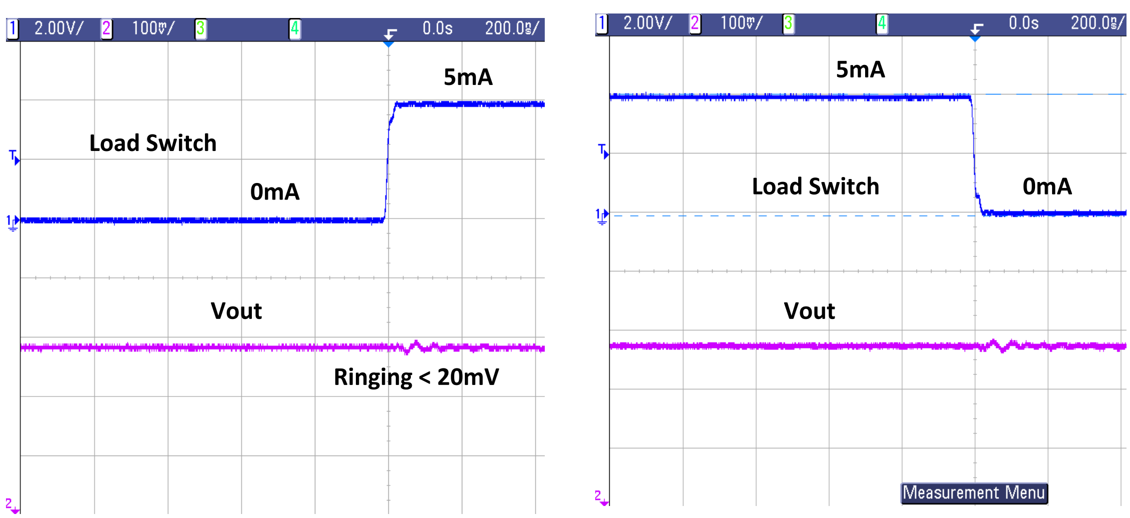

(b) Load regulation response, load switch turns on or off a resistor load. Turn on: 5mA, turn off: 0mA. Vin is set 1.5V.

Fig. 5.5. Test results of the LDO, with (a) line regulation (b) load regulation.

5.2 In-Vitro Test

In-vitro test is essential for the pH sensor measurement system. Limited by the chemical materials and professional tools, a simple measurement kit is purchased from online shop for the in-vitro test. Fig. 5.6 shows the test setup for the in-vitro test.

First, to test it, a pH solution is generated using acid and alkaline chemicals as pH substances. Three chemicals were employed:

1. Potassium hydrogen phthalate (pH = 4.00 at 25^{o}C);
2. Mixed phosphate (pH = 6.86 at 25^{o}C);
3. Sodium tetraborate (pH = 9.18 at 25^{o}C);

Each chemical can be used for 25s0ml solution. So, in this experiment, we will mix the solutions to generate different pH values from 4~9.18 with a limited range.

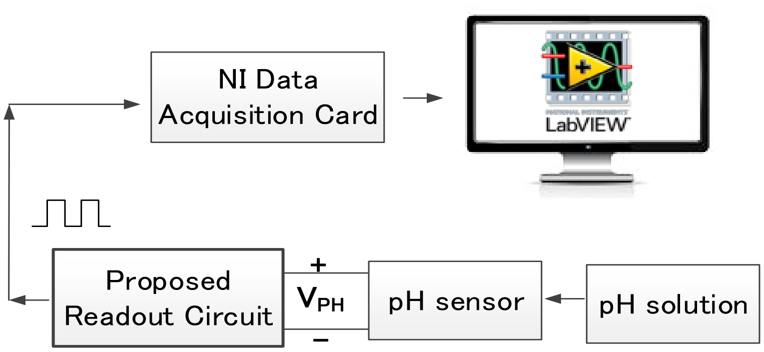

Fig. 5.6. Block diagram of the measurement and calibration setup for the readout circuit. The CMOS microchip with the pH sensor generates square wave signal based on the pH level and then send to a microprocessor which counts the frequency and send the data to a computer via a Bluetooth transceiver. Eventually the data will be displayed and processed in the LabView from the computer.

Fig. 5.7 shows the electrochemical sensor alongside a 22-gauge needle for size comparison.

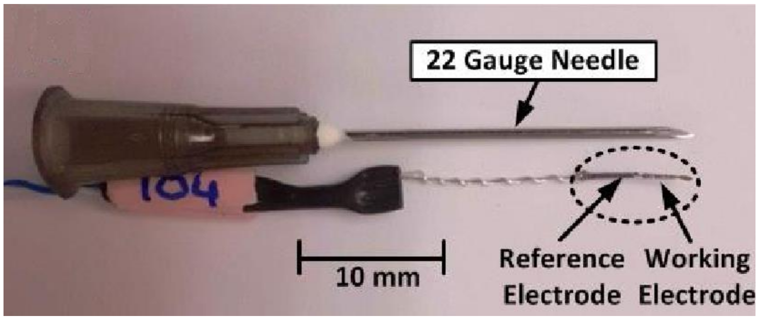

Fig. 5.7. Photograph of the fabricated electrochemical sensor alongside a 22-gauge needle for size comparison.

The calibration and test procedures are as follows:

1. prepare three different solutions using the three chemicals mentioned above, these pH values are fixed from the manufacturer. To confirm the pH values, a commercial pH meter is employed as shown in Fig. 5.8. The model name is HANNA™ HI98128.

Fig. 5.8. A commercial pH meter is employed to confirm the pH values in the solutions.

2. Test the three chemicals separately to get the PH_OUT voltage.

3. Then using another container to mix the chemicals to increase the pH values by adding more alkaline chemicals. Connect all the components together with the test chip in this work, shown in Fig. 5.9.

Table 5-3 shows the pH values and PH_OUT voltage and output frequencies under different pH values. Due to the limited chemicals, a pH level from 4-9.18 has been tested which can cover a wide range of applications.

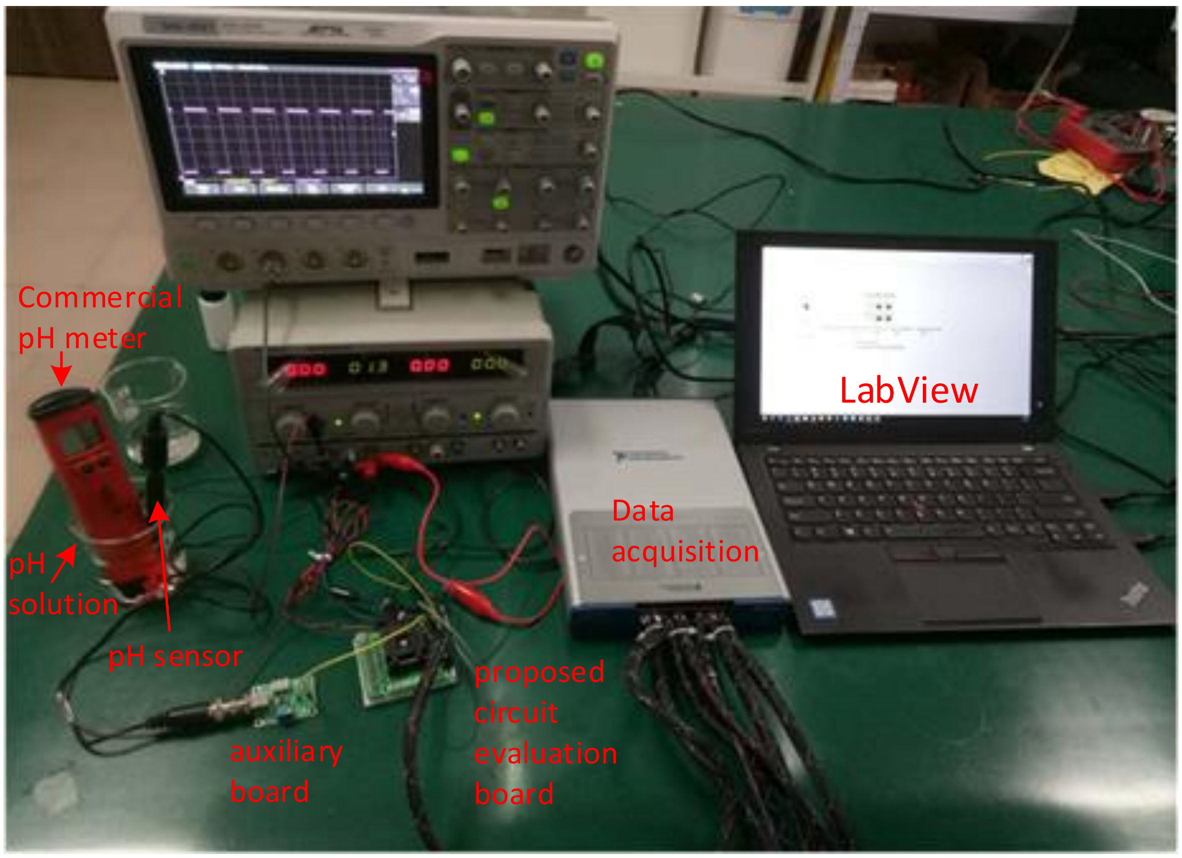

Fig. 5.9. In-vitro test setup for the pH measurement system in this work, including solution, pH sensor/electrode, and an auxiliary board. Auxiliary board provides a proper socket and RC filter. A National Instruments™ acquisition system is employed to transfer data from the proposed circuit to computer.

Figure 5.10 plots the result from Table 5-3 to give a more intuitive comparison. From the figure, it can be concluded that the pH sensor itself has a very linear output voltage versus input pH values within 4-9.18 pH range. And this readout circuit can also demonstrate a great linearity all over the range, which is verified from the chip test and measurement session. However, this in-vitro test still can demonstrate a stable operation of the readout system with the pH sensor in a real pH solution.

TABLE 5-3 OUTPUT FREQUENCIES AND PH_OUT VOLTAGE UNDER DIFFERENT PH VALUES

pH	pH_OUT (V)	Output Frequency (KHz)
4	0.464	12
4.68	0.415	11.4
5.01	0.393	11
5.57	0.352	10.6
6.86	0.26	9.5
7.53	0.21	9
8.46	0.145	8.17
9.18	0.094	7.7

5.3 Conclusion

The pH sensor measurement system in this paper is proposed and designed showing high linearity, wide detection range and low-power dissipation and is realized in a standard 0.13-μm CMOS technology. The system is analyzed, and measured, and the measurement shows very good match with the simulation. The calibration can help the output frequency tuned with good linearity within the interested pH output range -0.5V ~ +0.5V. A customized wide range pH sensor application figure-of-merit (FoM), is defined as below:

$$FoM = \frac{InputRange * sensitivity}{Power * CircuitSize} \tag{5-1}$$

The unit is $\frac{kHz / V}{\mu W * mm^2}$.

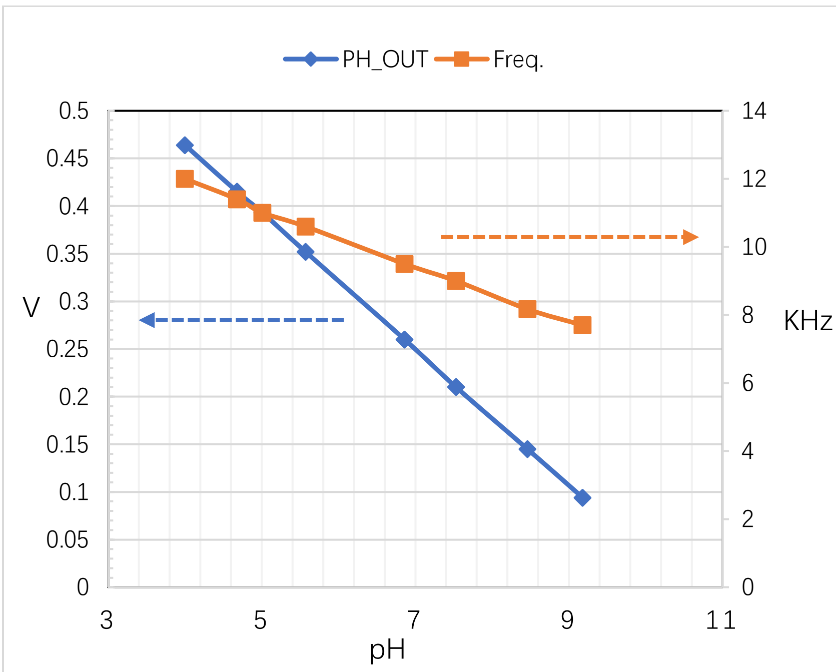

Fig. 5.10. pH sensor output voltage measurement system ouput frequency versus input pH values.

Then we can summarize the performance of this proposed measurement system with the state-of-arts, shown in Table 5-4. Here sensitivity is defined as the change in the output frequency over the change in the pH level that can be effectively detected. The table compares from power, process, supply, pH levels can be effectively detected, whether including integrated power conditioning unit (voltage regulator), silicon size, sensitivity, and FoM.

Simple comparison with these values may not reflect the real importance of this work. For example, to cover -0.5V to +0.5V, it is getting more than 2X harder to cover 0 ~ +0.5V. The effort in [43] to reduce noise with averaging algorithm is similar with the calibration method in this work.

It can be seen from the test results that the proposed design demonstrates a much better linearity with very little power and dies size compromise. In addition, due to the high linearity, the proposed circuit can effectively cover a wide range of pH sensor voltage which can cover from -7 to 7 real pH values with commercial pH sensors calibrated with -0.5V to +0.5V output.

TABLE 5-4 PERFORMANCE COMPARISON OF THE PROPOSED WORK WITH PREVIOUS LITERATURE

Work	**Power** (μW)**	**Process (μm)**	**Supply (V)**	**pH*****	**voltage reg.?**	**Circuit Size (mm^2)**	**Sensitivity (kHz/pH)**	**FoM**
[16]	120	0.35	3.5	0 ~7	No	0.045	121	2.2
[16] *	50	0.13	1.25	0 ~7	No	0.001	1.285	25.7
[43]	6	0.35	1.2	5-7	No	0.109	6~8	12
This	14	0.13	1.25	0~14	Yes	0.0017	0.86	**38**

**to be fair, only include the readout core, not including power conditioning unit.*

**Effectively pH levels can be detected with good linearity.*

**** Circuit in [16] implemented on the same 0.13-μm process chip for comparison. Sensitivity is calculated from -0.5V to 0V pH sensor voltage.*

Table 5-5 shows specification comparison from some most popular commercial pH meters. From the table this work can implement comparable performance with using lower supply voltages. The supply current is unknown from the commercial products, but this work can achieve very low current not including post-processing units or display parts. The temperature range is also wider, which is mainly limited by the sensor itself, because the measurement part can operate with -40~125ºC.

TABLE 5-5 SPECIFICATION COMPARISON OF THE PROPOSED WORK WITH COMMERCIAL PH METERS

Manufacturer	**Model**	**pH range**	**Supply (V)**	**resolution**	**Temp. range**	**Calibration**
Jellas™	JLPH01	0~14	4.5	0.1	0~50ºC	automatic
Hach™	9531000	0~14	6	0.1	0~50ºC	automatic
Apera™	AI209	0~14	6	0.1	0~50ºC	automatic
Hanna™	HI98128	-2~16	1.5	0.01	-5~50ºC	automatic
This	NA	0~14	**1.25**	0.01	**-20~65ºC***	manual

* *From simulation results.*

Chapter 6 Conclusion and Future Work

6.1 Original Contributions

This work went through multiple phases identifying the project, researching the literature and prior arts, identified the problem, confirmed the value of the problem, and finally found the practical approach for the problem. With the key milestones achieved, it is expected that the design will be finalized and followed by test and characterization. The planning of the remaining part of this project is listed below.

1. Proposed and designed a mass production ready multiple purposes (biometrical and environmental) pH sensor readout circuit with low-power, miniaturized size in standard CMOS technology, and high linearity.

2. Maximized the input pH sense voltage range to cover a wide range of pH sensor applications.

3. Proposed a simple and feasible method to calibrate the output frequency to overcome the variations from process.

4. Developed the basic mathematical model to validate the linearity and frequency calibration.

5. Developed the power management unit for the pH sensor and readout circuit, to make the pH measurement system a complete one suitable for a low-power application.

6.2 Future Work

A list of items expected to be delivered at the end of this work is discussed below:

1. Do more practice of in-vivo test including biomedical, real environmental test, to test the output frequency response under real-world noise, fluctuation and so on;

2. Create different options for different input ranges, like acid, alkaline etc., to make it more convenient to use.

3. May make one option dedicated for biomedical application since the pH values vary very small, then the output frequency can be designed to have better sensitivity.

4. Build an auto-calibration system for the output frequency variation;

5. Optimize the circuits to minimize the temperature coefficient.

References

[1] "The History of the Integrated Circuit". *Nobelprize.org*, Apr. 2012.

[2] B.K. Jain, "Digital Electronics - A Modern Approach", *Global Vision Publishing House*, May 2017.

[3] Michael J. Flynn, Wayne Luk, "*Computer System Design: System-on-Chip*", Wiley, ISBN: 978-0-470-64336-5, Oct. 2011.

[4] R. Ghodssi and P. Lin, "*MEMS Materials and Processes Handbook*". Berlin: Springer. ISBN 978-0-387-47316-1, 2011.

[5] Pier Andrea Serra, "*Advances in Bioengineering*", ISBN 978-953-51-2141-1, July 2015.

[6] Ping Wang and Qingjun Liu, "*Biomedical Sensors and Measurement*", ISBN 978-3-642-19525-9, 2011.

[7] Gerard Meijer, "*Smart Sensor Systems*", ISBN: 978-0-470-86691-7, Oct. 2008.

[8] Andrea De Marcellis and Giuseppe Ferri, "*Analog Circuits and Systems for Voltage-Mode and Current-Mode Sensor Interfacing Applications*", ISBN 978-90-481-9827-6, Spring, 2011.

[9] Robert Bogue, "Sensors for Extreme Environments", *Sensor Review*, vol. 32, issue: 4, pp.267-272, 2012.

[10] S. K. Islam and M. R. Haider, "*Sensors and Low Power Signal Processing*", ISBN 978-0-387-79392-4, Springer, 2010.

[11] T. Prodromakis, Y. Liu and C. Toumazou, "Low- Cost Implementations of pH Monitoring Platforms", *IEEE Sensors Journal*, pp. 1082 - 1084, 2011.

[12] Hamid Basaeri, David Christensen, Shad Roundy, Yuechuan Yu, Tram Nguyen, Prashant Tathireddy and Darrin J. Young, "Ultrasonically powered hydrogel-based wireless implantable glucose sensor", *IEEE Sensors Journal*, 2016, pp. 1 – 3.

[13] Saumya Joshi; Vijay Deep Bhatt; Hao Wu; Markus Becherer; Paolo Lugli, "Flexible Lactate and Glucose Sensors Using Electrolyte-Gated Carbon Nanotube Field Effect Transistor for Non-Invasive Real-Time Monitoring", *IEEE Sensors Journal*, vol. 17, Issue 14, 2017, pp. 4315 – 4321.

[14] Sara S. Ghoreishizadeh, Camilla Baj-Rossi; Andrea Cavallini, Sandro Carrara, Giovanni De Micheli, "An Integrated Control and Readout Circuit for Implantable Multi-Target Electrochemical Biosensing", *IEEE Transactions on Biomedical Circuits and Systems*, vol. 8, Issue 6, pp. 891 - 898, 2014.

[15] Jing Liu, Yuan-Ting Zhang, Xiao-Rong Ding, Wen-Xuan Dai and Ni Zhao, "A Preliminary Study on Multi-Wavelength PPG Based Pulse Transit Time Detection for Cuffless Blood Pressure Measurement", *38th Annual International Conference of the IEEE Engineering in Medicine and Biology Society (EMBC)*, pp. 615 - 618, 2016.

[16] R.A. Croce, S. Vaddiraju, A. Legassey, K. Zhu, S.K. Islam, F. Papadimitrakopoulos and F.C. Jain, "A Highly Miniaturized Low-Power CMOS Based pH Monitoring Platform", *IEEE Sensors Journal*, 2015, 15 (2), pp. 895-901.

[17] Song Yuan, Hanfeng Wang and Syed K. Islam, "A Monolithic Low-Power Highly Linear pH Measurement System for Medical Application with Power Conditioning System", *IEEE International symposium on Medical Measurements and Applications (MeMeA)*, 2017.

[18] Kai Zhu, Syed K. Islam, Mohammad R. Haider, Melika Roknsharifi, Jeremy Holleman, "A Simple Oscillator-Based Data Generation and FSK Telemetry Unit for Low-Power Biomedical Implant System", *Analog Integrated Circuits and Signal Processing*, vol. 72, Issue 2, Aug. 2012, pp 383-393.

[19] P. Mohseni, K. Najafi, S. J. Eliades, and X. Wang, “Wireless Multichannel Biopotential Recording Using an Iintegrated FM Telemetry Circuit,” *IEEE Transactions on Neural Systems and Rehabilitation Engineering*, Sep. 2005, vol. 13, no. 3, pp. 263-271.

[20] R. R. Harrison, P. T. Watkins, R. J. Kier, R. O. Lovejoy, D. J. Black, B. Greger, and F. Solzbacher, “A Low- Power Integrated Circuit for a Wireless 100-Electrode Neural Recording System,” *IEEE Journal of Solid-State Circuits*, Jan. 2007, vol. 42, no. 1, pp. 123-133.

[21] F.C. Jain, F. Papadimitrakopoulos, R.A. Croce, P. Gogna, S.K. Islam, L. Zuo, and K. Zhu, “Circuit Architecture and System for Implantable Multi-Function and Multi-analyte Biosensing Device”, *US Patent #US20140072308 A1*, published Mar. 2014.

[22] Leonarda Carnimeo, Annamaria Roberta Altomare, and Rosamaria Nitti, “Monitoring of Retinal Vessels for Diabetic Patients in Home Care Assistance”, *IEEE International Symposium on Medical Measurements and Applications (MeMeA)*, 2016.

[23] Luigi Battista and Gianvito Summa, “Preliminary Evaluation of a Wireless Remote Monitoring System for Home Mechanical Ventilation”, *IEEE International Symposium on Medical Measurements and Applications (MeMeA)*, 2016.

[24] Sharmistha Bhadra, Warren Blunt, Chris Dynowski, Michael McDonald, Douglas J. Thomson, Michael S. Freund, Nazim Cicek, and Greg E. Bridges, “Fluid Embeddable Coupled Coil Sensor for Wireless pH Monitoring in a Bioreactor”, *IEEE Transactions on Instrumentation and Measurement*, vol. 63, no. 5, May 2014, pp. 1337-1346.

[25] Richard J. Wagner, Harold C. Mattraw, George F. Ritz, and Brett A. Smith, “Guidelines and Standard Procedures for Continuous Water-Quality Monitors: Site Selection, Field

Operation, Calibration, Record Computation, and Reporting", *U.S. Geological Survey*, 2006.

[26] Soil Testing & Investigation, *http://www.ppsthane.com/soil-testing-investigation*

[27] Yu Jiang, Xu Liu, Tran Chien Dang, Mei Yan, Hao Yu, Jui-Cheng Huang, Cheng-Hsiang Hsieh, Tung-Tsun Chen, "A 512×576 65-nm CMOS ISFET Sensor for Food Safety Screening with 123.8 mV/pH Sensitivity and 0.01 pH Resolution", *IEEE Symposium on VLSI Technology Digest of Technical Papers*, 2016.

[28] Department of Ecology, State of WA, *http://www.ecy.wa.gov/programs/eap/index.html.*

[29] M.C. Frost, M.E. Meyerhoff, M. E.: "Implantable Chemical Sensors for Real-Time Clinical Monitoring: Progress and Challenges", Current Opinion in Chemical Biology, 2002, 6, (5), pp. 633-641.

[30] Gerry K. Schwalfenberg, "The Alkaline Diet: Is There Evidence That an Alkaline pH Diet Benefits Health?" *Journal of Environmental Public Health*, Issue 2012.

[31] B. J. Yee, J. Cheung, P. Phipps, D. Banerjee, A.J. Piper, and R. R. Grinstein, "Treatment of obesity hypoventilation syndrome and serum leptin", *Respiration*, vol. 73, no. 2, pp. 209-212, 2006.

[32] Z.H. Fu, C.P. Joshi and A.H. Titus, "CMOS-Based Colour-Change pH Measurement System", *Electronics Letters*, 2009, 45 (22), pp.1138 – 1140.

[33] F.J.F. Martin, J.C.C. Rodriguez, J.C.A. Anton, J.C.V. Perez ; I. Sanchez-Barragan, J.M. Costa-Fernandez and A. Sanz-Medel, "Design of a Low-Cost Optical Instrument for pH Fluorescence Measurements", *IEEE Transactions on Instrumentation and Measurement*, Volume: 55, Issue: 4, Aug. 2006, pp. 1215 – 1221.

[34] D.R. Munoz, S.C.s Berga, D.F.N. Diaz, R. Garcia-Gil and A.E.N. Anton, "Transconductance Converters Based on Current Mirrors Applied to pH Measurement Using ISFET Sensors," *IEEE Transactions on Instrumentation and Measurement*, vol. 58, issue 2, Feb. 2009, pp. 434 - 440.

[35] Erick Garcia-Cordero, Hoël Guerin, Amira Muhech, Francesco Bellando, and Adrian M. Ionescu, "Heterogeneous Integration of Low Power pH FinFET sensors with Passive Capillary Microfluidics and miniaturized Ag/AgCl quasi-Reference Electrode", *IEEE 46th European Solid-State Device Research Conference (ESSDERC)*, Sep. 2016, pp. 452-455.

[36] S. Rigante , P. Livi , M. Wipf , K. Bedner , D. Bouvet , A. Bazigos , A. Rusu , A. Hierlemann and A. M. Ionescu, "Low Power FinFET pH-Sensor With High-Sensitivity Voltage Readout", Proceedings of the European Solid-State Device Research Conference (ESSDERC), Sep. 2013, pp.350-353.

[37] Xiwei Huang, Hao Yu, Xu Liu, Yu Jiang, Mei Yan, and Dongping Wu, "A Dual-Mode Large-Arrayed CMOS ISFET Sensor for Accurate and High-Throughput pH Sensing in Biomedical Diagnosis", *IEEE Transactions on Biomedical Engineering*, vol. 62, no. 9, Sep. 2015, pp. 2224 – 2233.

[38] M.S. Veeramani, P. Shyam, N.P. Ratchagar, A. Chadha, E. Bhattacharya, and S. Pavan, S, "A Miniaturized pH Sensor with an Embedded Counter Electrode and a Readout Circuit," *IEEE Sensors Journal*, 2013, 13, (5), pp. 1941-1948.

[39] Cheng-Hsin Chuang, Hsun-Pei Wu, Cheng-Ho Chen, Peng-Rong Wu, "Flexible pH Sensor with Polyaniline Layer Based on Impedance Measurement", *2011 Fifth International Conference on Sensing Technology*, pp 211 – 216.

[40] B. Lakard, Guillaume Herlem, Sophie Lakard, René Guyetant and Bernard, Fahys., “Potentiometric pH Sensors Based on Electrodeposited Polymers”, *Polymer*, vol. 46, pp. 12233-12239, 2005.

[41] P. Bergveld, “Development of an Ion-Sensitive Solid-State Device for Neurophysiological Measurements”, *IEEE Transactions on Biomedical Engineering*, vol. 17, Jan. 1970, pp. 70–71.

[42] K.B. Parizi, A.J. Yeh, ASY Poon, H-S Wong, “Exceeding Nernst limit (59mV/pH): CMOS-based pH Sensor for Autonomous Applications”, *IEEE International Electron Devices Meeting (IEDM)*, 2012.

[43] Matthew Douthwaite, Ermis Koutsos, David C. Yates, Paul D. Mitcheson, and Pantelis Georgiou, “A Thermally Powered ISFET Array for On-Body pH Measurement”, *IEEE Transactions on Biomedical Circuits and Systems*, vol. PP, Issue: 99, Aug. 2017.

[44] Yuanqi Hu, and Pantelis Georgiou, “A Robust ISFET pH-Measuring Front-End for Chemical Reaction Monitoring”, *IEEE Transactions on Biomedical Circuits and Systems*, vol. 8, no. 2, April 2014.

[45] Mst Shamim Ara Shawkat and Nicole McFarlane, “A Single-Chip ISFET based pH Sensor”, *IEEE Sensors* Journal, 2016.

[46] Guenole Lallement, Nicolas Moser, and Pantelis Georgiou, “Bio-inspired pH sensing using Ion Sensitive Field Effect Transistors”, *IEEE International Symposium on Circuits and Systems*, 2016.

[47] P.R. Gray and R.G. Meyer, *Analysis and Design of Analog Integrated Circuits*, New York; John Wiley & Sons, Inc., 1993.

[48] R. Jacob Baker, *CMOS Circuit Design, Layout, and Simulation*, Wiley-IEEE Press, ISBN 9780470881323, 3rd Edition, 2010.

[49] Ali Eftekhari, "pH Sensor Based on Deposited Film of Lead Oxide on Aluminum Substrate Electrode", *Sensors and Actuators B: Chemical*, vol. 88, Issue 3, Feb. 2003, pp. 234-238.

[50] William R. Heineman, Henry J. Wieck, and Alexander M. Yacynych, "Polymer Film Chemically Modified Electrode as a Potentiometric Sensor", *Anal. Chem.*, 1980, 52 (2), pp 345–346.

[51] R. A. J. Croce, SanthiSagar Vaddiraju, Jun Kondo, Yan Wang, Liang Zuo, Kai Zhu, Syed K. Islam, Diane J. Burgess, Fotios Papadimitrakopoulos and Faquir C. Jain, "A Miniaturized Transcutaneous System for Continuous Glucose Monitoring", *Biomedical Microdevices*, vol. 15, pp. 151-160, 2013.

[52] https://www.maximintegrated.com/en/app-notes/index.mvp/id/660, Maxim Inc.

[53] https://www.mosis.com/vendors/view/global-foundries/8rf-dm

[54] Rohm Semiconductor, "Comparator, Control Circuit of Switching Regulator Using the Same, Switching Regulator, and Electronic Equipment", *China Patent # CN 102541142 A*, published Jul 4, 2012.

[55] Bang S. Lee, "Technical Review of Low Dropout Voltage Regulator Operation and Performance", *Application Note SLVA072*, Texas Instruments, 1999.

[56] Maxwell F Kennedy, E. J. Kennedy, "Operational Amplifier Circuits: Theory and Applications", ISBN0030019478, 9780030019470, *Oxford University Press*, Incorporated, 1995.

[57] Behzad Razavi, "Design of Analog CMOS Integrated Circuits", ISBN-13: 978-0072380323, 1st Edition, *McGraw-Hill Education*, 2000.

[58] P.K. Chan, L.S. Ng, L. Siek and K.T. Lau, "Designing CMOS Folded-Cascode Operational Amplifier with Flicker Noise Minimisation", *Microelectronics Journal*, Short Communication, 32, pp. 69–73, 2001.

Appendix

The input impedance of a sensor system is an important parameter, which relates with the sensor dynamic output. The proposed system provides infinite input impedance for the sensor due to the PMOS gate as the input stage. As a small size PMOS, MP0 presents an infinite impedance under DC. The only AC impedance is the input gate capacitance which is the sum of the gate to drain capacitance, and gate to source capacitance multiplied by 1 minus the gate to source gain, which is

$$C_{in} = C_{GD} + C_{GS}(1 - A_{GS}) \tag{A-1}$$

Where

$$A_{GS} = \frac{R_S}{R_S + 1/g_m} \tag{A-2}$$

In this case RS is equivalent to the current source impedance, which is much higher than 1/gm. gm is the transconductance of MP0. So AGS is close to 1, which simplifies the input capacitance to CGD. Since MP0 is small (in this design it is W/L = 2μm/0.18μm), CGD is about 30fF.

Accuracy of the pH sensor readout system can be defined as the output frequency versus input voltage if the pH sensor output curve considered ideal. However, in this system, it is more valuable to check the linearity of f_{out} - Vin curve since the absolute value of the f_{out} at certain input voltage can be calibrated. The analysis can be found in previous section.

Vita

Song Yuan was born in Shandong, China. After graduation in 2000 from Qingdao No. 58 High School, he attended the Qingdao University of Science and Technology, where he earned a Bachelor of Science degree in 2005 from the Electrical Engineering and Automation Control Department. After graduating, Mr. Yuan was employed at Qingdao MESNAC Inc. as a hardware engineer. From fall 2007, he was enrolled in the department of Electrical Engineering and Computer Science at the University of Tennessee, Knoxville. At the same time, he joined in the Analog, VLSI and Devices Laboratory as a graduate teaching assistant. During his last year of Master study, he received ACM/IEEE Outstanding ECE Teaching Assistant 2010-2011. In the spring of 2012, he started his career as an intern at Electrical Research and Design Group of Siemens Molecular Imaging Inc. in Knoxville, Tennessee where he was a senior engineer when he resigned at August 2017. At Siemens Molecular Imaging Inc., he involved in the design of the front-end ASIC for Siemens first silicon photomultiplier base positron emission tomography (PET) medical imaging scanners and got it ready for the mass-production. Meanwhile, Mr. Yuan has been a candidate for the Ph.D. degree in electrical engineering from the University of Tennessee. Just before the defense of the dissertation, Mr. Yuan resigned from Siemens and started a ASIC company named Grectronics Inc. in China with his four friends, Getao Liang, Kevin Tham, Kai Zhu and Liang Zuo, who were well known to each other when he studied at the University of Tennessee. Mr. Yuan will complete his Doctor of Philosophy degree in Electrical Engineering in Fall 2017 which is his tenth year in U.S.